THE COLOUR DIPOLE MODEL OF DIFFRACTIVE SCATTERING

THE UNIVERSITY of MANCHESTER

A thesis submitted to the University of Manchester
for the degree of Doctor of Philosophy
in the Faculty of Science and Engineering

By

Ruben Sandapen

Department of Physics and Astronomy

November 2002

Contents

List of Figures

List of Tables

Abstract

UNIVERSITY OF MANCHESTER

ABSTRACT OF THESIS submitted by **Ruben Sandapen** for the Degree of Doctor of Philosophy and entitled **The colour dipole model of diffractive scattering**

Month and Year of Submission: November 2002

We study two exclusive diffractive processes, Deeply Virtual Compton Scattering (DVCS) and vector meson production within the colour dipole model. In doing so, we concentrate on the Forshaw, Kerley and Shaw (FKS) dipole model which yields successful predictions for both Deep Inelastic Scattering (DIS) and diffractive DIS, for photon virtualities Q^2 down to and including $Q^2 = 0$ GeV^2. In the case of DVCS, we also study the alternative McDermott, Frankfurt, Guzey and Strikman (MFGS) dipole model which has so far been applied to DIS and is restricted to reasonably large $Q^2 > 1$ GeV^2.

Both models give a good description of the H1 data on DVCS, and the predictions agree closely, even beyond the HERA energy range. For the kinematic range of the recent ZEUS preliminary data, we find a more significant difference between the predictions of the two models and by adjusting the value of the diffractive slope, both models can describe the data.

In our analysis of vector meson production, the unknown meson light-cone wavefunction introduces a major element of uncertainty in our calculation. We choose to explore and use two different parametrisations for the meson light-cone wavefunction, one by Nemchik, Nikolaev, Predazzi and Zakharov (NNPZ) and another by Dosch, Gousset, Kulzinger and Pirner (DGKP). Both parametrisations are constructed in analogy to the perturbative photon light-cone wavefunction, but differ in their specific functional form and choice of free parameters. We give predictions for ρ, ϕ and J/Ψ meson production. Our predictions are consistent with the available HERA data, though for the light mesons, we are unable to fit the total cross-section and longitudinal to transverse cross-section ratio data simultaneously using the same set of free parameters in the NNPZ wavefunction.

Declaration

No portion of the work referred to in this thesis has been submitted in support of an application for another degree or qualification of this or any other university or other institution of learning.

Copyright and Ownership of Intellectual Property Rights

Acknowledgements

First of all, I would like to thank warmly my supervisor, Graham Shaw for his precious guidance, useful discussions and his calming influence during these past three years.

I am also extremely grateful to Jeff Forshaw for enlightening discussions, his advice on various occasions and simply for being a marvellous physics teacher.

I am equally grateful to Martin McDermott for all his help, useful discussions and collaboration on our joint paper on DVCS.

I thank my former colleagues in the Manchester theory group, especially George Kerley, Janis Gravelis, Fabrice Thalmann and Nicholas Petropoulos who helped me to get started.

Thanks to Gavin Poludniowski for useful discussions and for proofreading the derivations of the photon light-cone wavefunctions in this thesis.

I am happy to thank to Stephan Gieseke, Stephane Munier, Mara Soares and Ana Stasto for correspondance about their work on photon light-cone wavefunctions and vector meson production, Yuji Yamazaki for sending me the recent preliminary ZEUS data on DVCS, and Jan Olsson for sending me a compilation of recent HERA results on vector meson production.

Special thanks to Gail for all her generous help including her warm welcome for an extended stay in her house during the writing-up period. Thanks also to Jeff and Martin for welcoming me and being so nice housemates.

Big thanks to Dad and Mum Michel and Marie-Paule without whom I would never have got so far.

Last but by no means least, I thank Anne-Pascale for our relationship.

This work is supported by a University of Manchester scholarship.

Autobiographical Note

The author was born in the small town of Rose-Hill on the tropical island, Mauritius, Indian Ocean in 1975. After graduating with a first class BSc (Hons) degree in Physics from the University of Mauritius in 1999, he obtained a full scholarship to join the theoretical physics group of the University of Manchester, England.

Dedication

To Anne-Pascale

Chapter 1

Introduction

This introductory chapter is a review chapter. We begin with the kinematics of a general two-body scattering process and recall the key ideas of S matrix theory, in particular the unitarity relation and the optical theorem. We then review the basic features of Regge theory ideas which lead to the idea of pomeron exchange in hadron-hadron elastic[1] scattering at high energy. We next turn to photon-hadron interactions which show striking similarities with hadron-hadron scattering suggesting the idea of the hadronic fluctuation of the photon. The virtuality of the photon can provide a hard scale to enable a perturbative expansion in Quantum Chromodynamics (QCD). This leads to the subject of Deep Inelastic Scattering, where we shall first meet the concept of factorisation of long-distance from short-distance dynamics. At the same time, we introduce the proton's structure functions, their scaling behaviour and direct interpretation in terms of parton distribution functions within the parton model. We discuss qualitatively the QCD corrections to the parton model which explain scaling violations. We finally introduce diffractive deep inelastic scattering and exclusive diffractive processes.

1.1 Two-body scattering

Consider a general two-particle to two-particle scattering process as shown in Figure 1.1.

The *s-channel* reaction is

$$a(p_1) + b(p_2) \to c(p_3) + d(p_4) \tag{1.1}$$

where p_i is the 4 momentum of a particle. The Mandelstam variables s, t and u are then defined as follows,

$$s = (p_1 + p_2)^2 \ , \tag{1.2}$$

$$t = (p_1 - p_3)^2 \ , \tag{1.3}$$

$$u = (p_1 - p_4)^2 \ . \tag{1.4}$$

[1] more generally diffractive. See Section 1.3.

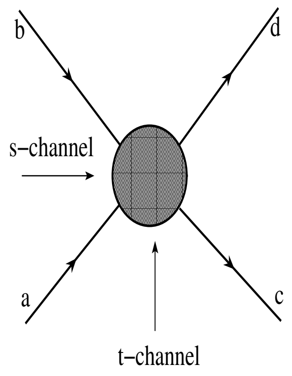

Figure 1.1: Two-particle to two-particle scattering

In the centre-of-mass frame,

$$s = (E_1 + E_2)^2 \ , \tag{1.5}$$

so that s is the square of the centre of mass energy. If each particle has the mass m, then momentum conservation guarantees that[2]

$$s + t + u = \sum_{i=1}^{4} m_i^2 \ , \tag{1.6}$$

which means that there are only two independent variables, taken to be s and t. Consider now the crossed reaction

$$a(p_1) + \bar{c}(-p_3) \to \bar{b}(-p_2) + d(p_4) \ . \tag{1.7}$$

We see that in this case t is the centre of mass energy and s is the momentum transferred between particles a and c. (1.7) is the *t-channel* reaction.

If θ is the angle between $\vec{p_1}$ and $\vec{p_3}$, we see that

$$t = t_{\text{min}} + 2|\vec{p_1}||\vec{p_3}|(\cos\theta - 1) \tag{1.8}$$

[2]We use $\hbar = c = 1$ throughout.

with

$$t_{\text{min}} = m_1^2 + m_3^2 - 2E_1E_3 + 2|\vec{p_1}||\vec{p_3}| \ . \tag{1.9}$$

If the reaction is *elastic*,

$$a(p_1) + b(p_2) \to a(p_1) + b(p_2) \quad ,$$

then $t_{\text{min}} = 0$ and $t = 0$ in the *forward* direction, $\theta = 0$. In the general case, the expression for t_{min}, in terms of s and the masses m_i, is both clumsy and unrevealing for our purposes. Instead let us consider the high energy limit : $s \gg m_i^2$ and $m_2 = m_4$. In this case, we have [1]

$$t_{\text{min}} \approx -\frac{m_2^2(m_3^2 - m_1^2)^2}{s^2} \ . \tag{1.10}$$

The point to remember is that for a inelastic reaction, t is not zero even in the forward direction ($\theta = 0$), the lower limit being given by (1.10) in the high energy limit and when $m_2 = m_4$.

Consider the s-channel reaction (1.1). We expect the amplitude for (1.1) to be Lorentz invariant, being a function of the two independent Mandelstam variables s and t : $\mathcal{A}(s,t)$. In terms of the amplitude, the differential cross-section is then given by [2]

$$d\sigma = \frac{|\mathcal{A}(s,t)|^2}{F} dQ \ , \tag{1.11}$$

where F is the flux of incoming particles and dQ is the Lorentz invariant phase space factor. A Lorentz invariant expression for the flux F is [2]

$$F = 4\sqrt{[(p_1.p_2)^2 - m_1^2 m_2^2]} \ . \tag{1.12}$$

In the high energy limit, the flux F becomes

$$F \approx 2s \ . \tag{1.13}$$

The Lorentz invariant phase space factor dQ is given by[3] [2]

$$dQ = (2\pi)^4 \delta^4(p_3 + p_4 - p_1 - p_2) \frac{d^3\vec{p}_3}{(2\pi)^3 2E_3} \frac{d^3\vec{p}_4}{(2\pi)^3 2E_4} \tag{1.14}$$

[3] We are using plane wave to represent free particles with the normalisation of $2E$ particles per unit volume [2].

A little algebra reveals that in the centre-of-mass frame,

$$\frac{d\sigma}{d\Omega_{cm}} = \frac{1}{64\pi^2 s}\frac{|\vec{p_3}|}{|\vec{p_1}|}|\mathcal{A}(s,t)|^2 \ . \tag{1.15}$$

where $|\vec{p_1}| = |\vec{p_2}|$ and $|\vec{p_3}| = |\vec{p_4}|$. Using (1.15) and (1.8), we arrive at the following Lorentz invariant expression for the differential cross-section :

$$\frac{d\sigma}{dt} = \frac{1}{16\pi s^2}|\mathcal{A}(s,t)|^2 \ . \tag{1.16}$$

The physics resides in the scattering amplitude $\mathcal{A}(s,t)$ and (1.16) relates this quantity to the experimentally measurerable differential cross-section. We shall use repeatedly (1.16) in later chapters.

1.2 The S-matrix

This section contains a condensed[4] account of the S matrix, following [3]. Our aim is to introduce the Cutkosky rules and in particular the optical theorem which we shall use later. For a general scattering process, the overlap of *free* particle states a long time before ($t = -\infty$) the scattering with *free* particle states a long time after ($t = +\infty$), the S_{fi} element of the S-matrix is

$$S_{fi} = \langle \mathrm{f}|\hat{S}|\mathrm{i}\rangle \ . \tag{1.17}$$

where $\hat{S}$ is the scattering operator. The S-matrix is assumed to be

- Lorentz invariant
- unitary
- analytic

We have already made use of the property of Lorentz invariance when writing the amplitude as a function of the Mandelstam variables s and t. Let us explore the unitarity property. Recall that the S-matrix encodes all information about the scattering process *including the case of no scattering*. Therefore, the probability of a state $|i\rangle$

[4]More details can be found in e.g [1].

scattering into some state $|f\rangle$, summed over all such states $|f\rangle$, including the case when $|f\rangle$ coincides with $|i\rangle$, must be *unity* :

$$P_{\text{tot}} = \sum_f S^*_{fi} S_{fi} = 1 \; . \tag{1.18}$$

This leads to the condition

$$\sum_f S^\dagger_{if} S_{fi} = S^\dagger S = S S^\dagger = 1 \; . \tag{1.19}$$

In other words, the unitarity property of the S-matrix is a direct consequence of the conservation of probability. To isolate the no-scattering part, we write

$$S_{fi} = \delta_{fi} + T_{fi} \quad ; \quad T_{fi} = i(2\pi^4)\delta^4(p_f - p_i)\mathcal{A}_{fi} \; . \tag{1.20}$$

p_f (p_i) is the *total* momenta in the final (initial) state and $\mathcal{A}_{fi}$ is the scattering amplitude of a state $|i\rangle$ going to a state $|f\rangle$. The delta function in (1.20) simply expresses conservation of total momentum. Using (1.20) and the unitarity property of the S-matrix (1.19), we find that

$$2\Im m \mathcal{A}_{fi} = (2\pi)^4 \delta^4(p_f - p_i) \sum_m \mathcal{A}_{im} \mathcal{A}^\dagger_{mf} \; . \tag{1.21}$$

If we have N particles in the intermediate state $|m\rangle$, we integrate over the phase space of all particles. Explicitly,

$$2\Im m \mathcal{A}_{fi} = \sum_m \int \prod_{n=1}^{N} \frac{d^3 p_n}{(2\pi)^3 2E_n} \mathcal{A}_{im} \mathcal{A}^\dagger_{mf} (2\pi)^4 \delta^4(p_f - p_i) \; . \tag{1.22}$$

(1.22) gives the *Cutkosky* rules [4] which allows us to calculate the imaginary part of an amplitude by considering the amplitudes of the incoming and outgoing states into all possible intermediate states. The Cutkosky rule is particularly useful for calculating the imaginary amplitude of a loop diagram, as we shall see in Chapter 2. If the state $|i\rangle$ is identical[5] to the final state $|f\rangle$, (1.22) becomes

$$2\Im m \mathcal{A}_{\text{el}}(s, t = 0) = \sum_m \int \prod_{n=1}^{N} \frac{d^3 p_n}{(2\pi)^3 2E_n} |\mathcal{A}_{im}|^2 (2\pi)^4 \delta^4(p_f - p_i) \; . \tag{1.23}$$

[5]This means that $|i\rangle$ has the same particles as $|f\rangle$ and that the momentum and spin of each particle does not change (elastic, forward and no-spin flip scattering) [1]. Note however that (as we shall see later) the modern literature defines the term “elastic” less restrictively in the context of diffractive reactions.

Dividing the right-hand side by the high energy limit flux factor (see (1.13)), it becomes the *total* cross-section for the initial state $|i\rangle$ to go into some final state $|m\rangle$, summed over all such states, that is

$$\Im m \mathcal{A}_{\mathrm{el}}(s, t=0) = s\sigma_{\mathrm{tot}} \,. \tag{1.24}$$

(1.24) is an extremely important and useful relation known as the *optical theorem.* Using the optical theorem, we can rewrite (1.16) as

$$\frac{d\sigma^{\mathrm{el}}}{dt}|_{t=0} = \frac{1}{16\pi}|\sigma_{\mathrm{tot}}|^2(1+\beta^2) \tag{1.25}$$

where β is the ratio of real to imaginary parts of the amplitude,

$$\beta = \frac{\Re e \mathcal{A}}{\Im m \mathcal{A}} \,. \tag{1.26}$$

The amplitude $\mathcal{A}$ for the scattering is also assumed to be an *analytic* function of the Mandelstam variables s and t, regarded as complex variables. By analytic continuation, the same amplitude describes a reaction and its crossed version.

$$\mathcal{A}_{ab\to cd}(s,t,u) = \mathcal{A}_{a\bar{c}\to\bar{b}d}(t,s,u) \tag{1.27}$$

Analyticity also leads to dispersion relations which allows us to reconstruct the real part of an amplitude given the imaginary part [3].

1.2.1 The high energy limit amplitude

Regge theory [5] provides a framework to describe scattering amplitudes in the kinematic limit $s \gg |t|$, known as the Regge limit. A formal account of Regge theory can be found in [6]. Here we aim at presenting the essential ideas. We outline the standard[6] procedure, the Sommerfeld and Watson transformation (see e.g [3]) which leads to the emergence of Regge poles (and Regge trajectories) and a key formula for the scattering amplitude in the high energy limit. *The whole procedure is designed to extract the high energy behaviour of the scattering amplitude.* Starting with the t channel process, we can make a partial wave expansion of the amplitude,

$$\mathcal{A}_{a\bar{c}\to\bar{b}d}(t,s) = \sum_{l=0}^{\infty}(2l+1)a_l(s)P_l\left(1+\frac{2t}{s}\right) \,. \tag{1.28}$$

[6]For an alternative approach, see [1].

Here, $a_l(s)$ is the partial wave amplitude and P_l is the Legendre polynomial. Analytic continuation into the s channel gives

$$\mathcal{A}_{ab\to cd}(s,t) = \sum_{l=0}^{\infty}(2l+1)a_l(t)P_l\left(1+\frac{2s}{t}\right) \tag{1.29}$$

The next step, following Sommerfeld [7] and Watson [8] is to rewrite (1.29) into a contour integration in the complex angular momentum l plane :

$$\mathcal{A}(s,t) = \frac{1}{2i}\oint_C dl(2l+1)\frac{a(l,t)}{\sin\pi l}P\left(l,1+\frac{2s}{t}\right) \tag{1.30}$$

C is a contour surrounding the positive real l axis as shown in Figure 1.2. For integer values of l, we have poles in (1.30) due to the $\sin\pi l$ which reproduces (1.29). We would think that the complex function $a(l,t)$ is not unique since we can add to it any function which vanishes at the integer values of l and still reproduce (1.29). However, a theorem due to Carlson [9] tells us that $a(l,t)$ is unique if it satisfies the condition $a(l,t) < \exp(\pi|l|)$ as $|l| \to \infty$. In the relativistic case, we need to introduce two analytic functions $a^{(+1)}(l,t)$ and $a^{(-1)}(l,t)$ (each separately unique) for the even and odd partial wave amplitudes respectively:

$$\mathcal{A}(s,t) = \frac{1}{2i}\oint_C dl\frac{(2l+1)}{\sin\pi l}\sum_{\eta=\pm}\frac{(\eta+e^{-i\pi l})}{2}a^{(\eta)}(l,t)P\left(l,1+\frac{2s}{t}\right) . \tag{1.31}$$

η is called the signature. Deforming the integration contour to C' (the line $\Re e l = -1/2$) as shown in Figure 1.2, we pick up $2\pi i \times$ *residue* due to isolated singularities (poles) in the new domain of integration. *In the high energy limit*, the integration along C' vanishes and the leading term in the Legendre polynomial is extracted to give the following formula for the scattering amplitude,

$$\mathcal{A}(s,t) = \sum_i \frac{(\eta_i+e^{-i\pi\alpha_i(t)})}{2}\beta(t)s^{\alpha_i(t)} , \tag{1.32}$$

where the sum runs over all Regge poles. In practice only the leading Regge pole (with the largest value of $\Re e\alpha_i(t)$) is retained. The amplitude (1.32) can then be factorised as follows:

$$\mathcal{A}(s,t) = \frac{(\eta+e^{-i\pi\alpha(t)})}{2\sin\pi\alpha(t)}\frac{\gamma_{ac}(t)\gamma_{bd}(t)}{\Gamma(\alpha(t))}s^{\alpha(t)} . \tag{1.33}$$

where γ_{ac} (γ_{bd}) are the couplings of the Reggeon to the particles a and c (b and d). These are real functions of t. $\Gamma(\alpha(t))$ has been extracted to cancel the so-called nonsense poles [3]. (1.33) is the key equation we were referring to at the beginning of this section. We interprete (1.32) as giving the high energy limit scattering s-channel amplitude with the exchange in the t-channel of a "particle" with angular momentum equal to $\alpha(t)$. Of course, it is not a particle since $\alpha(t)$ is not integer (or half integer). It is called a *Reggeon*. $\beta(t)$ contains the couplings of the Reggeon to the particles. It tells us the *universal* (since the couplings depend on t only) dependence of scattering amplitude on s in the high energy limit from a particular Reggeon exchange. Immediately, we can find a simple expression for the ratio β of the real to imaginary parts of the scattering amplitude. Using (1.33), we find that

$$\beta = \frac{\Re e \mathcal{A}}{\Im m \mathcal{A}} = -\frac{\eta + \cos\pi\alpha(t)}{\sin\pi\alpha(t)} \ . \tag{1.34}$$

(1.34) allows us to calculate the ratio of the real to imaginary parts of the forward amplitude with a knowledge of the Regge intercept, $\alpha(0)$. We shall use (1.34) in Chapter 3.

1.2.2 Regge trajectories and the Pomeron

Now we make the connection with physical particles. We can think of physical particles being exchanged in the t-channel with $\alpha(t)$ giving the spin J of the exchanged particle when $t = M^2$, where M is the mass of the exchange particle. Chew and Frautschi [10] have plotted the spins and masses of families of mesons and found that those for the low lying mesons all lie in straight line:

$$\alpha(t) = \alpha(0) + \alpha' t \quad ; \quad \alpha(0) = 0.55 \text{ and } \alpha' = 0.86 \text{ GeV}^{-2} \ . \tag{1.35}$$

(1.35) is called a Regge trajectory. Using (1.16) and (1.33) it follows that

$$\frac{d\sigma}{dt} \propto s^{(2\alpha(0) - 2\alpha' t - 2)} \ . \tag{1.36}$$

The optical theorem (1.24) also tells us that

$$\sigma_{\text{tot}} \propto s^{(\alpha(0)-1)} \ . \tag{1.37}$$

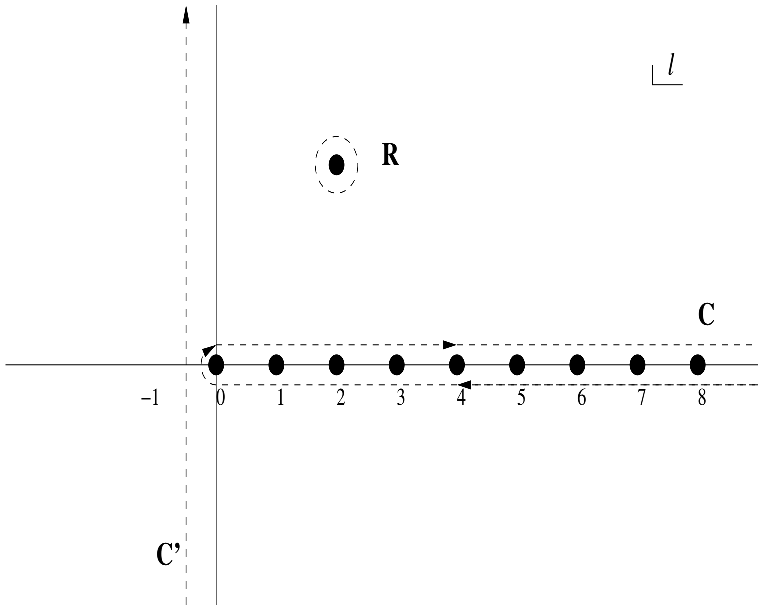

Figure 1.2: The Sommerfeld-Watson transformation: The contour of integration is deformed from C to C'. Singularities in the new domain of integration give rise to the Regge poles.

Hence knowing the Regge intercept $\alpha(0)$, we get the s dependence of the total cross-section. Conversely, we can extract the Regge intercept from fits to total cross-section data.

1.2.3 The Pomeron

If only a meson Regge trajectory is exchanged during a scattering process, (1.37) predicts that the total cross-section decreases and vanishes asymptotically. Experimentally, this is *not* the case: The total cross-section decreases initially and at sufficiently high s starts to rise slowly as shown in Figure 1.3. If we attribute this rise to a new Regge trajectory, then the Regge intercept must be greater that unity: $\alpha(0) > 1$. This new Regge trajectory is called the *Pomeron* trajectory or simply the Pomeron. Donnachie and Landshoff made a simultaneous fit to a comprehensive set of pp (and $p\bar{p}$) total cross-section data . Their results are as follows [24]

$$\sigma_{pp} = 21.7 s^{0.08} + 56.1 s^{-0.45} \quad ; \quad \sigma_{\bar{p}p} = 21.7 s^{0.08} + 98.4 s^{-0.45} \; . \tag{1.38}$$

Hence, the extracted Pomeron intercept is

$$\alpha(t=0) = 1.08 \; . \tag{1.39}$$

This is usually referred to as the "soft" Pomeron intercept. The Pomeron carries the quantum numbers of the vacuum (colour singlet, isospin zero and even under the operation of charge conjugation). This follows from the Pomeranchuk theorem [12] which asserts that if there is charge exchange, the cross-section vanishes asymptotically. From the fact that the Pomeron intercept is near 1 and that the amplitude is predominantly imaginary, (1.34) tells us that the Pomeron has even signature, $\eta = 1$.

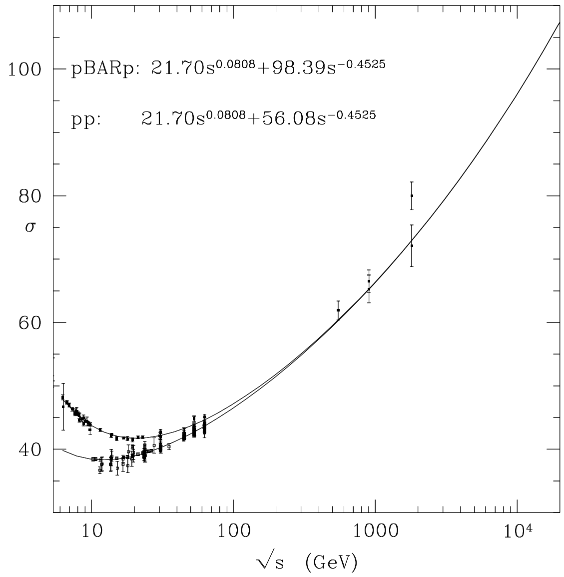

Figure 1.3: The Donnachie-Landshoff fits. Figure from [24].

1.3 Analogy with optical diffraction

So far, we have focused on the high energy limit of elastic amplitudes and hence total cross-sections via the optical theorem, where the scattering proceeds by Pomeron exchange. *Elastic scattering, in the high energy limit, is in fact a special case of a wider class of processes called diffractive processes.* It is natural to wonder why the term 'diffraction' is being employed and whether this has anything to do with the more familiar optical diffraction. In fact, diffraction in particle scattering is exactly analogous to diffraction in optics. To see this, consider a plane wave incident on a disc of radius R_0. It is well known that if a screen is place a *long* distance behind the disk, a diffraction pattern is observed on the screen. This is called Fraunhofer diffraction. It follows from Huygen's principle which states that each point on the disk acts as a source for a secondary spherical waves which then interfere between themselves giving the diffraction pattern. If the wavelength of the incident wave is λ, then the DeBroglie relation tells us that the magnitude of its momentum is $k = 2\pi/\lambda$. If the momentum of the incoming photons is $\boldsymbol{k_1}$ and that of the outgoing photons is $\boldsymbol{k_2}$, the momentum transfer is $\boldsymbol{\kappa} = \boldsymbol{k_1} - \boldsymbol{k_2}$. The resulting amplitude on the screen is given by the two-dimensional Fourier transform of the momentum transfer (See e.g [27, 26])

$$\mathcal{A} = \int_{disc} d^2\boldsymbol{x} e^{i\boldsymbol{\kappa}.\boldsymbol{x}} \ . \tag{1.40}$$

where $\boldsymbol{x}$ is the two-dimensional vector specifying the disc. Integrating over the surface of the disk, using the integral identity [23] for the Bessel function of order ν,

$$\int z^{\nu+1} J_\nu(z) dz = z^{\nu+1} J_{\nu+1}(z) \ , \tag{1.41}$$

gives

$$\mathcal{A} = \frac{2\pi R_0 J_1(\kappa R_0)}{\kappa} \tag{1.42}$$

where for small angle, $\kappa \approx k_1\theta$. The intensity as a function of the scattering angle θ in a diffraction pattern is then given by

$$\frac{I(\theta)}{I(\theta = 0)} = \frac{[2J_1(\kappa R_0)]^2}{(\kappa R_0)^2} \approx 1 - \frac{R_0^2}{4}(k_1\theta)^2 \ , \tag{1.43}$$

where we have neglected higher powers of θ. This has a striking similarity with the elastic differential hadron-hadron cross-section which is described experimentally by a forward ($t = 0$) peak and an exponential decrease with increasing $|t|$:

$$\frac{d\sigma/dt}{d\sigma/dt|_{t=0}} \approx \exp(-B|t|) \approx 1 - B(p_1\theta)^2 \ . \tag{1.44}$$

where p_1 is the incident hadron momentum and $|t| \approx (p_1\theta)$ is the 4-momentum transfer squared, for small scattering angle θ. Again B (known as the diffractive slope) is related to the size of the interacting particle and is measured experimentally for a given process. Integrating (1.44) over t, we find that

$$\sigma = \frac{d\sigma/dt|_{t=0}}{B} \,. \tag{1.45}$$

Given B, (1.45) allows us to deduce the total cross-section, once we have calculated the forward differential cross-section.

We have seen that the hadron-hadron elastic scattering is analogous to Fraunhofer diffraction in classical optics. In optical diffraction, $|\boldsymbol{k}_1| = |\boldsymbol{k}_2|$ and in particle diffractive scattering, the 4-momentun transfer is small and all 4-mometa are much less than the centre-of-mass energy squared, s [26].

In addition to elastic scattering we can also have singly dissociative and doubly dissociative diffractive scattering where either one of both of the incoming particles break up. These three types of diffractive scattering are illustrated in Figure 1.4.

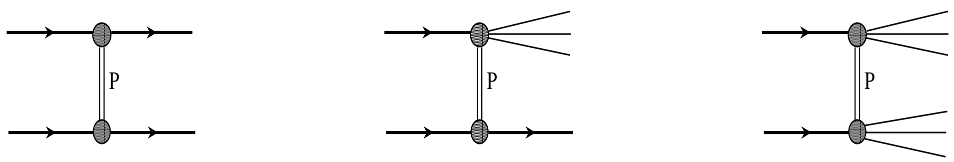

Figure 1.4: From left to right: elastic (diffractive) scattering, singly dissociative diffractive scattering and doubly dissociative diffractive scattering. The double line indicates Pomeron (P) exchange.

Experimentally, there is a large *rapidity gap* between the final states in each of the three types of diffractive scattering [42, 43]. At high energy, the rapidity η is given by

$$\eta = \frac{1}{2}\ln\left(\tan\frac{\theta}{2}\right) \tag{1.46}$$

where θ is the angle between the outgoing states. Thus, at high energy a large rapidity gap is equivalent to a large angular gap between the outgoing states. A rapidity gap can only exist if an object with vacuum quantum numbers is exchanged during the scattering, otherwise it is exponentially suppressed. The presence of a rapidity gap is consistent with Pomeron exchange.

1.4 Photon-hadron interactions

1.4.1 Vector meson dominance

So far, we have discussed only about hadron-hadron interaction. Apart from being several orders of magnitude lower, the photon-hadron cross-section shows strikingly similar features to hadron-hadron cross-section. For instance, the total photon-hadron cross-section just as the hadron-hadron total cross-section remains nearly constant with increasing energy. Moreover, the diffraction peak present in the hadron-hadron elastic differential cross-section is also present in the photon-hadron case. We are driven to conclude that the photon has a point-like component (which is the gauge boson of QED) and a hadronic component [13],

$$|\gamma\rangle = |\gamma_{\text{bare}}\rangle + C|\gamma\rangle_{\text{had}} \tag{1.47}$$

where C is a coefficient specifying the probability of the hadronic fluctuation. At intermediate energies, the photon is assumed to fluctuate into a vector meson. This is the *vector meson dominance model* [13]:

$$|\gamma\rangle_{\text{had}} = a|\rho\rangle + b|\omega\rangle + c|\phi\rangle \ . \tag{1.48}$$

Vector meson dominance models work well for real photons or photons of low virtuality. We can also have a highly virtual photon interacting with a hadron. The presence of a hard scale (here the virtuality of the photon) allows the use of peturbative Quantum Chromodynamics. This is the case in Deep Inelastic Scattering. First, let us recall the most basic features of Quantum Chromodynamics.

1.4.2 Quantum Chromodynamics

Quantum Chromodynamics (QCD) is a non-Abelian gauge theory based upon SU(3) symmetry of colour charge. Spin 1/2 quarks and spin 1 gluons are the fundamental degrees of freedom. The quarks form a colour triplet and the gluons a colour octet. The QCD lagrangian is [17]

$$\mathcal{L}^{QCD} = -\frac{1}{4} G^a_{\mu\nu} G^{a\mu\nu} + \sum_f \bar{\psi}_f (i \not{D} - m_f) \psi_f + \text{gauge fixing term} + \text{ghost terms} \ , \tag{1.49}$$

where a is a colour label, running from 1 to 8 for the $SU(3)$ and f runs over quark flavours. The covariant derivative and field strength tensor are given by

$$D_\mu = \partial_\mu - i g_s A^a_\mu T^a \ , \tag{1.50}$$

$$G^a_{\mu\nu} = \partial_\mu A^a_\nu - \partial_\nu A^a_\mu + g f^{abc} A^b_\mu A^c_\nu \ , \tag{1.51}$$

where the f^{abc} are the structure constant of $SU(3)$ and T^a are a set of eight independent Hermitian traceless 3×3 matrices. Feynman rules analogous to those of Quantum Electrodymanics (QED) can then be derived. Many pedagogical discussions of QCD and its applications are available; see e.g [14]. Let us here only recall two very important features of QCD. The first one is *asymptotic freedom* which means that at high momentum transfer or short distance, we can use perturbation theory. The running coupling α_s at lowest order is given by

$$\alpha_s(Q^2) = \frac{12\pi}{(33 - 2N_f)\ln(Q^2/\Lambda^2)} \tag{1.52}$$

where in general Q is a characteristic momentum or energy transfer in the process under consideration. In DIS, this would be the virtuality of the photon as defined earlier. If there is a hard ($Q \gg \Lambda$) scale so that $\alpha_s \ll 1$ in (1.52), a perturbative expansion in α_s is legitimate. The second is *colour confinement* which means that real physical particles exist only as colour singlets. Hence in an actual physical process, there is always a soft non-perturbative piece which cannot be calculated within pQCD. We shall see this explicitly in Deep Inelastic Scattering.

1.4.3 Deep Inelastic Scattering

The Deep Inelastic process (at $Q^2 \ll M_z^2$, where M_z is the mass of the Z boson) is shown in Figure 1.5(a). The overall process is

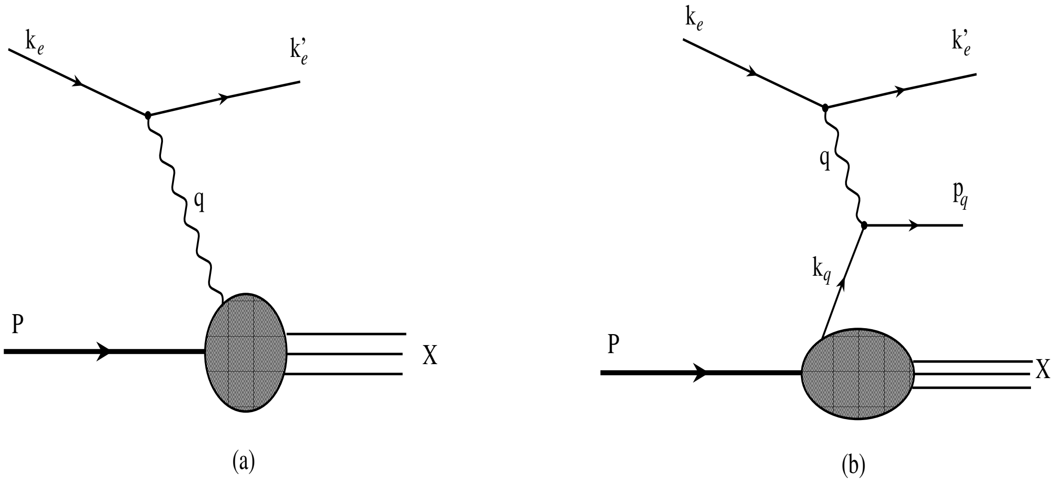

Figure 1.5: (a) Deep Inelastic Scattering (DIS). (b) Parton model of DIS. The 4-momenta shown are defined in the text.

$$e(k_e) + p(P) \to e(k'_e) + X \quad ,$$

and the photon-proton subprocess is

$$\gamma^*(q) + p(P) \to X \quad ,$$

where the 4-momenta are given in brackets. The standard DIS variables are the virtuality of the photon,

$$Q^2 = -q^2 \ , \tag{1.53}$$

the dimensionless Bjorken variable x[7],

$$x = \frac{Q^2}{2P.q} \tag{1.54}$$

The photon-proton centre of mass energy given by

$$W^2 = (q+P)^2 = s \ . \tag{1.55}$$

Note that in the high energy limit, we can write

$$x \approx \frac{Q^2}{s} \ . \tag{1.56}$$

[7]We reserve x for the Bjorken variable throughout.

Finally a third variable to characterise fully the DIS process is

$$y = \frac{P.q}{P.k_e} = \frac{W^2 + Q^2}{S} \ , \tag{1.57}$$

where $S = (P + k_e)^2$.

In terms of the above variables, the differential cross-section factorises into leptonic and hadronic tensors,

$$\frac{d^2\sigma}{dx dQ^2} \propto L_{\mu\nu} W^{\mu\nu} \ . \tag{1.58}$$

It is straightforward to calculate $L_{\mu\nu}$ in QED [2]

$$L_{\mu\nu}(k_e, k_e') = k_{e\mu} k_{e\nu}' + k_{e\nu} k_{e\mu}' - g_{\mu\nu}(k_e.k_e' - m_e^2) \ . \tag{1.59}$$

where m_e is the electron mass. We shall be more interested in the hadronic tensor which describes the photon-proton interaction which includes long-distance, non-perturbative physics. The most general expression for $W^{\mu\nu}$ is [2, 15]

$$W^{\mu\nu}(P,q) = \left(g^{\mu\nu} - \frac{q^\mu q^\nu}{q^2}\right) W_1(x,Q^2) + \left(P^\mu + \frac{1}{2x} q^\nu\right)\left(P^\nu + \frac{1}{2x} q^\mu\right) W_2(x,Q^2) \ . \tag{1.60}$$

The proton's structure functions F_1 and F_2 are related to the scalar functions W_1 and W_2 via [15]

$$F_1(x,Q^2) = W_1(x,Q^2) \quad ; \quad F_2(x,Q^2) = (P.q) W_2(x,Q^2) \ . \tag{1.61}$$

In principle, the structure functions depend on both x and Q^2. We shall shortly see that in the parton model, the structure functions exhibit Bjorken scaling [18], that is they depend only on the dimensionless variable x. QCD corrections to the parton model then predict a logarithmic Q^2 dependence. First, let us see how scaling arises. In the parton model, we make the assumption (a second assumption will come later) that the photon scatters off a single *free* parton as shown in Figure 1.5(b). The amplitude for the Feynman diagram 1.5(b)(not taking into account the leptonic vertex) is [19]

$$\mathcal{M}^\mu(p_q, X; P) = e e_q \bar{u}_\lambda(p_q)(i\gamma^\mu) S(k_q, X; P) \ . \tag{1.62}$$

where $S_\alpha = \langle X|\Psi_\alpha(0)|P\rangle$ encodes the long-distance, soft dynamics at the proton vertex. $\Psi_\alpha(0)$ is the quark field operator which also carries (implicitly here) a colour index and $p_q = k_q + q$. Taking the modulus square of (1.62), integrating over the phase space of the outgoing quark and summing over all unobserved states X, we obtain the following expression for the hadronic tensor:

$$W^{\mu\nu} = \sum_X \int \frac{d^3\vec{p}_q}{2E_q(2\pi)^3} \mathcal{M}^{\mu *}\mathcal{M}^{\nu}(2\pi)^4\delta^4(p_q + p_X - q - P) \tag{1.63}$$

Summing over λ, we can rewrite (1.63) as

$$W^{\mu\nu} = 2\pi \int \frac{d^3\vec{p}_q}{2E_q} \left[\sum_X \bar{S}_\beta(k_q, P) S_\alpha(k_q, P)\delta^4(p_q + p_X - q - P)\right] \xi^{\mu\nu}_{\beta\alpha} \ . \tag{1.64}$$

where we have isolated the short-distance, hard piece:

$$\xi^{\mu\nu}_{\beta\alpha} = (ee_q)^2 \left[(-i\gamma^\mu)(\not{p}_q + m_q)(i\gamma^\nu)\right]_{\beta\alpha} \tag{1.65}$$

Hereafter we use the usual notation, $\not{p}_q = p^\mu_q \gamma_\mu$. In (1.64) and (1.65), we have restored the spinor indices α and β. Let us define

$$\Phi_{\alpha\beta}(k_q, P) = \sum_X \bar{S}_\beta(k_q, P) S_\alpha(k_q, P)\delta^4(p_q + p_X - q - P) \tag{1.66}$$

or equivalently

$$\Phi_{\alpha\beta}(k_q, P) = \sum_X \delta^4(p_q - p_X - q - P)\langle P|\bar{\Psi}_\beta(0)|X\rangle\langle X|\Psi_\alpha(0)|P\rangle \ . \tag{1.67}$$

Using the integral representation of the delta function and translational invariance of the quark field operator, this becomes

$$\Phi_{\alpha\beta}(k_q, P) = \int \frac{d^4z}{(2\pi)^4} e^{ik_q.z}\langle P|\bar{\Psi}_\beta(0)\Psi_\alpha(z)|P\rangle \ . \tag{1.68}$$

Therefore we can write (1.64) as

$$W^{\mu\nu} = 2\pi \int \frac{d^3\vec{p}_q}{2E_q} \mathrm{Tr}[\Phi\xi^{\mu\nu}] \ . \tag{1.69}$$

Using

$$\int \frac{d^3\vec{p}_q}{2E_q} = \int d^4p\delta(p_q^2 - m_q^2)\theta(E_q - m_q) \tag{1.70}$$

(1.69) becomes

$$W^{\mu\nu} = \int d^4p_q \mathrm{Tr}[\Phi\mathcal{E}^{\mu\nu}] = \int d^4k \mathrm{Tr}[\Phi\mathcal{E}^{\mu\nu}] \tag{1.71}$$

where in the second equality, we have chosen to integrate over the momentum of the struck quark instead. In passing we note that $\mathcal{E}^{\mu\nu}$ is the discontinuity of the amputated[8] elastic Compton amplitude [19],

$$\mathcal{E}^{\mu\nu} = \xi^{\mu\nu}\delta(p_q^2 - m_q^2)\theta(E_q - m_q)2\pi = \text{disc.}\mathcal{A}(\gamma^* p \to \gamma^* p) \ . \tag{1.72}$$

The second assumption in the parton model is that the non-perturbative object $\Phi_{\alpha\beta}(k_q, P)$ is strongly damped as the virtual k^2 and the transverse momentum $\boldsymbol{k}$ of the struck quark become large [15]. To see the consequences of this assumption, it is convenient to first define two light-like vector n and l such that $n.l = 1$. Any 4-vector can then be decomposed in the basis spanned by n and l. This is called a Sudakov decomposition.[9] The 4-momenta of the proton and photon can then be written as

$$P^\mu = l^\mu + \frac{M_p^2}{2} n^\mu \approx l^\mu \quad ; \quad q^\mu = (P.q)n^\mu + q_\perp^\mu \ . \tag{1.73}$$

where $q_\perp^2 = -q^2 = Q^2$ and we have neglected the proton's mass. We can write $l^\mu = (P, 0, 0, P)$ and $n^\mu = (1/(2P), 0, 0, -1/(2P))$ where choosing P to be large, selects the *infinite momentum frame* of the proton. In general, it is easy to show that

$$k_q^\mu = \xi P^\mu + \frac{k_q^2 + \boldsymbol{k}_q^2}{2\xi} n^\mu + k_\perp^\mu \tag{1.74}$$

where $K_\perp^\mu = (0, \boldsymbol{k}_q, 0)$. If $\Phi(k_q, P)$ suppresses large values of k_q^2 and $\boldsymbol{k}_q$, the struck quark is *collinear* to the proton,

$$k_q^\mu \approx \xi P^\mu \ . \tag{1.75}$$

and the delta function in (1.70) can be simplified to give

$$\delta((k_q + q)^2 - m_q^2) \approx \frac{1}{2P.q}\delta(\xi - x) \ , \tag{1.76}$$

where we have neglected the quark mass. Projecting out the structure function F_2 from (1.60), we find [15]

$$F_2 = (P.q)n^\mu n^\nu W_{\mu\nu} = (e_q e)^2 x \int d^4k \text{Tr}[\not{n}\Phi(k_q, P)]\delta(\xi - x) \ . \tag{1.77}$$

[8] With external spinors and polarisation vectors removed.

[9] We shall use the Sudakov decomposition technique again in Chapter 2.

Defining the quark distribution function to be

$$f(x) = \int d^4k \mathrm{Tr}[\not{n}\Phi(k_q, P)]\delta(\xi - x) \ , \tag{1.78}$$

we have

$$F_2(x) = (e_q e)^2 x f(x) \ . \tag{1.79}$$

In other words, we see that the structure function F_2 scales

$$F_2(x, Q^2) \to F_2(x) \ . \tag{1.80}$$

At the same time, we have now have a definition (1.78) for the quark distribution function or parton distribution function (pdf). Recalling the definition (1.66), the quark distribution function is expressed in terms of the *diagonal* matrix elements of *bilocal* quark field operators. We can compare this definition with that of elastic form factors defined using *off-diagonal* matrix elements of *local* combinations of quark field operators (see e.g [16])

$$\bar{u}(P', S')[\gamma^\mu F_1(Q^2) + \frac{i\sigma^{\mu\nu}q_\nu}{2M}F_2(Q^2)]u(P, S) = \langle P', S'|\bar{\Psi}(0)\gamma^\mu\Psi(0)|P, S\rangle \ , \tag{1.81}$$

where M is the mass of the proton and we have specified more precisely the proton state by a spin label S. Interpolating between form factors and parton distribution functions, there is a new class of parton distributions functions called *generalised* parton distributions (gpds) defined in terms of *off-diagonal* matrix elements of *bilocal* quark field operators [94],

$$\tilde{\Phi}(P, P', k_q, k_q', S, S') = \int d^4z e^{i\bar{k_q}\cdot z}\langle P', S'|\bar{\Psi}\left(-\frac{z}{2}\right)\Psi\left(\frac{z}{2}\right)|P, S\rangle \ , \tag{1.82}$$

where $\bar{k_q} = (k_q + k_q')/2$. Here, k_q' is the 4-momentum of the returning parton in "handbag" type diagram (c.f Figure 1.5(b)). We shall see later that Deeply Virtual Compton Scattering probes a gpd.

1.4.4 Scaling violations and the DGLAP evolution

In this Section, we follow [15, 21]. Figure 1.6 shows that the structure function F_2 has a slow dependence on Q^2. This departure from scaling is due to QCD corrections

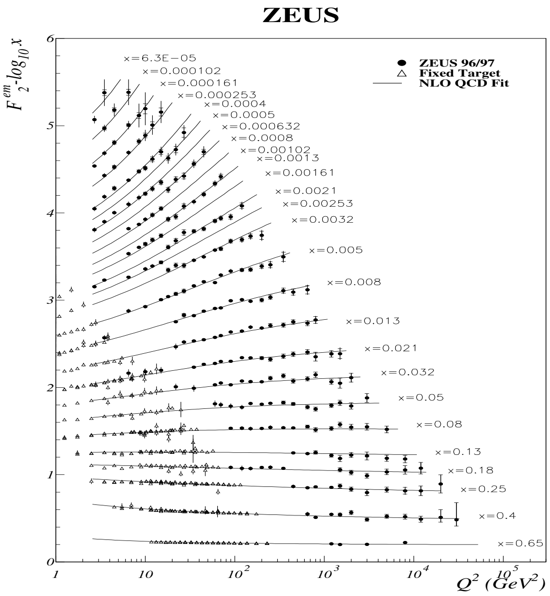

Figure 1.6: Scaling violations of the proton's structure function, $F_2(x, Q^2)$. Results from [37].

to the parton model. Our central assumption that led to Bjorken scaling was that the struck quark had negligible transverse momenta $\boldsymbol{k}$. This is not the case if we take into account gluon emission. The quark can radiate off gluons and acquire large transverse momentum. Figure 1.7 shows that each emitted parton can itself emit another parton, thus forming a ladder structure. In calculating this Feynman diagram one encounters divergences due to soft and collinear emissions. It turns out that soft emission divergences are exactly cancelled by virtual corrections. On the other hand, a regularisation procedure is required for the collinear divergences. Usually an infrared cut-off μ_F is introduced. The pdfs are the redefined (renormalised) to absorb the terms which contain the cut-off and as a result become dependent on it. Then, the perturbatively calculable partonic cross-section is factorised off the pdfs, the factorisation scale being μ_F. Formal proof of factorisation to all orders in perturbation theory can be found in [36]. Symbolically, we write

$$\sigma_{ep} = \sum_i [f_{i/p}(Q^2) \otimes \sigma_{ei}(Q^2)] \ . \tag{1.83}$$

The structure function F_2 is then given by

$$F_2(x,Q^2) = \sum_i \int_x^1 dz C_i \left(\frac{x}{z}, \alpha_s(\mu_R), \frac{Q^2}{\mu_F^2}\right) f_i(z,\mu_F^2) + \text{higher twist terms} \tag{1.84}$$

where μ_F is a factorisation scale and μ_R is the renormalisation scale. C_i are the perturbatively calculable coefficients and f_i are the parton distribution functions, pdfs. The latter are *universal*; once known for a particular process, they can be used for other processes. The factorisation theorem is valid for asymptotic Q^2 and has power corrections as shown in (1.84).[10] The factorisation is said to be *collinear* because all partons in the pdfs are forced to have transverse momenta less than μ_F. In practice, when calculating the ladder diagram, one makes approximations. In that leading to the DGLAP equations, the transverse momenta of partons are strongly ordered as we move up the ladder.

$$Q_0^2 \ll \ldots \ll \boldsymbol{k}_i^2 \ll \boldsymbol{k}_{i+1}^2 \ll \ldots \ll Q^2 \,. \tag{1.85}$$

This gives rise to terms $\propto \alpha_s \ln(Q^2/Q_0^2)$ at each order in pertubation theory and these need to be summed to all orders. This is called the leading log (in $\ln Q^2/Q_0^2$) approximation because at each order in perturbation theory, α_s is accompanied by the same power of $\ln Q^2/Q_0^2$. In this approximation, the evolution equations of the pdfs are the celebrated DGLAP (Dokshitzer-Gribov-Lipatov-Altarelli-Parisi) equations [35],

$$\frac{df_i(x,Q^2)}{d\ln Q^2} = \sum_j \int_x^1 \frac{dz}{z} P_{ij}(z, \alpha_s(Q^2) f_i) \left(\frac{x}{z}, Q^2\right) \,. \tag{1.86}$$

where we have taken $\mu_R^2 = \mu_F^2 = Q^2$. P_{ij} functions are the splitting functions which describe emission of a parton from a parent parton in the ladder structure. The pdf at the input scale Q_0^2 cannot be calculated within pQCD but once extracted from experiment, the DGLAP equations control its evolution with Q^2.

[10] Here, we understand higher twist terms as being suppressed by powers of $(1/Q^2)^n$ where $n \geq 2$. Within the operator product formalism, *twist* is defined as the difference between the mass dimension and spin of an operator [20].

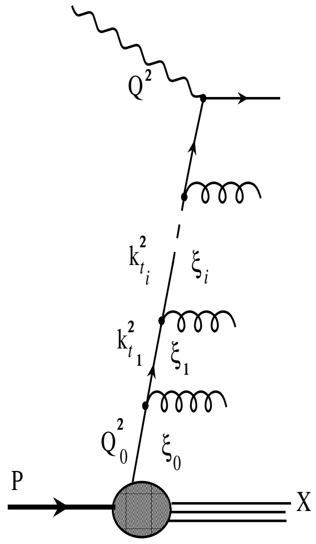

Figure 1.7: QCD corrections to the parton model: A typical ladder diagram.

1.5 Hard diffraction at HERA and the BFKL Pomeron

HERA (Hadron-Elektron-Ring-Anlage) [30] is the accelerator complex in Hamburg, Germany. It is an $e^{\pm}p$ collider operating at present at a centre of mass energy, $S = (k+p)^2$ of $\sim$ 300 GeV, where k and p are the 4-momenta of the proton and electron respectively. The H1 [31] and the ZEUS [32] experiments refer to two different detectors at different locations in the accelerator complex. In recent years, two important discoveries have attracted the attention of the community. The first one is the strong rise of the structure function F_2 with decreasing x, at small x. The second is the presence of rapidity gaps or diffractive events in about 10% of DIS events.

1.5.1 The steep rise of F_2 at small x

In terms of the structure functions, the differential cross-section is given as

$$\frac{d^2\sigma(ep \to eX)}{dxdQ^2} = \frac{2\pi\alpha_{e.m}}{xQ^4}\left[(1+(1-y)^2)F_2(x,Q^2) - y^2F_L(x,Q^2)\right] \ . \tag{1.87}$$

$F_2(x,Q^2)$ and $F_L(x,Q^2)$ are the structure functions of the proton. The structure functions $F_2(x,Q^2)$ and $F_L(x,Q^2)$ are given as:

$$F_2(x,Q^2) = \frac{Q^2}{4\pi^2\alpha_{e.m}}(\sigma_T^{\gamma^* p} + \sigma_L^{\gamma^* p}) \tag{1.88}$$

and

$$F_L(x,Q^2) = \frac{Q^2}{4\pi^2\alpha_{e.m}}\sigma_L^{\gamma^* p} \ . \tag{1.89}$$

(1.88) connects the structure function F_2 to the virtual photon-proton total cross section. We expect the following energy or equivalently x-dependence (at fixed Q^2) in the high energy limit:

$$F_2(x,Q^2) \approx Ax^{-0.08} + Bx^{0.45} \ . \tag{1.90}$$

as is the case for hadron-hadron and real photon-hadron scattering. This is true for $0.01 \leq x \leq 0.1$. However, for lower x, both the H1 [33] and ZEUS [34] data reveal a steeper x dependence (typically $\sim x^{-0.3}$) as can be clearly seen in Figure 1.8. Such an x dependence deviates from the soft Pomeron exchange picture and is expected within pQCD as we shall see next.

At very large energy (or very small x), logarithms ($\alpha_s \ln(1/x)$) appear and spoil the convergence of the perturbative series. In this regime and at moderate Q^2, the DGLAP equations are no longer valid and resummation of terms in $\ln(1/x)$ is done by the BFKL equation [38]. There is no more ordering in the transverse momenta $\boldsymbol{k}_i$ but instead the momentum fractions ξ_i are strongly ordered as we move up the ladder. It is then necessary to generalise collinear factorisation to the so-called k_T factorisation. The BFKL equation is an evolution equation of the *unintegrated gluon density*, $\mathcal{F}(x,\boldsymbol{k})$[11]

$$\frac{\partial \mathcal{F}(x,\boldsymbol{k})}{\partial \ln(1/x)} = \frac{3\alpha_s}{\pi}\boldsymbol{k}^2 \int_0^\infty \frac{d\boldsymbol{k}'}{\boldsymbol{k}'}\left[\frac{\mathcal{F}(x,\boldsymbol{k}'^2) - \mathcal{F}(x,\boldsymbol{k}^2)}{|\boldsymbol{k}'^2 - \boldsymbol{k}^2|} + \frac{\mathcal{F}(x,\boldsymbol{k}^2)}{\sqrt{4\boldsymbol{k}'^4 + \boldsymbol{k}^4}}\right] \tag{1.91}$$

where the unintegrated gluon density is related (at leading twist) to the ordinary gluon density via

$$xg(x,Q^2) = \int_0^{Q^2} \frac{d\boldsymbol{k}^2}{\boldsymbol{k}^2}\mathcal{F}(x,\boldsymbol{k}) \ . \tag{1.92}$$

[11] We shall meet this quantity again in Chapter 2.

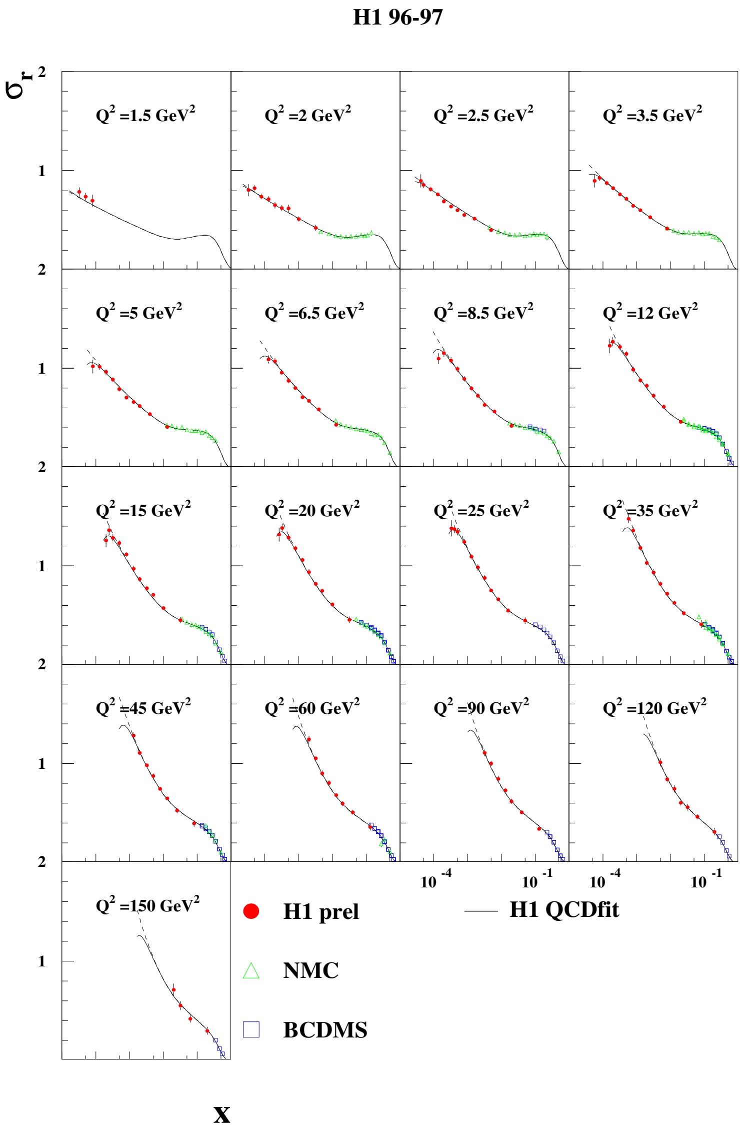

Figure 1.8: The strong rise of F_2 at small x. Figure from [22].

An analytic solution of the BFKL equation shows that

$$F_2(x, Q^2) \approx xg(x, Q^2) \propto x^{-\lambda} \tag{1.93}$$

where at fixed α_s,

$$\lambda = \frac{12 \ln 2}{\pi} \alpha_s \approx 0.4 \; . \tag{1.94}$$

which means that total cross-sections go like

$$\sigma_{\text{tot}} \approx s^{0.4} \; . \tag{1.95}$$

This suggest another Pomeron intercept, usually called the *hard* or BFKL Pomeron which describe photon-hadron interaction at high energy and Q^2 sufficiently high to provide a hard scale. Note that (1.95) is correct to leading $\ln(1/x)$ and next to leading order corrections are important [39].

1.5.2 Diffraction in DIS

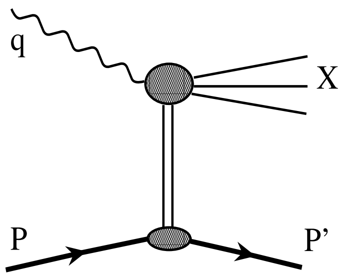

Figure 1.9: Diffractive Deep Inelastic Scattering (DDIS) via Pomeron exchange, denoted here by the double lines. The 4-momenta shown are defined in the text.

In DIS, the relation to Pomeron exchange is via the optical theorem. The Pomeron can enter a subprocess of DIS where the proton remains intact and there is a large rapidity gap between the final dissociation products of the photon and the proton. This is sometimes called diffractive DIS:

$$\gamma^*(q) + p(P) \to p(P') + X \quad .$$

Three additional variables are needed to fully specify the kinematics. The first one is the Mandelstam variable t and the two others are

$$x_{\mathcal{P}} = \frac{q.(P-P')}{q.P} \quad ; \quad \beta = \frac{x}{x_{\mathcal{P}}} \, . \tag{1.96}$$

where β plays an analogous role to that of x in DIS. One then defines the four-fold differential cross-section [44]

$$\frac{d^4\sigma(ep \to Xp)}{d\beta dQ^2 dx_{\mathcal{P}} dt} = \frac{2\pi\alpha_{e.m}^2}{\beta Q^4}\left[(1+(1-y)^2)F_2^{D(4)}(\beta, Q^2, x_{\mathcal{P}}, t) - y^2 F_L^{D(4)}(\beta, Q^2, x_{\mathcal{P}}, t)\right] \tag{1.97}$$

and integrating out t, we get the diffractive structure function $F_2^{D(3)}$,

$$F_2^{D(3)}(\beta, Q^2, x_{\mathcal{P}}) = \int dt F_2^{D(4)}(t, x_{\mathcal{P}}, \beta, Q^2) \, . \tag{1.98}$$

1.5.3 Exclusive diffractive processes

Figure 1.10: Exclusive photon production and exclusive meson production via Pomeron exchange, denoted by double lines. The 4-momenta shown are defined in the text.

An exclusive process as defined by Feynman [47] is one in which the kinematics of all initial and final state particles are specified. In this thesis, we shall explore two diffractive exclusive processes. The first one is Deeply virtual Compton Scattering as shown in Figure 1.10 (a):

$$\gamma^*(q) + p(P) \to p(P') + \gamma(q') \quad ; \quad q'^2 = 0 \ ,$$

with a real photon in the final state. Data for DVCS has been published by H1 [45] and more recently, the ZEUS collaboration has released preliminary data [46] on both the Q^2 and W dependencies of the DVCS cross-section. The second is vector meson production as shown in Figure 1.10 (b):

$$\gamma^*(q) + p(P) \to V(p_v) + p(p') \ ,$$

where V is either the ρ, ϕ or J/Ψ vector meson. Note that vector meson production satisfies the definition of a diffractive process as proceeding by vacuum (Pomeron) exchange since the vector meson carries the same quantum numbers as the photon. It is also for this reason that it is now common in the literature to refer to this process as an elastic process. Strictly speaking, both DVCS and vector meson production are *not* elastic processes. Using (1.10), we find that the lower limit for t is

$$t_{\text{min}} = (M_v^2 + Q^2)^2 \frac{M_p^2}{s^2} \tag{1.99}$$

where M_p is the mass of the proton. At high s, t_{min} is small and $t \approx t_{\text{min}}$ because larger t is suppressed by the elastic form factor of the proton (since we insist that the proton remains intact). Therefore $t \approx 0$ can be considered to be a good approximation. For exclusive processes, factorisation theorems have been proven at the *amplitude* level [48]. We shall only briefly touch upon these theorems later. Our work will be focused on an analysis of these exclusive processes within the *colour dipole model*.

1.6 Summary

This chapter has been a summary in itself. Perphaps the central idea is that in a physical process we always have a pertubatively non-calculable piece and that factorisation theorems in QCD allow us to seperate neatly the non-perturbative piece (lumped into pdfs) from the perturbative piece. In what follows, we shall explore and use the colour dipole model, in which the factorisation idea is still present. A major difference is that we shall switch from the proton's infinite momentum frame to one in which the proton is at rest. Hence, we shall probe the structure of the virtual photon instead of that of the proton. The most basic picture is the following: In the proton's rest frame, the photon fluctuates into a quark-antiquark pair which then interacts strongly with the proton, the two processes being characterised by very different time-scales. The splitting of the photon into a dipole of small transverse size is treated within perturbation theory. The interaction of the dipole with the proton is encoded in the dipole cross-section. We might be tempted to think that the dipole cross-section is purely non-perturbative. Nevertheless, if the transverse size of the $q\bar{q}$ is small enough, the interaction is governed by pQCD. The mixture of long-distance and short-distance physics is then controlled by the relative contribution of dipoles of different sizes in a particular process.

We shall expand these ideas and derive the essential equations of the dipole model in Chapter 2. Chapter 3 and 4 are devoted to an analysis of DVCS and vector meson production within the colour dipole model. We conclude in Chapter 5.

Chapter 2

The colour dipole model

2.1 Introduction

The first five sections of this chapter provide the theoretical basis of the colour dipole model. Our starting point is pQCD. We calculate the *high energy limit* helicity amplitudes for $q\bar{q}$ production in virtual photon-quark scattering, via one gluon exchange. We express these amplitudes in terms of the *light-cone photon wavefunctions* which we define and extract for all possible helicity configurations. We then discuss the physical meaning of light-cone wavefunctions within the framework of light-cone quantisation. We progress to two gluon exchange and calculate the amplitude for (quark) elastic Compton scattering, $\gamma^* q \to \gamma^* q$. Introducing the unintegrated gluon distribution, we replace the quark by a proton and show how the elastic Compton amplitude factorises (in impact parameter space) into light-cone photon wavefunctions and the dipole cross-section, the latter being defined in terms of the unintegrated gluon distribution. We next present a much more general formulation of the colour dipole model, *valid beyond perturbation theory* and show how we reach the same factorisation at the amplitude level for (proton) elastic Compton Scattering. We discuss how the dipole model is used to investigate various physical processes.

In the final sections, we present in detail two different models for the dipole cross-section which we shall use in later chapters.

2.2 The photon light-cone wavefunctions

2.2.1 Derivation within covariant perturbation theory

We start by calculating the amplitude for $\gamma^* q \to q\bar{q} + q$, with one gluon exchanged in the t channel, as shown in Figure 2.1. In doing so, we shall define and extract a very important object: the light-cone photon wavefunction. *The light-cone photon wavefunction is the probability amplitude for finding a* $q\bar{q}$ pair *in the photon.* Before discussing how this interpretation arises, we shall first derive explicit expressions for the complete set of light-cone photon wavefunctions in the $q\bar{q}$ helicity basis. Expressions for the modulus squared (summation over all quark-antiquark helicities is

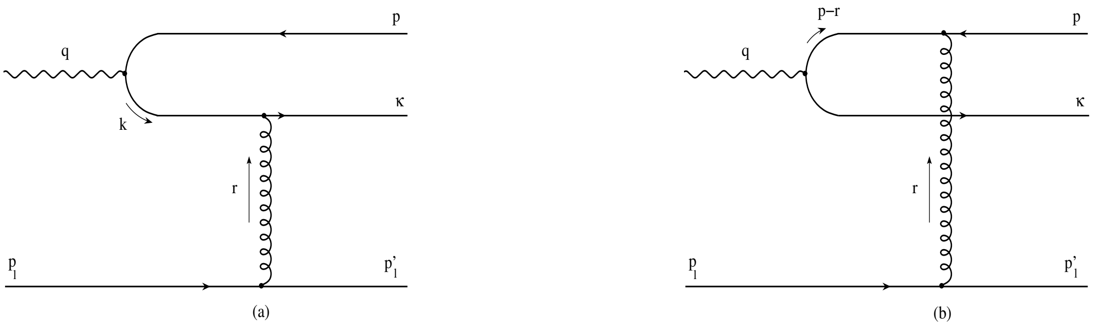

Figure 2.1: One gluon exchange Feynman diagram for $\gamma^* q \to \gamma q\bar{q} + q$. The 4-momenta are given in brackets and defined in the text. Note that both diagrams need to be considered to give a gauge invariant amplitude.

implicitly carried out) of the longitudinally and transversely polarised photon light-cone wavefunctions are given in [49] and are derived in e.g [3]. In [50], the authors derive the photon light-cone wave functions in the helicity basis of the quark-antiquark pair, limited to massless (anti)quark. This is extended to massive (anti)quark in [51]. *Here, we follow closely* [51], *the only difference being that we use the helicity method of* [53] *rather than that proposed in* [51].

The notation is as follows: The subscript in brackets on amplitudes refer to the figure representing the amplitude. For instance, $\mathcal{A}_{(2.1)}$ means the amplitude corresponding to the Feynman diagram in Figure 2.1. For a 4-vector p^μ, $\not{p} = \gamma^\mu p_\mu$, where summation over repeated indices is implied. Conventional Dirac spinors are denoted as usual (for e.g $u_h(\kappa)$) where h denotes the helicity of the Dirac particle and κ its 4-momentum.

Defining the light-like vectors p' and q' as

$$p' \equiv \frac{\sqrt{s}}{2}(1, \mathbf{0}, -1) \qquad\qquad q' \equiv \frac{\sqrt{s}}{2}(1, \mathbf{0}, 1)\ , \tag{2.1}$$

we make a Sudakov decomposition of all 4-momenta as follows:

$$q = q' - xp' \quad ; \quad x = \frac{Q^2}{s} \tag{2.2}$$

$$p_l = p' \tag{2.3}$$

$$k = \alpha q' + \beta p' + k_\perp \tag{2.4}$$

$$r = \alpha' q' + x_g p' + r_\perp \tag{2.5}$$

In this way, we have $2p'.q' = s$ and $-q^2 = Q^2$. Note that although the lower quark is taken to be massless, we allow the upper quark (antiquark), of flavour f, to have a non-vanishing mass m_f. Putting the outgoing lower quark on-shell, we find that $\alpha' = t/s$. Hence terms proportional to α' are subleading in s and can be neglected in the high energy limit. In what follows, we shall neglect α' compared to α. There is no *a priori* reason to do this. Nevertheless, we find that keeping α' compared to α only gives terms (at the amplitude level) proportional to α' which anyway do not survive the high energy limit. Therefore it is legitimate (and convenient) to neglect α' compared to α from the very beginning of the calculation. Putting the outgoing antiquark on-shell, we find

$$\beta = -x - \frac{\boldsymbol{k}^2 + m_f^2}{(1-\alpha)s} \tag{2.6}$$

which means that β is suppressed by a factor of $1/s$. Likewise, from the on-shell condition for the outgoing upper quark gives

$$x_g = x + \frac{m_f^2 + (1-\alpha)(\boldsymbol{k}+\boldsymbol{r})^2 + \alpha \boldsymbol{k}^2}{\alpha(1-\alpha)s} \,. \tag{2.7}$$

The second term in (2.7) is sometimes called the transverse invariant mass, M_t, of the outgoing $q\bar{q}$ pair in the photon-gluon fusion process, $\gamma^* g \to q\bar{q}$ [65]. (2.7) shows that x_g is also supressed by a factor $1/s$. An immediate consequence is that, in the high energy limit, the 4-momentum of the gluon is mainly transverse:

$$t = r^2 = \alpha' x_g s + r_\perp^2 \approx -\boldsymbol{r}^2 \,. \tag{2.8}$$

Note that we *cannot* neglect x_g compared to β since both are suppressed in the high energy limit. For the lower quark line, we assume that the emitted gluon is soft compared to the fast moving quark so that[1]

$$-ig_s \tau^a_{ij} \bar{u}_{\lambda'}(p_l') \gamma^\mu u_\lambda(p_l) = -2ig_s \tau^a_{ij} p_l^\mu \delta_{\lambda\lambda'} \,, \tag{2.9}$$

where g_s is the strong coupling constant and τ^a_{ij} are the generators of the colour group in the fundamental representation. The delta function $\delta_{\lambda'\lambda}$ expresses conservation of

[1]This is the eikonal approximation [3].

the fast moving, massless lower quark's helicity upon soft gluon emission. The Lorentz index μ in (2.9) contracts with the gluon propagator[2]

$$D^{\mu\nu} = \frac{-ig^{\mu\nu}}{r^2}\delta^{ab} \; . \tag{2.10}$$

Putting everything together, we arrive at the following expression for the total amplitude

$$\mathcal{A}_{h\bar{h}(2.1)} = -\frac{2g_s^2}{t} e e_f \delta_{\lambda\lambda'} \mathcal{C} \bar{u}_h(\kappa) \Big[\frac{\Gamma_a}{\Delta_a} - \frac{\Gamma_b}{\Delta_b}\Big] v_{\bar{h}}(p) \tag{2.11}$$

with

$$\kappa = k + r \quad \text{and} \quad p = q - k \; . \tag{2.12}$$

$\mathcal{C}$ is the colour factor. e is the electronic charge, e_f is the fraction of electronic charge carried by a quark of flavour f. h and $\bar{h}$ denote the helicities of the quark and antiquark respectively. In what follows, $\bar{h}$ or $h = +(-)$ means the helicity of the quark or antiquark is $\frac{1}{2}(-\frac{1}{2})$. Γ_a and Γ_b are defined below:

$$\Gamma_a = \not{p}' (\not{k} + m_f) \not{\varepsilon} \tag{2.13}$$

$$\Gamma_b = \not{\varepsilon} (\not{p} - \not{r} + m_f) \not{p}' \tag{2.14}$$

where ε is the photon polarisation vector. We make the following choice for the polarization vectors of the longitudinal and transverse photon:

$$\varepsilon_L = \frac{1}{Q}(q' + xp') \quad ; \quad \varepsilon_T(\pm) = \frac{1}{\sqrt{2}}(0, 1, \gamma i, 0) \text{ with } \gamma = \pm \; . \tag{2.15}$$

The denominator of the quark propagator in diagram 2.1(a) is given by $\Delta_a = k^2 - m_f^2$. Using (2.4) it is straightforward to show that

$$\Delta_a = -\frac{1}{1-\alpha}[\alpha(1-\alpha)Q^2 + \mathbf{k}^2 + m_f^2] \; . \tag{2.16}$$

Similarly, for the antiquark propagator in diagram 2.1(b), we have $\Delta_b = (p-r)^2 - m_f^2$. Using (2.2), (2.4) and (2.5) we arrive at

$$\Delta_b = -\frac{1}{\alpha}[\alpha(1-\alpha)Q^2 + (\mathbf{k}+\mathbf{r})^2 + m_f^2] \; . \tag{2.17}$$

[2]In [51], the metric tensor decomposition, $g_{\mu\nu} = \frac{2}{s}(q'_\mu p'_\nu + q'_\nu p'_\mu + g^{\perp}_{\mu\nu})$, is used. While this is a very useful trick in calculating high energy limit amplitudes in general, it is unnecessary here.

Going back to the numerator of (2.11), we use the Dirac equation to write :

$$\bar{u}_h(\kappa)\Gamma_a v_{\bar{h}}(p) = \bar{u}_h(\kappa)[\alpha s \not{\epsilon} - \not{p}_l' \not{p}_l \not{\epsilon}]v_{\bar{h}}(p) \ , \tag{2.18}$$

and similarly

$$\bar{u}_h(\kappa)\Gamma_b v_{\bar{h}}(p) = \bar{u}_h(\kappa)[(1-\alpha)s \not{\epsilon} + \not{\epsilon} \not{p}_l' \not{p}_l]v_{\bar{h}}(p) \ . \tag{2.19}$$

We want to calculate the amplitude for each possible helicity configuration. Let us now introduce the helicity method [53] we are going to use. The first (trivial) step is to rewrite the generic expression $\bar{u}\Gamma_i v$ as a trace :

$$\bar{u}_h(\kappa)\Gamma_i v_{\bar{h}}(p) = \mathrm{Tr}(v_{\bar{h}}(p) \otimes \bar{u}_h(\kappa)\Gamma_i) \quad ; \quad i = a, b \ . \tag{2.20}$$

Then, the tensor product of spinors is expressed in terms of the 4-momenta of the quark, antiquark and two auxilliary vectors p_0 and η. The latter vectors are chosen[3] as $p_0 = (1, 0, 0, -1)$ and $\eta = (0, \frac{1}{2}, -\frac{i}{2}, 0)$. Explicit expressions for the different spinor pairs and helicity configurations are given in [53]. The one we need is

$$v_{\bar{h}}(p) \otimes \bar{u}_h(\kappa) = \mathcal{N}(m_f - \not{p}) \left\{ \begin{array}{cc} -(1+\gamma_5) \not{\eta} & 1+\gamma_5 \\ 1-\gamma_5 & (1-\gamma_5) \not{\eta}^* \end{array} \right\} \not{p}_0(m_f + \not{\kappa}) \ , \tag{2.21}$$

where

$$\mathcal{N} = \frac{1}{4\sqrt{(p.p_0)(\kappa.p_0)}} \ . \tag{2.22}$$

Note that (2.21) is *not* a matrix equation, but rather just a compact notation to show the dependence on the quark-antiquark helicities, $\bar{h}$ and h, the rule being $\left\{ \begin{array}{cc} ++ & +- \\ -+ & -- \end{array} \right\}$.

In our case, it is easy to show that

$$\mathcal{N} = \frac{1}{4\sqrt{(1-\alpha)\alpha s}} \ . \tag{2.23}$$

For convenience, we shall not substitute for $\mathcal{N}$ until it comes to evaluate the amplitude.

Let us start with the case when the photon is transversely polarised. We need to do a little algebraic manipulation first. We expand the string of γ matrices in the second term in (2.18) and (2.19) onto a Dirac basis. Since the number of γ matrices is odd, we have (see e.g [55])

$$\not{p}_l' \not{p}_l \not{\epsilon} = \not{v} + \not{a}\gamma^5 \tag{2.24}$$

[3]They must satisfy the relation $\not{p}_0 = i\gamma_5 \not{\eta}_1 \not{\eta}_2 \not{p}_0$ where $\eta = \eta_1 + i\eta_2$ [53].

with

$$v^\mu = p_l'^\mu (p_l.\varepsilon) - p_l^\mu (p_l'.\varepsilon) + \varepsilon^\mu (p_l'.p_l) \tag{2.25}$$

and

$$a^\mu = i\epsilon^{\mu\nu\lambda\sigma} p'_{l_\nu} p_{l_\lambda} \varepsilon_\sigma \ . \tag{2.26}$$

Plugging in the polarization vector for the transverse photon gives

$$\Gamma_a = \alpha s \ \not{\varepsilon}_T + \boldsymbol{\varepsilon_T.r} \ \not{p}' - i \ \not{\epsilon}_T \gamma_5 \ . \tag{2.27}$$

A similar calculation using (2.19) gives

$$\Gamma_b = (1-\alpha) s \ \not{\varepsilon}_T + \boldsymbol{\varepsilon_T.r} \ \not{p}' + i \ \not{\epsilon}_T \gamma_5 \tag{2.28}$$

where in both (2.27) and (2.28),

$$\not{\epsilon}_T = \epsilon^{\mu\nu\lambda\sigma} p'_{l_\nu} p_{l_\lambda} \varepsilon_{T_\sigma} \gamma_\mu \ . \tag{2.29}$$

Here, $\epsilon^{\mu\rho\sigma\lambda}$ is the totally antisymmetric tensor, with $\epsilon^{0123} = -1$. We have to calculate $\bar{u}_h(\kappa)\Gamma_i v_{\bar{h}}(p) = \mathrm{Tr}\left[v_{\bar{h}}(p) \otimes u_h(\kappa)\Gamma_i\right]$ with $\Gamma_i (i = a, b)$ as given by (2.27) or (2.28). We are now ready to use the helicity method.

Consider the case $\bar{h} = +$ and $h = -$. Picking up the $1 + \gamma_5$ entry of (2.21), we find that

$$\mathrm{Tr}[v_+(p) \otimes \bar{u}_-(\kappa) \ \not{\varepsilon}] = \mathcal{N}\left[\mathrm{Tr}(\gamma_5 \ \not{p} \ \not{p}_0 \ \not{\kappa} \ \not{\varepsilon}_T) - \mathrm{Tr}(\not{p} \ \not{p}_0 \ \not{\kappa} \ \not{\varepsilon}_T)\right] \ , \tag{2.30}$$

$$\mathrm{Tr}[v_+(p) \otimes \bar{u}_-(\kappa) \ \not{p}'] = \mathcal{N}\left[\mathrm{Tr}(\gamma_5 \ \not{p} \ \not{p}_0 \ \not{\kappa} \ \not{p}') - \mathrm{Tr}(\not{p} \ \not{p}_0 \ \not{\kappa} \ \not{p}')\right] \ , \tag{2.31}$$

and

$$\mathrm{Tr}[v_+(p) \otimes \bar{u}_-(\kappa) \ \not{\epsilon}_T \gamma_5] = \mathcal{N}\left[\mathrm{Tr}(\not{p} \ \not{p}_0 \ \not{\kappa} \ \not{\epsilon}_T) - \mathrm{Tr}(\gamma_5 \ \not{p} \ \not{p}_0 \ \not{\kappa} \ \not{\epsilon}_T)\right] \ , \tag{2.32}$$

where we have neglected terms in m_f^2. Using the usual trace theorems [54], we evaluate (2.30), (2.31) and (2.32). Defining $\underline{k} = k_x + i\gamma k_y$ and $\underline{r} = r_x + i\gamma r_y$, we arrive at

$$\mathrm{Tr}[v_+(p) \otimes \bar{u}_-(\kappa) \ \not{\varepsilon}_T] = \mathcal{N} 2\sqrt{2}\sqrt{s}\left[\gamma \underline{k} + \gamma(1-\alpha)\underline{r} - \alpha \underline{k} + (1-\alpha)(\underline{k} + \underline{r})\right] \ , \tag{2.33}$$

and

$$\mathrm{Tr}[v_+(p) \otimes \bar{u}_-(\kappa) \ \not{p}'] = -\mathcal{N} 4 s \sqrt{s} \alpha (1-\alpha) \ , \tag{2.34}$$

$$\mathrm{Tr}[v_+(p) \otimes \bar{u}_-(\kappa)\ \not{\epsilon}_T \gamma_5] = -\mathcal{N} i 2\sqrt{2}s\sqrt{s}\alpha(1-\alpha)\gamma \underline{r}\ . \qquad (2.35)$$

Using the above expressions together with (2.27) and (2.28), we find that

$$\mathrm{Tr}[v_+(p) \otimes \bar{u}_-(\kappa)\Gamma_a] = \mathcal{N}\alpha 2\sqrt{2}s\sqrt{s}(1+\gamma-2\alpha)(\underline{k}) \qquad (2.36)$$

and

$$\mathrm{Tr}[v_+(p) \otimes \bar{u}_-(\kappa)\Gamma_b] = \mathcal{N}(1-\alpha) 2\sqrt{2}s\sqrt{s}(1+\gamma-2\alpha)(\underline{k}+\underline{r})\ . \qquad (2.37)$$

If $\gamma = +$, using (2.36) and (2.37) together with (2.16) and (2.17) we rewrite the amplitude (2.11) as[4]

$$\mathcal{A}_{-+}^{T(\gamma=+)} = 2g_s^2 \frac{s}{t} \delta_{\lambda'\lambda} \mathcal{C}\sqrt{\alpha(1-\alpha)} \left[\Psi_{-+}^{T(\gamma=+)}(\boldsymbol{k},\alpha) - \Psi_{-+}^{T(\gamma=+)}(\boldsymbol{k}+\boldsymbol{r},\alpha)\right] \qquad (2.38)$$

where we have defined and extracted the transverse light-cone photon wavefunction,

$$\Psi_{-+}^{T(\gamma=+)}(\boldsymbol{k},\alpha) = \frac{\sqrt{2}ee_f(1-\alpha)(k_x+ik_y)}{\alpha(1-\alpha)Q^2+\boldsymbol{k}^2+m_f^2} \qquad (2.39)$$

for the helicity configuration $\gamma = +$, $\bar{h} = +$ and $h = -$. Here $\Psi_{+-}^{T(\gamma=+)}(\boldsymbol{k}+\boldsymbol{r},\alpha)$ is given by the same expression (2.39) with the replacement $\boldsymbol{k} \to \boldsymbol{k}+\boldsymbol{r}$.[5] Likewise, for $\gamma = -$, we find

$$\mathcal{A}_{-+}^{T(\gamma=-)} = 2g_s^2 \frac{s}{t} \delta_{\lambda'\lambda} \mathcal{C}\sqrt{\alpha(1-\alpha)} \left[\Psi_{-+}^{T(\gamma=-)}(\boldsymbol{k},\alpha) - \Psi_{-+}^{T(\gamma=-)}(\boldsymbol{k}+\boldsymbol{r},\alpha)\right] \qquad (2.40)$$

with

$$\Psi_{-+}^{T(\gamma=-)}(\boldsymbol{k},\alpha) = -\frac{\sqrt{2}ee_f\alpha(k_x-ik_y)}{\alpha(1-\alpha)Q^2+\boldsymbol{k}^2+m_f^2}\ . \qquad (2.41)$$

The calculation for helicity amplitudes for the helicity configurations ($\gamma = -$, $\bar{h} = -$, $h = +$) and ($\gamma = +$, $\bar{h} = -$, $h = +$) is a repetition of the above, using instead the $1-\gamma_5$ entry of (2.21). We extract the following wavefunctions:

$$\Psi_{+-}^{T(\gamma=-)}(\boldsymbol{k},\alpha) = \frac{\sqrt{2}ee_f(1-\alpha)(k_x-ik_y)}{\alpha(1-\alpha)Q^2+\boldsymbol{k}^2+m_f^2}\ , \qquad (2.42)$$

$$\Psi_{+-}^{T(\gamma=+)}(\boldsymbol{k},\alpha) = -\frac{\sqrt{2}ee_f\alpha(k_x+ik_y)}{\alpha(1-\alpha)Q^2+\boldsymbol{k}^2+m_f^2}\ . \qquad (2.43)$$

[4] In order not to overload the notation, we drop the subscript 2.1 till the end of this section in which we are always refering to the amplitude of Figure 2.1.

[5] For the other helicity configurations as well, $\Psi_{h\bar{h}}^{T(\gamma)}(\boldsymbol{k}+\boldsymbol{r},\alpha)$ is given by the corresponding expression for $\Psi_{h\bar{h}}^{T(\gamma)}(\boldsymbol{k},\alpha)$ with this replacement.

Note that the photon's helicity tends to follow the faster quark or antiquark [44]. For e.g if α is large, $\Psi_{-+}^{T(\gamma=-)}$ dominates over $\Psi_{+-}^{T(\gamma=-)}$.

In all the non-vanishing helicity amplitudes we have calculated so far, the quark and antiquark have opposite helicities ($h = -\bar{h}$). Had we taken the quark (antiquark) to be massless, this would be the complete set of helicity amplitudes. However, with a finite quark mass, we find that for the transversely polarised photon, helicity amplitudes (proportional to the quark mass) survive in which the quark and antiquark have same helicities. Indeed, for $h = +$ and $\bar{h} = +$, using the $-(1+\gamma_5)\ \not{n}$ entry of (2.21) we find

$$\mathrm{Tr}[v_+(p)\otimes\bar{u}_+(\kappa)\ \not{\epsilon}_T] = -\mathcal{N}m_f\mathrm{Tr}\left[\not{n}\ \not{p}_0\ \not{\kappa}\ \not{\epsilon}_T - \not{p}\ \not{n}\ \not{p}_0\ \not{\epsilon}_T + \gamma_5\ \not{n}\ \not{p}_0\ \not{\kappa}\ \not{\epsilon}_T + \gamma_5\ \not{p}\ \not{n}\ \not{p}_0\ \not{\epsilon}_T\right] , \tag{2.44}$$

$$\mathrm{Tr}[v_+(p)\otimes\bar{u}_+(\kappa)\ \not{p}'] = -\mathcal{N}m_f\mathrm{Tr}\left[\not{n}\ \not{p}_0\ \not{\kappa}\ \not{p}' - \not{p}\ \not{n}\ \not{p}_0\ \not{p}' + \gamma_5\ \not{n}\ \not{p}_0\ \not{\kappa}\ \not{p}' + \gamma_5\ \not{p}\ \not{n}\ \not{p}_0\ \not{p}'\right] , \tag{2.45}$$

$$\mathrm{Tr}[v_+(p)\otimes\bar{u}_+(\kappa)\ \not{\epsilon}_T\gamma_5] = \mathcal{N}m_f\mathrm{Tr}\left[\not{n}\ \not{p}_0\ \not{\kappa}\ \not{\epsilon}_T + \not{p}\ \not{n}\ \not{p}_0\ \not{\epsilon}_T + \gamma_5\ \not{n}\ \not{p}_0\ \not{\kappa}\ \not{\epsilon}_T - \gamma_5\ \not{p}\ \not{n}\ \not{p}_0\ \not{\epsilon}_T\right] . \tag{2.46}$$

Using the trace theorems, we evaluate (2.44), (2.45) and (2.46) to arrive at

$$\mathrm{Tr}[v_+(p)\otimes\bar{u}_+(\kappa)\ \not{\epsilon}_T] = \mathcal{N}m_f 2\sqrt{2}(1+\gamma)\sqrt{s}\ , \tag{2.47}$$

$$\mathrm{Tr}[v_+(p)\otimes\bar{u}_+(\kappa)\ \not{p}'] = 0\ , \tag{2.48}$$

$$\mathrm{Tr}[v_+(p)\otimes\bar{u}_+(\kappa)\ \not{\epsilon}_T\gamma_5] = 0\ , \tag{2.49}$$

Using (2.27) and (2.28), we find that

$$\mathrm{Tr}\left(v_+(p)\otimes\bar{u}_+(\kappa)\Gamma_a\right) = \alpha\mathcal{N}m_f 2\sqrt{2}s\sqrt{s}(1+\gamma)\ , \tag{2.50}$$

and

$$\mathrm{Tr}\left(v_+(p)\otimes\bar{u}_+(\kappa)\Gamma_b\right) = (1-\alpha)\mathcal{N}m_f 2\sqrt{2}s\sqrt{s}(1+\gamma)\ , \tag{2.51}$$

Consider the case $\gamma = +$. Using (2.50) and (2.51) together with (2.16) and (2.17), we can write the amplitude (2.11) as

$$\mathcal{A}_{++}^{T(\gamma=+)} = 2g_s^2\frac{s}{t}\delta_{\lambda'\lambda}\mathcal{C}\sqrt{\alpha(1-\alpha)}[\Psi_{++}^{T(\gamma=+)}(\boldsymbol{k},\alpha) - \Psi_{++}^{T(\gamma=+)}(\boldsymbol{k}+\boldsymbol{r},\alpha)] \tag{2.52}$$

with

$$\Psi^{T(\gamma=+)}_{++}(\boldsymbol{k},\alpha) = \frac{\sqrt{2}ee_f m_f}{\alpha(1-\alpha)Q^2 + \boldsymbol{k}^2 + m_f^2} \,, \tag{2.53}$$

On the other hand, for $\gamma = -$, both (2.50) and (2.51) vanish. Thus we have

$$\mathcal{A}^{T(\gamma=-)}_{++} = 0 \quad ; \quad \Psi^{T(\gamma=-)}_{++}(\boldsymbol{k},\alpha) = 0 \,. \tag{2.54}$$

We extract a similar expression for the photon light-cone wavefunction in the helicity configuration ($\gamma = -$ and $h = -$, $\bar{h} = -$),

$$\Psi^{T(\gamma=-)}_{--}(\boldsymbol{k},\alpha) = \frac{\sqrt{2}ee_f m_f}{\alpha(1-\alpha)Q^2 + \boldsymbol{k}^2 + m_f^2} \,. \tag{2.55}$$

and similarly

$$\mathcal{A}^{T(\gamma=+)}_{--} = 0 \quad ; \quad \Psi^{T(\gamma=+)}_{--}(\boldsymbol{k},\alpha) = 0 \,. \tag{2.56}$$

(2.39), (2.41), (2.42), (2.43),(2.53) and (2.55) are the transverse light-cone photon wavefunctions.

Notice that in (2.53) and (2.55), helicity is conserved at the $\gamma^* \to q\bar{q}$,

$$\frac{h + \bar{h}}{2} = \gamma \tag{2.57}$$

as one would expect in the non-relativistic case. In the relativistic limit, the quark mass becomes negligible and these amplitudes (or photon light-cone wavefunctions) vanish and the only non-vanishing photon light-cone wavefunctions would be (2.39), (2.41), (2.42), (2.43) where helicity is *not* conserved during the $\gamma \to q\bar{q}$ transition.[6] Of course, total angular momentum is always conserved and that is why these photon light-cone wavefunctions are proportional to the relative transverse momentum $\boldsymbol{k}$ of the $q\bar{q}$ pair ; the pair is allowed to have orbital angular momentum so that the identity

$$J_z = L_z + S_z \tag{2.58}$$

is satisfied. Now for the case of heavy quarks, the terms proportional to the quark mass become important and the terms proportional to $\boldsymbol{k}$ are refered to as relativistic corrections. We shall come back to these ideas in Chapter 4 when we calculate the amplitude for vector meson production.

[6] Put another way, helicity is conserved along the fermion line.

Now for longitudinal case. Here, *invoking gauge invariance beautifully simplifies the calculation*. Due to gauge invariance, the total amplitude vanishes if in Γ_a and Γ_b, we substitute the photon 4 momentum q^μ for the photon polarisation vector ε_L^μ (See e.g [54]). This means that

$$\bar{u}_h(\kappa)\frac{\Gamma_a}{\Delta_a}v_{\bar{h}}(p)\mid_{(\varepsilon_L\to q)}=\bar{u}_h(\kappa)\frac{\Gamma_b}{\Delta_b}v_{\bar{h}}(p)\mid_{(\varepsilon_L\to q)} \ . \tag{2.59}$$

Using the polarisation vector (2.15) for the longitudinal photon and the above relation, together with (2.11), we derive the following simple expression for the total amplitude:

$$\mathcal{A}^L_{h\bar{h}}=-ee_f\mathcal{C}\frac{2g_s^2}{t}\delta_{\lambda'\lambda}2Q\bar{u}_h(\kappa)\ \not{p}'\ v_{\bar{h}}(p)\left[\frac{\alpha}{\Delta_a}-\frac{(1-\alpha)}{\Delta_b}\right] \ . \tag{2.60}$$

Therefore we only have to find *one* trace: $\mathrm{Tr}\left[v_{\bar{h}}(p)\otimes\bar{u}_h(\kappa)p'\right]$ and we have already calculated it for all helicity configurations (see e.g (2.34) and (2.48)). The non-vanishing cases are

$$\mathrm{Tr}[v_{-(+)}(p)\otimes\bar{u}_{+(-)}(\kappa)\ \not{p}']=\mathcal{N}\left[\mathrm{Tr}(\gamma_5\ \not{p}\ \not{p}_0\ \not{\kappa}\ \not{p}')-\mathrm{Tr}(\not{p}\ \not{p}_0\ \not{\kappa}\ \not{p}')\right]=-s\sqrt{\alpha(1-\alpha)} \ . \tag{2.61}$$

Using (2.61) in (2.60), we find that

$$\mathcal{A}^L_{\pm\mp}=2g_s^2\frac{s}{t}\delta_{\lambda,\lambda'}\mathcal{C}\sqrt{\alpha(1-\alpha)}\Big[\Psi^L_{\pm\mp}(\boldsymbol{k},\alpha)-\Psi^L_{\pm\mp}(\boldsymbol{k}+\boldsymbol{r},\alpha)\Big] \tag{2.62}$$

with

$$\Psi^L_{\pm\mp}(\boldsymbol{k},\alpha)=-\frac{2ee_f\alpha(1-\alpha)Q}{\alpha(1-\alpha)Q^2+\boldsymbol{k}^2+m_f^2} \tag{2.63}$$

where we have defined and extracted the *longitudinal light-cone photon wavefunction* for the given quark-antiquark helicity configuration. $\Psi^L_{\pm\mp}(\boldsymbol{k}+\boldsymbol{r},\alpha)$ is given by the same expression with $\boldsymbol{k}\to\boldsymbol{k}+\boldsymbol{r}$. If $h=+(-)$ and $\bar{h}=+(-)$ (i.e the quark and antiquark have same helicities), we have found that this trace vanishes, see (2.48). Hence we can write

$$\mathcal{A}^L_{\pm\pm}=0 \quad ; \quad \Psi^L_{\pm\pm}(\boldsymbol{k},\alpha)=0 \ . \tag{2.64}$$

(2.63) are the non-vanishing longitudinal light-cone photon wavefunctions.

(2.63), (2.39), (2.41), (2.42), (2.43), (2.53) and (2.55) are the non-vanishing photon light-cone wavefunctions in momentum space. Let us collect them in a compact and obvious notation [59],

$$\Psi^{T(\gamma=+)}_{h,\bar{h}}(\boldsymbol{k},\alpha) = -\sqrt{2}ee_f[ke^{i\theta_k}(\alpha\delta_{h+,\bar{h}-} - (1-\alpha)\delta_{h-,\bar{h}+}) + m_f\delta_{h+,\bar{h}+}]\frac{1}{\boldsymbol{k}^2+\epsilon^2} \;, \tag{2.65}$$

$$\Psi^{T(\gamma=-)}_{h,\bar{h}}(\boldsymbol{k},\alpha) = -\sqrt{2}ee_f[ke^{-i\theta_k}((1-\alpha)\delta_{h+,\bar{h}-} - \alpha\delta_{h-,\bar{h}+}) + m_f\delta_{h-,\bar{h}-}]\frac{1}{\boldsymbol{k}^2+\epsilon^2} \;, \tag{2.66}$$

$$\Psi^{L}_{h,\bar{h}}(\boldsymbol{k},\alpha) = 2\alpha(1-\alpha)Qee_f\frac{1}{\boldsymbol{k}^2+\epsilon^2} \;, \tag{2.67}$$

with

$$\epsilon^2 = m_f^2 + \alpha(1-\alpha)Q^2 \;. \tag{2.68}$$

Let us pause to summarise what we have done so far. We have calculated the helicity amplitudes (in the high energy limit) for $\gamma^* q \to q\bar{q} + q$ scattering and *defined* the light-cone photon wavefunctions in terms of which we chose to express the amplitudes. However, the definition of the light-cone wavefunction is *not* arbitrary; it is precisely the probability amplitude for finding a $q\bar{q}$ pair (with the quark carrying a particular momentum fraction α and transverse momentum $\boldsymbol{k}$) in the photon. The wavefunction $\Psi(\boldsymbol{k},\alpha)$ does *not* depend on the high energy limit in which we choose to work. In other words, for the *sole* purpose of extracting the light-cone wavefunctions, taking the high energy limit for the full amplitude is *not* necessary but as we have shown, it does simplify considerably the calculation. This is not surprising, given the physical meaning of the photon light-cone wavefunction we stated earlier. Indeed, we would expect the wavefunction $\Psi(\boldsymbol{k},\alpha)$ to depend only on the $\gamma^* \to q\bar{q}$ vertex and not on the photon-proton centre-of-mass energy. We can clearly see this in (2.65) and (2.67). Of course, the expressions we have calculated for the photon wavefunctions are correct to leading order in $\alpha_{e.m.}$.[7] Let us next explore the physical meaning of these light-cone wavefunctions.

2.2.2 Light-cone quantisation

The physical interpretation of the light-cone wavefunction becomes clear within the framework of light-cone perturbation theory. Let us disgress a little to introduce the

[7]Clearly, we can add gluon emission. Recent progress concerning these α_s corrections can be found in [52].

basic features of this formalism (see e.g [56, 57] for a pedagogical introduction and [58] for a formal presentation). Quantisation is carried out at equal light-cone time x^+, where

$$x^{\pm} = \frac{1}{\sqrt{2}}(x^0 \pm x^3) \quad ; \quad x^{\mu} = (x^+, x^-, \boldsymbol{x}) \,. \tag{2.69}$$

Similarly, the 4-momentum P^{μ} is written as $P^{\mu} = (P^+, P^-, \boldsymbol{P})$ where P^- is conjugate to x^+ and plays the role of light-cone energy, while P^+ is the longitudinal momentum and the 3-momentum $\vec{P}$ is given by $(P^+, \boldsymbol{P})$. The dot product between any two 4 vectors a and b is

$$a.b = (a^+ b^- + a^- b^+) - \boldsymbol{a}.\boldsymbol{b} \,. \tag{2.70}$$

Therefore for an on mass-shell particle of mass m, we have the dispersion relation,

$$P^- = \frac{\boldsymbol{P}^2 + m^2}{P^+} \,. \tag{2.71}$$

Immediately, we can make a simple observation: $P^+ > 0$, which follows from (2.71) since the light-cone energy must be positive. This has an important consequence: The only state with zero longitudinal momentum is that with no particles, i.e the vacuum state. In more technical terms, the vacuum state does not mix with other Fock states; the light-cone vacuum is an exact eigenstate of the light-cone hamiltonian.[8] On the other hand, in equal-time quantisation, this is not the case: the 3 momentum $\vec{k} = (k^1, k^2, k^3)$ can have positive as well as negative values so that zero-momentum Fock states can contain particles. This is a major advantage of the light-cone formalism compared to the equal-time formalism. Consequently, in the light-cone formalism, it is legitimate to make a Fock state expansion of a QCD bound state, $|\varphi\rangle$ onto a quark-gluon basis: $|q\bar{q}\rangle$, $|q\bar{q}g\rangle$ and higher Fock states .

Suppose the light-cone momentum carried by the ith parton (quark or gluon) in a bound state, is k^+. Then the longitudinal momentum fraction z_i is defined as

$$z_i = \frac{k^+}{P^+} \,. \tag{2.72}$$

z_i is a boost invariant quantity [57]. We further need to specify $\boldsymbol{k}$ for each parton and k^- is fixed via the dispersion relation (2.71). The amplitude of fluctuation into each Fock state is given by the *light-cone wavefunction* $\Psi_{n/\varphi}(z_i, \boldsymbol{k}_i, h_i)$.

[8]The rigorous argument is more subtle, see e.g [60].

$$|\varphi : P\rangle = \int \overline{\prod}_i \frac{dz_i d^2\boldsymbol{k}_i}{\sqrt{z_i}16\pi^3} |n : z_i P^+, \boldsymbol{k}_i, h_i\rangle \Psi_{n/\varphi}(z_i, \boldsymbol{k}_i, h_i) \ . \tag{2.73}$$

where

$$\overline{\prod_i} = \prod_i \delta\left(\sum_i z_i = 1\right) 16\pi^3 \delta^2 \left(\sum_i \boldsymbol{k}_i\right) \tag{2.74}$$

The above delta functions express conservation of total momentum. In practice we truncate the expansion (2.73), retaining only the lowest valence Fock state, in accordance with the constituent quark model. For a meson, this would be the $|q\bar{q}\rangle$ state. Denoting the longitudinal momentum fraction of the quark by z and its transverse momentum by $\boldsymbol{k}$, we find

$$|\varphi : P\rangle = \int \frac{dz d^2\boldsymbol{k}}{16\pi^3\sqrt{z(1-z)}} |q\bar{q} : zP^+, \boldsymbol{k}, \bar{h}, h\rangle \Psi_{q\bar{q}/\varphi}(z, \boldsymbol{k}, \bar{h}, h), \tag{2.75}$$

where we have integrated over the longitudinal momentum fraction and the transverse momentum of the antiquark using the delta functions. In other words, the longitudinal momentum fraction and the transverse momentum of the antiquark are both fixed by that of the quark. On the other hand, the helicities of the quark and antiquark ($\bar{h}$ and h) are independent of each other and are explicit arguments of the light-cone wavefunction. The light-cone wavefunction satisfies the following normalisation condition[9][60, 57]:

$$\sum_{\bar{h},h} \int_0^1 dz \int \frac{d^2\boldsymbol{k}}{16\pi^3} \mid \Psi_{q\bar{q}/\varphi}(z, \boldsymbol{k}, \bar{h}, h) \mid^2 = 1 \ . \tag{2.76}$$

The bound state $|\varphi\rangle$ is an eigenstate of the light-cone Hamiltonian, H_{LC} :

$$H_{LC}|\varphi\rangle = M_\varphi^2|\varphi\rangle \ . \tag{2.77}$$

where the full light-cone Hamiltonian is $H_{LC} = H_0 + H_I$. H_I is the interacting part of the light-cone Hamiltonian while H_0 is the free Hamiltonian which satisfies

$$H_0|\phi\rangle = M_0^2|\phi\rangle. \tag{2.78}$$

[9]Of course (2.76) *imposes* a constituent picture of a meson consisting only of a quark and an antiquark. Relaxing this condition, one would replace the $=$ sign in (2.76) by a $\leq$ sign.

with M_0^2 being the invariant mass of the *non-interacting* $q\bar{q}$ pair. Adding the 4-momenta of the quark and antiquark, then squaring gives

$$M_0^2 = \frac{\boldsymbol{k}^2 + m_f^2}{z(1-z)} \; . \tag{2.79}$$

Rearranging (2.77) and projecting out the light-cone wavefunction, we have

$$\Psi_{q\bar{q}/\varphi} = \frac{\langle q\bar{q}|H_I|\varphi\rangle}{\xi} \; , \tag{2.80}$$

with

$$\xi = M_\varphi^2 - M_0^2 \; . \tag{2.81}$$

ξ is a measure of the (light-cone) *off-shellness* of the bound state. The overlap of a Fock state with the bound state (i.e the light-cone wavefunction) vanishes as $\xi \to \infty$. Since this happens when either $\boldsymbol{k}$ is large or z is small, we have the following boundary conditions on a light-cone wavefunction :

$$\Psi(z, \boldsymbol{k}, \bar{h}, h) \to 0 \quad \text{for} \quad \boldsymbol{k} \to \infty, \quad z \to 0 \text{ or } 1 \; . \tag{2.82}$$

To completely specify the light-cone wavefunction, we need to calculate the matrix element in the numerator of (2.80). For QCD bound states, this is a highly non-trivial task since the interaction light-cone Hamiltonian is not even known [59]. However, the photon light-cone wavefunction can be calculated within perturbation theory. Before doing that let us first make the connection between light-cone coordinates and the Sudakov decomposition we have been using in Section 2.1. In terms of light-cone coordinates, the 4-momentum of the photon is

$$q^\mu = (q^+, q^-, \mathbf{0}) \quad ; \quad q^- = \frac{-Q^2}{q^+} \; . \tag{2.83}$$

Using (2.2), (2.4) and (2.83), we find that

$$\alpha = \frac{k^+}{q^+} \; . \tag{2.84}$$

Therefore the Sudakov variable α is the fraction of light-cone longitudinal momentum of the photon carried by the quark. *Following the common trend, we shall call this variable z hereafter.*

The photon light-cone wavefunction $\Psi_\gamma(z, \boldsymbol{k})$ is defined via

$$|\gamma_{\text{physical}}\rangle = \sqrt{Z_3}|\gamma_{\text{bare}}\rangle + \int \frac{d^2\boldsymbol{k}}{16\pi^3} dz \Psi_{q\bar{q}/\gamma}(z, \boldsymbol{k})|q\bar{q}\rangle + \dots \ . \tag{2.85}$$

Here, Z_3 is the photon wavefunction renormalisation constant which is ultraviolet divergent for transverse photons [3, 54]. The photon light-cone wavefunction for fluctuating into a $q\bar{q}$ pair is given by (2.80), with the interaction Hamiltonian,

$$H_I = ee_f q^+ \int d^3x \bar{\Psi}(x) A.\gamma \Psi(x) \tag{2.86}$$

where A^μ, $\Psi(x)$ and $\bar{\Psi}(x)$ are the photon and quark fields containing the creation and annihilation operators. For a virtual photon, the off-shellness parameter ξ is given by

$$\xi = -\left(\frac{\boldsymbol{k}^2 + m_f^2}{z(1-z)} + Q^2\right) \ . \tag{2.87}$$

Using (2.80),(2.86) and (2.87), we can write [60]

$$\Psi^{T,L}_{h,\bar{h}} = -ee_f\sqrt{z(1-z)}\frac{\overline{u}_h(\boldsymbol{k}, z)\gamma.\varepsilon^{T,L} v_{\bar{h}}(-\boldsymbol{k}, 1-z)}{z(1-z)Q^2 + \boldsymbol{k}^2 + m_f^2} \ . \tag{2.88}$$

Choosing the longitudinal and transverse photon polarisation vectors as

$$\varepsilon^L = \left(\frac{q^+}{Q}, \frac{Q}{2q^+}, \mathbf{0}\right) \quad ; \quad \varepsilon^T = \frac{1}{\sqrt{2}}(0, 0, 1, \pm i) \tag{2.89}$$

and the matrix elements given in [58], we should recover the expressions (2.65), (2.66) and (2.67) we have derived earlier within covariant perturbation theory. Let us sketch the derivation for longitudinal photon light-cone wavefunction. Using ε^L and the light-cone matrix elements [58, 59]

$$\bar{u}\gamma^+ v = 2\sqrt{z(1-z)}q^+\delta_{\bar{h},-h} \ , \tag{2.90}$$

and

$$\bar{u}\gamma^- v = -\frac{\boldsymbol{k}^2 + m_f^2}{\sqrt{z(1-z)}q^+}\delta_{\bar{h},-h} \ , \tag{2.91}$$

we arrive at

$$\Psi^L_{h,\bar{h}}(\boldsymbol{k}, z; Q) = -\delta_{h,-\bar{h}} ee_f \left(\frac{z(1-z)2Q}{\boldsymbol{k}^2 + m_f^2 + z(1-z)Q^2} - \frac{1}{Q}\right) \ . \tag{2.92}$$

which is exactly the same as (2.67) except for the additional term in $1/Q$ in (2.92). However, when we take the Fourier transform to impact parameter space this term gives a delta function, $\delta^2(\boldsymbol{d}_\perp)$ which forces the dipole size to vanish. Such a dipole has no effective colour charge and leads to a vanishing cross-section [59]. Therefore, we can neglect this extra term.[10] We also notice that imposing gauge invariance takes this term away. Replacing the polarisation vector ϵ^μ by q^μ, the gauge-invariant light-cone wavefunction (or amplitude) must vanish

$$q^\mu \bar{u}_h \gamma_\mu v_{\bar{h}} = q^+ \bar{u}_h \gamma^- v_{\bar{h}} + q^- \bar{u}_h \gamma^+ v_h = 0 \tag{2.93}$$

so that

$$\bar{u}_h \gamma^- v_{\bar{h}} = \frac{Q^2}{q^{+2}} \bar{u}_h \gamma^+ v_h \ . \tag{2.94}$$

Therefore,

$$\bar{u}_h \gamma . \epsilon v_{\bar{h}} = \frac{Q}{q^+} \bar{u}_h \gamma^+ v_h \ . \tag{2.95}$$

Using the light-cone matrix element (2.90), we find that

$$\Psi^L_{h,\bar{h}}(\boldsymbol{k}, z; Q) = -\delta_{h,-\bar{h}} \frac{e e_f z(1-z) 2Q}{\boldsymbol{k}^2 + m_f^2 + z(1-z)Q^2} \ . \tag{2.96}$$

which is, as we expected, exactly the same as (2.92) without the term in $1/Q$. Recall that we also imposed gauge invariance when we calculated the longitudinal photon wavefunction in Section 2.2.1. This is precisely why the extra term did not appear in that earlier derivation.

Since we are dealing here with a virtual photon which is not a real composite particle, it is not surprising that the photon light-cone wavefunction differs from a hadronic light-cone wavefunction. First, the transverse photon light-cone wavefunction does not satisfy the boundary condition (2.82). Second, the normalisation condition for the transverse photon light-cone wavefunction also differs from (2.76) since Z_3 is ultraviolet divergent [3]. The usual normalisation condition for the transverse photon wavefunction is [3]

$$\sum_{h,\bar{h}} \int \frac{d^2\boldsymbol{k}}{4\pi^2} dz |\Psi_{h,\bar{h}}(\boldsymbol{k}, z; Q^2)|^2 = c^2 \tag{2.97}$$

[10] Nevertheless, we find it important to note the appearance of this "extra" term to be able to construct the meson light-cone wavefunction in exact analogy with the photon light-cone wavefunction. See Chapter 4.

with $c^2 = 1 - Z_3 \approx \frac{\alpha_{e.m}}{\pi} \sum_f e_f^2 \ln(\Lambda^2/Q^2)$.[11] In addition, we note the extra term in $1/Q$ reflects this point-like nature of the photon since when Fourier-transformed to $d_\perp$-space, it leads to a delta function, $\delta^2(\boldsymbol{d}_\perp)$ which forces the size of the dipole to be zero. Despite these remarks, in the light-cone formalism, given the wavefunction, there is little distinction between composite real and virtual particles [60]. The concept of a light-cone photon wavefunction is both legitimate and useful.

2.2.3 Photon light-cone photon wavefunctions in impact parameter space

Let us now find the light-cone photon wavefunctions in impact parameter space. The Fourier conjugate to the transverse momentum $\boldsymbol{k}$ is the transverse separation of the quark-antiquark pair, called the dipole size $\boldsymbol{d}_\perp$. The Fourier transform of a momentum space light-cone wavefunction is then given by

$$\Psi(\boldsymbol{d}_\perp, z) = \int \frac{d^2\boldsymbol{k}}{(2\pi)^2} e^{i\boldsymbol{k}.\boldsymbol{d}_\perp} \Psi(\boldsymbol{k}, z) \; . \tag{2.98}$$

First notice that for an arbitrary function $f(\boldsymbol{k})$, it is easy to show that

$$\int \frac{d^2\boldsymbol{k}}{(2\pi)^2} e^{i\boldsymbol{k}.\boldsymbol{d}_\perp} k e^{\pm\theta_k} f(\boldsymbol{k}) = -i(\partial_x \pm i\partial_y) f(\boldsymbol{d}_\perp) \; . \tag{2.99}$$

If in addition, the function $f(\boldsymbol{k})$ (and hence $f(\boldsymbol{d}_\perp)$) does not have any angular dependence, transformation to polar coordinates on the right-hand side of (2.99) simply gives

$$\int \frac{d^2\boldsymbol{k}}{(2\pi)^2} e^{i\boldsymbol{k}.\boldsymbol{d}_\perp} k e^{\pm\theta_k} f(k) = -ie^{\pm i\theta_{d_\perp}} \partial_{d_\perp} f(d_\perp) \; . \tag{2.100}$$

In our case,

$$f(k, z) = \frac{1}{z(1-z)Q^2 + k^2 + m_f^2} \tag{2.101}$$

which indeed does not have any angular dependence so that we can use (2.100). The Fourier transform of (2.101) gives

$$\int \frac{d^2\boldsymbol{k}}{2\pi^2} e^{i\boldsymbol{k}.\boldsymbol{d}_\perp} \frac{1}{\boldsymbol{k}^2 + \epsilon^2} = \frac{K_0(\epsilon d_\perp)}{2\pi} \tag{2.102}$$

[11] Here Λ is the ultraviolet cut-off and we have summed over the three colours [3].

where we have first done the angular integration and then used [61]

$$\int_0^\infty dt \frac{t^{\nu+1} J_\nu(at)}{(t^2+z^2)^{\mu+1}} = \frac{a^\mu z^{\nu-\mu}}{2^\mu \Gamma(\mu+1)} K_{\nu-\mu}(az) \; . \tag{2.103}$$

K_0 is the modified Bessel function [61] and $\epsilon^2 = Q^2 z(1-z) + m_f^2$. Using (2.102) and (2.100), it is now straightforward to write down the light-cone photon wavefunctions in impact-parameter space,

$$\Psi^L_{h,\bar{h}}(d_\perp, z) = \sqrt{\frac{N_c}{4\pi}} \delta_{h,-\bar{h}} e e_f 2z(1-z) Q \frac{K_0(\epsilon d_\perp)}{2\pi} \; . \tag{2.104}$$

$$\begin{aligned}\Psi^{T(\gamma=+)}_{h,\bar{h}}(d_\perp, z) = \sqrt{\tfrac{N_c}{4\pi}} e e_f \sqrt{2} \big[i e^{\pm i\theta_{d_\perp}} (z\delta_{h+,\bar{h}-} - (1-z)\delta_{h-,\bar{h}+}) \partial_{d_\perp} \\ + m_f \delta_{h+,\bar{h}+} \big] \tfrac{K_0(\epsilon d_\perp)}{2\pi} \; .\end{aligned} \tag{2.105}$$

$$\begin{aligned}\Psi^{T(\gamma=-)}_{h,\bar{h}}(d_\perp, z) = \sqrt{\tfrac{N_c}{4\pi}} e e_f \sqrt{2} \big[i e^{\pm - i\theta_{d_\perp}} ((1-z)\delta_{h+,\bar{h}-} - z\delta_{h-,\bar{h}+}) \partial_{d_\perp} \\ + m_f \delta_{h-,\bar{h}-} \big] \tfrac{K_0(\epsilon d_\perp)}{2\pi} \; .\end{aligned} \tag{2.106}$$

We have multiplied each of the above wavefunctions by $\sqrt{N_c/4\pi}$ so that they are properly normalised according to (2.97). We can now find the modulus squared of the above wavefunctions, summed over all quark and antiquark helicities. It is fairly straightforward to show that[12]

$$\mid \Psi^L(z, d_\perp) \mid^2 = \frac{6}{\pi^2} \alpha_{e.m} \sum_{f=1}^{n_f} e_f^2 Q^2 z^2 (1-z)^2 K_0^2(\epsilon d_\perp) \tag{2.107}$$

and

$$\mid \Psi^T(z, d_\perp) \mid^2 = \frac{3}{2\pi^2} \alpha_{e.m} \sum_{f=1}^{n_f} e_f^2 \left[(z^2 + (1-z)^2) \epsilon^2 K_1^2(\epsilon d_\perp) + m_f^2 K_0^2(\epsilon d_\perp) \right] \; . \tag{2.108}$$

Integrating over the transverse size $d_\perp$ and longitudinal momentum fraction z gives the probability for finding a $q\bar{q}$ pair in the photon.

2.2.4 Properties of the photon light-cone wavefunctions

The modified Bessel functions $K_0(y)$ and $K_1(y)$ diverge as $1/y$ and $\ln(1/y)$ for the argument $y \ll 1$ and are exponentially suppressed for large y [61]. Let us investigate

[12]We shall show more details when calculating analogous quantities in the case of DVCS in Chapter 3.

Figure 2.2: Schematic representation of the fluctuation of photon into a $q\bar{q}$ pair. (a) : Equal share in longitudinal momentum, small dipole, (b) : z near its end-points, large dipole (also called the aligned jet configuration [3]).

some interesting limits. For a given Q^2, if $d_\perp$ is large, z is near its 'end-points' : $z \sim 0$ or 1. Large dipoles have an asymmetric sharing of the photon's longitudinal momentum. On the other hand, for small $d_\perp$, an equal share of the longitudinal momentum is favoured : $z \sim 1/2$. Now, the longitudinal photon wavefunction vanishes for $z \sim 0$ or 1 because of the $z(1-z)$ factor in the numerator (see (2.79)). This is not the case for the transverse photon wavefunction. Therefore, the end-points of z are not suppressed in the transverse photon wavefunction. Put another way, *the transversely polarised photon can produce large dipoles even at large* Q^2 (see also the discussion in [93]).

If Q^2 is large, small dipoles are favoured modulo the case when z is near its end-points in the transverse photon wavefunction. In this limit the wavefunctions become insensitive to the quark mass. On the other hand, for small Q^2, the wavefunctions become sensitive to the quark mass and at the same time favour large dipoles. Clearly, confinement effects become important in this region. At $Q^2 = 0$, the quark mass acts as an infrared regulator preventing the modified Bessel functions from diverging. In this way, we can decrease Q^2 down to the photoproduction limit, $Q^2 = 0$, although it is clear that non-perturbative effects become important and the photon wavefunction becomes model-dependent in this limit. We postpone a quantitative discussion of the modelling of the photon wavefunction in this region to Section 2.5, when we shall introduce different dipole models. For now, we illustrate these properties of the photon light-cone wavefunctions in Figure 2.3 and Figure 2.4 below.

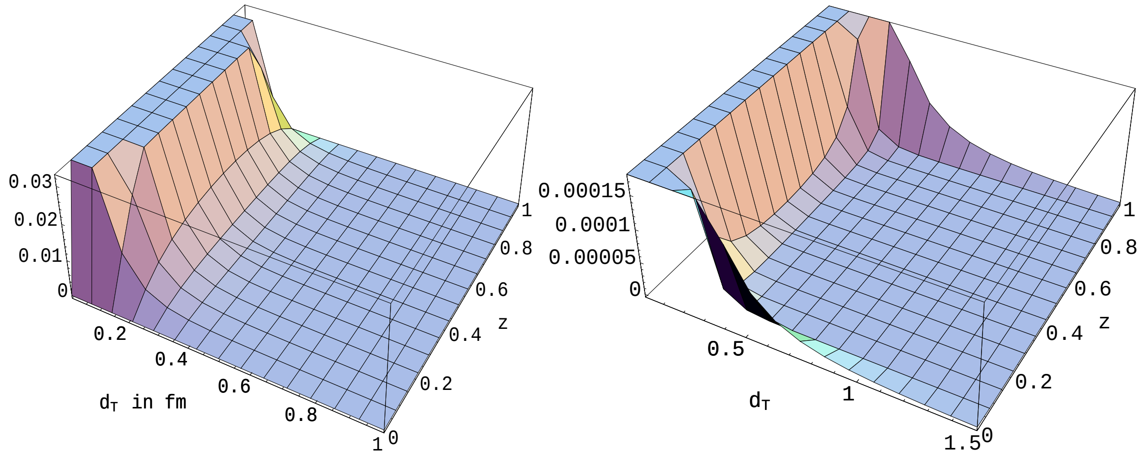

Figure 2.3: $|\Psi^L(z, d_\perp; Q^2)|^2$ (left) and $|\Psi^T(z, d_\perp; Q^2)|^2$ (right) as a function of $d_\perp$ (in fm) and z. We can see clearly that the end-points contributions are not suppressed in the transverse case. Consequently, the transverse photon selects large dipoles even for high Q^2. Here, $Q^2 = 20$ GeV^2. Note the different range on the $d_\perp$ (denoted by d_T here) axis. Both wavefunctions diverge at as $d_\perp \to 0$.

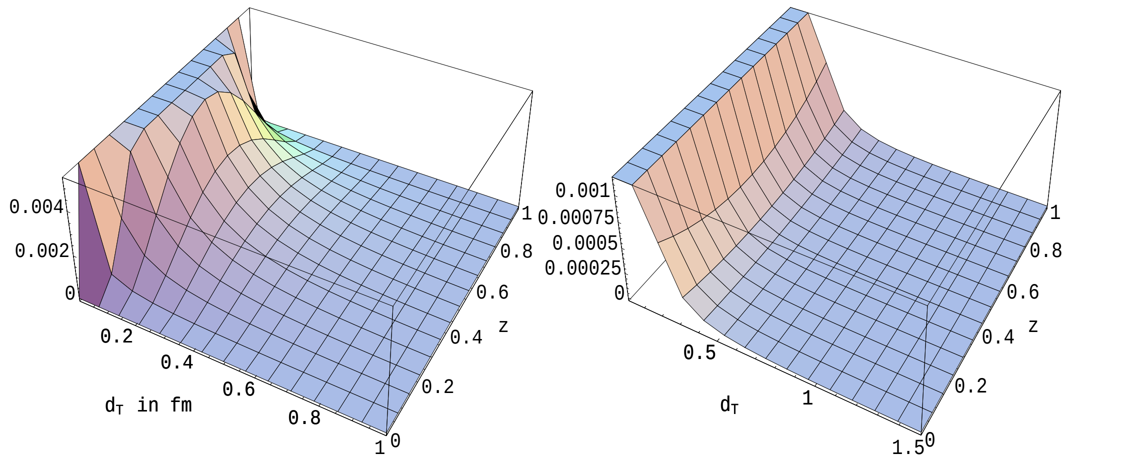

Figure 2.4: The effect of decreasing Q^2 from 20.0 GeV^2 (Compare with Figure 2.3 above) to 0.1 GeV^2. Larger dipoles are less suppressed in both the longitudinal and transverse photon wavefunctions.

2.3 Factorisation in impact parameter space

2.3.1 Elastic Compton scattering on a quark

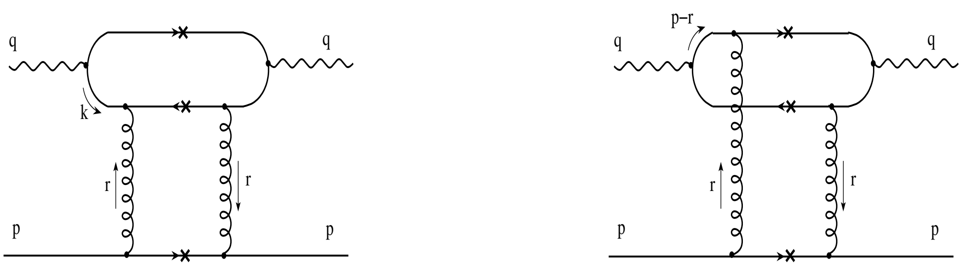

Figure 2.5: Two gluon exchange for the process $\gamma^* q \to \gamma^* q$. The 4-momenta are given in brackets and defined in the text. To ensure gauge invariance, there are two other diagrams which we need to take into account, in which the *right* gluon couples to the antiquark instead.

We progress to two gluons being exchanged in the t-channel and the quark-antiquark pair recombining into a virtual photon in the final state. This is the lowest order QCD process which can simulate Pomeron exchange, since the two gluons can be in a colour singlet. We follow the presentation given in [51], using the calculational technique developed in [3]. We shall restrict ourselves to the calculation of the *forward* ($t = 0$) amplitude. This is reasonable since we shall be concerned only with diffractive amplitudes which peaks in the forward direction. Following [3], we use the Cutkosky rule [4] which allows us to *cut* the Feynman diagram into two parts and integrate over the phase space of the three intermediate particles which we put on mass-shell denoted by crosses in Figure 2.5. This gives the imaginary part of the amplitude which is precisely what we are interested in since diffractive amplitudes are predominantly imaginary. The full amplitude is then given by

$$\mathcal{A}_{(2.5)}(s, t = 0) = \int d(P.S^3)\mathcal{A}_{(2.1)}(\boldsymbol{k}, \boldsymbol{d}_\perp, z)\mathcal{A}^\dagger_{(2.1)}(\boldsymbol{k}, \boldsymbol{d}_\perp, z) \tag{2.109}$$

with

$$d(P.S^3) = \frac{1}{128\pi^5}\int d^4p d^4\kappa d^4p'_l \delta(p^2-m^2)\delta(\kappa^2-m^2)\delta(p'^2_l)\delta^4(q+p_l-p-\kappa-p'_l)\ . \quad (2.110)$$

The integral over p'_l can be done to absorb the energy-momentum conserving delta function. We then *choose* to integrate over the quark momemtum k and the gluon momentum r. Using (2.2), (2.4) and (2.5), we arrive at

$$\begin{aligned} d(P.S^3) &= \frac{1}{512\pi^5 s}\int dz d\beta d^2\boldsymbol{k} d\alpha' dx_g d^2\boldsymbol{r} \\ &\quad \delta((1-z)(x+\beta)-(\frac{\boldsymbol{k}^2+m^2}{s})) \\ &\quad \delta(z(\beta+x_g)-\frac{\boldsymbol{\kappa}^2+m^2}{s})\delta(\alpha'(1-x_g)-\frac{\boldsymbol{r}^2}{s}) \end{aligned}$$

where we have included the Jacobian, $J = s/2$ due to the change to Sudakov variables and also extracted a factor $1/s$ from each delta function. Since the amplitudes depend only on $\boldsymbol{k}$ and $\boldsymbol{r}$, we can absorb all three delta functions by integrating out the Sudakov variables α', x_g and β. We are left with

$$\mathcal{A}_{(2.5)}(s,t=0) = \frac{1}{512\pi^5 z(1-z)s}\int dz d^2\boldsymbol{k}\frac{d^2\boldsymbol{r}}{\boldsymbol{r}^4}\mathcal{A}_{(2.1)}\mathcal{A}^\dagger_{(2.1)}\ . \quad (2.111)$$

We have already calculated the amplitudes $\mathcal{A}_{2.1}(\boldsymbol{k})$ and $\mathcal{A}_{2.1}(\boldsymbol{k}+\boldsymbol{r})$ in terms of the light-cone photon wavefunctions. For the following discussion , we can choose any particular configuration and suppress for convenience the helicity indices on the photon light-cone wavefunctions. Hence we have

$$\mathcal{A}_{(2.5)}(s,t=0) = \frac{sg_s^4\mathcal{C}'}{128\pi^5}\delta_{\lambda\lambda'}\int d^2\boldsymbol{k}\frac{d^2\boldsymbol{r}}{\boldsymbol{r}^4}dz\left[\Psi(\boldsymbol{k},z)-\Psi(\boldsymbol{k}+\boldsymbol{r},z)\right]\left[\Psi^*(\boldsymbol{k},z)-\Psi^*(\boldsymbol{k}+\boldsymbol{r},z)\right]\ . \quad (2.112)$$

Note that we have a different colour factor C' now. Let us write the photon wavefunctions in impact parameter space. Picking up an extra exponential due to the integration shift when taking the Fourier transform of $\Psi(\boldsymbol{k}+\boldsymbol{r})$, and we arrive at

$$\begin{aligned} \mathcal{A}_{(2.5)}(s,t=0) &= s\frac{g_s^4\mathcal{C}'}{32\pi^3}\int dz\frac{d^2\boldsymbol{r}}{\boldsymbol{r}^4}d^2\boldsymbol{d}_\perp\left[1-e^{-i\boldsymbol{r}.\boldsymbol{d}_\perp}\right]\left[1-e^{i\boldsymbol{r}.\boldsymbol{d}_\perp}\right] \\ &\quad \times\int\frac{d^2\boldsymbol{k}}{(2\pi)^2}e^{i\boldsymbol{k}.(\boldsymbol{d}'_\perp-\boldsymbol{d}_\perp)}\Psi(\boldsymbol{d}'_\perp,z)\Psi^*(\boldsymbol{d}_\perp,z)\ . \end{aligned} \quad (2.113)$$

Notice that the amplitude vanishes for $\boldsymbol{r}=0$, thereby regulating the infrared divergence when integrating over $\boldsymbol{r}$. This is in accordance with the general result that colour singlet amplitudes are infrared finite [3].[13] The integration over $\boldsymbol{k}$ is trivially

[13] This is the Kinoshita, Lee, Nauenberg theorem [62].

done and gives a delta function $\delta^2(\boldsymbol{d}_\perp - \boldsymbol{d}'_\perp)$ which can then be absorbed by integrating over $\boldsymbol{d}'_\perp$. We choose not to do it yet. Instead, let us get closer to an actual physical process by replacing the lower quark by a proton as shown in Figure 2.6.

2.3.2 Elastic Compton scattering on a proton

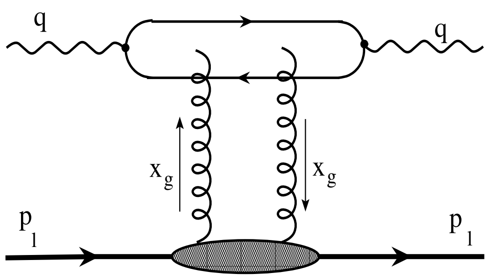

Figure 2.6: Elastic Compton scattering ($\gamma^* p \to \gamma^* p$) via two gluon exchange. The unintegrated gluon distribution is represented by the lower blob. The gluons can be attached to either the quark or the antiquark in the upper loop. The 4-momenta are defined in the text.

To describe the non-perturbative interaction of the gluons to the proton, we introduce the *unintegrated gluon distribution* $\mathcal{F}(x_g, \boldsymbol{r}^2)$. Making the replacement,

$$\frac{g_s^2 \mathcal{C}'}{8\pi^2} \delta_{\lambda\lambda'} \to \mathcal{F}(x_g, \boldsymbol{r}^2) \tag{2.114}$$

we find that the amplitude (2.113) becomes

$$\begin{aligned} \mathcal{A}_{(2.6)}(s, t=0) &= s \tfrac{g_s^2}{4\pi} \int dz \tfrac{d^2\boldsymbol{r}}{\boldsymbol{r}^4} d^2\boldsymbol{d}_\perp \mathcal{F}(x_g, \boldsymbol{r}^2) \left[1 - e^{-i\boldsymbol{r}.\boldsymbol{d}'_\perp}\right] \left[1 - e^{i\boldsymbol{r}.\boldsymbol{d}_\perp}\right] \\ &\qquad \times \int \tfrac{d^2\boldsymbol{k}}{(2\pi)^2} e^{i\boldsymbol{k}.(d'_\perp - d_\perp)} \Psi(d'_\perp, z) \Psi^*(\boldsymbol{d}_\perp, z) \end{aligned} \tag{2.115}$$

Here we are using the k_T factorisation scheme[14] [63] and going beyond leading $\ln Q^2$. $\mathcal{F}(x_g, \boldsymbol{r}^2)$ is the distribution function for finding a gluon with transverse momentum $\boldsymbol{r}^2$

[14] Compare to collinear factorisation in DIS for instance, where the transverse momentum of a parton is forced to be less than some scale.

and a fraction x_g of the proton's light-cone energy. By integrating over the transverse momentum $\boldsymbol{r}$, we get the ordinary gluon distribution

$$x_g g(x_g, Q^2) = \int \frac{d^2\boldsymbol{r}}{\boldsymbol{r}^2} \theta(Q^2 - \boldsymbol{r}^2) \mathcal{F}(x_g, \boldsymbol{r}^2) \ , \tag{2.116}$$

where the theta function provides an upper limit, Q^2, for the integration. If we define the *dipole cross-section* as

$$\hat{\sigma}(\boldsymbol{d}_\perp, x_g) \equiv \frac{4\pi\alpha_s}{N_c} \int \frac{d^2\boldsymbol{r}}{\boldsymbol{r}^4} \mathcal{F}(x_g, \boldsymbol{r}^2)[1 - e^{-i\boldsymbol{r}.\boldsymbol{d}_\perp}][1 - e^{i\boldsymbol{r}.\boldsymbol{d}'_\perp}] \ , \tag{2.117}$$

and use

$$\int \frac{d^2\boldsymbol{k}}{(2\pi)^2} e^{i\boldsymbol{k}.(\boldsymbol{d}'_\perp - \boldsymbol{d}_\perp)} = \delta^2(\boldsymbol{d}'_\perp - \boldsymbol{d}_\perp) \tag{2.118}$$

we arrive at

$$\mathcal{A}^{L,T}_{\bar{h},h(2.6)}(s, t = 0) = s\frac{N_c}{4\pi} \int d^2\boldsymbol{d}_\perp dz \hat{\sigma}(\boldsymbol{d}_\perp, x_g) \Psi^{L,T}_{\bar{h},h}(\boldsymbol{d}_\perp, z) \Psi^{L,T*}_{\bar{h},h}(\boldsymbol{d}_\perp, z) \tag{2.119}$$

where we have restored the helicity indices. Summing over $\bar{h}$ and h, we arrive at

$$\mathcal{A}^{L,T}_{(2.6)}(s, t = 0) = s \int d^2\boldsymbol{d}_\perp dz \hat{\sigma}(\boldsymbol{d}_\perp, x_g) \mid \Psi^{L,T}(\boldsymbol{d}_\perp, z) \mid^2 \ . \tag{2.120}$$

where $\Psi^{L,T}(\boldsymbol{d}_\perp, \alpha)$ is given by (2.107) or (2.108). We find that the dipole cross-section neatly factorises from the light-cone wavefunctions. Going a step further, we use the optical theorem (see (1.24)) to get the total inclusive DIS $\gamma^* p \to X$ cross-section,

$$\sigma^{L,T}(\gamma^* p \to X) = \int d^2\boldsymbol{d}_\perp dz \hat{\sigma}(\boldsymbol{d}_\perp, x_g) \mid \Psi^{L,T}(\boldsymbol{d}_\perp, z) \mid^2 \ . \tag{2.121}$$

Note that the above derivation is valid only if we assume that x_g does *not* depend on $\boldsymbol{k}$ so that we could take $\mathcal{F}(x_g, \boldsymbol{r}^2)$ out of the $\boldsymbol{k}$ integral so that the latter results in the delta function, $\delta^2(\boldsymbol{d}_\perp - \boldsymbol{d}'_\perp)$. This delta function expresses conservation of the transverse size of the quark-antiquark pair during the interaction. This assumption is justified only if in (2.7), we assume that $M_t^2 \sim Q^2$ so that $x_g \sim 2x$ [65]. *Otherwise if x_g is specified exactly, transverse $d_\perp$ is no longer conserved and the k_T factorisation approach is no more compatible with the colour dipole model* [64].

The pQCD dipole cross-section as given by (2.117) relates the dipole cross-section to the gluon density. Indeed, if we expand the exponential in (2.117) to second order in $d_\perp$ and do the angular integration, we find

$$\hat{\sigma}(x_g, d_\perp) = \frac{\pi^2 d_\perp^2}{3} \alpha_s x_g g(x_g, Q^2) \ . \tag{2.122}$$

where at leading $\ln(1/x)$, we can make the assumption $x_g \sim x$. We do not claim to have derived (2.122); it is merely a definition in our formulation (see (2.117)) and for a rigorous derivation we refer to [66]. At leading $\ln 1/x$ and$\ln Q^2$ accuracy, it is sufficient to sample the gluon density at $x_g = x$ and Q^2 [67]. Going beyond leading log, some *effective* scales $\bar{Q}^2$ and x_g must be chosen. However, we must point out that the colour dipole model is believed to be correct to leading $\ln(1/x)$ and going beyond that accuracy is only phenomenologically motivated. At the same time, the skewed or generalised gluon distribution must be used which depends on the kinematics on a particular process. We shall discuss the skewedness of the DVCS amplitude in Chapter 3.

Within pQCD, we have defined the dipole cross-section and showed how the amplitude for elastic Compton scattering factorises into the dipole cross-section and the light-cone photon wavefunctions for the initial and final state. However, it turns out that (2.120) is a *perfectly general formula*, valid beyond perturbation theory as we shall demonstrate in Section 2.4. Before doing that, let us discuss the idea of gluon saturation.

2.3.3 Gluon saturation

Recall in Section 1.5.1, Chapter 1, we have seen that the gluon density rises steeply at small x. Gluon saturation is the idea that the number of gluons cannot become arbitrarily large in the proton [70]. As the energy s increases (at fixed Q^2) we enter a regime where the interaction between the gluons have to be taken into account. In the dipole framework, the phenomenon of gluon saturation translates into a breakdown in the monotonic increase of the dipole cross-section with dipole size. Put another way, if the cross-section of small dipoles start to exceed that of large dipoles at sufficiently high s (low x), we see the onset of gluon saturation. This is distinct from “saturation” of the dipole cross-section with dipole size $d_\perp$ (i.e the dipole cross-section becomes slowly varying with $d_\perp$ at large $d_\perp$ or low Q^2) which is necessary to acheive the $F_2 \propto Q^2$ behaviour in the photoproduction limit [29]. To avoid possible confusion, let us stress that when we speak of saturation, we mean saturation with the energy s. We shall see in Section 2.6 how saturation effects are implemented in one dipole model.

2.4 General formulation of the colour dipole model

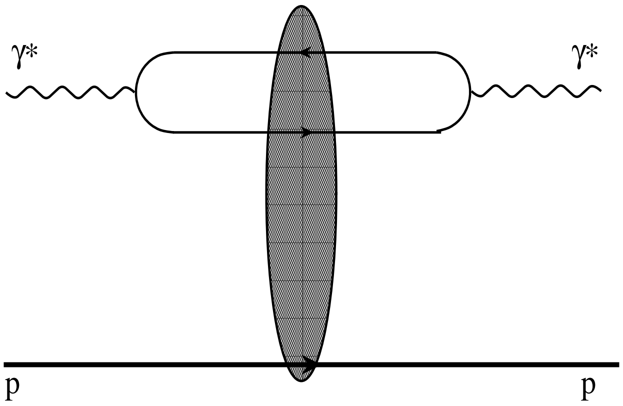

Figure 2.7: Elastic Compton Scattering in the colour dipole model

Let us now analyse the photon-proton interaction in the rest frame of the proton. At small x, the time scale of fluctuation of the photon into the dipole is much greater than the time scale of the dipole-proton interaction. It is convenient to use the light-cone formalism to show this [3]. In the proton's rest frame, the 4-momentum of the proton is

$$P^\mu = (M_p, M_p, \mathbf{0}) \tag{2.123}$$

and that of the quark (or antiquark, with the substitution $z \to (1-z)$ and $\boldsymbol{k} \to -\boldsymbol{k}$) is

$$q^\mu = \left(zP^+, \frac{m_f^2 + \boldsymbol{k}^2}{zP^+} \right) \ . \tag{2.124}$$

The energy imbalance $\Delta E = q^0 - k_q^0 - k_{\bar{q}}^0$ is then

$$\Delta E \approx \left(Q^2 + \frac{\boldsymbol{k}^2 + m_f^2}{z(1-z)} \right) \frac{M_p x}{2Q^2} \ , \tag{2.125}$$

where we have made use of the conservation of the '+' component at the $\gamma^* q\bar{q}$ vertex. At large Q^2, it follows from the uncertainty principle that longitudinal distance over which the $q\bar{q}$ pair propagates is $\sim \frac{1}{M_p x}$ which can be huge compared to the radius of the proton. This implies a factorisation of the scattering amplitude in terms of light-cone wavefunctions and a dipole cross-section.

In the diffractive regime (high energy), the quark-antiquark pair is moving fast and the small momentum transfer due to its interaction with the proton is too small to change the transverse size $d_\perp$ of the quark-antiquark pair and the fraction of (light-cone) longitudinal momentum z $(1-z)$ carried by the quark (antiquark). In other words, $d_\perp$ and z are conserved and the quantum state $|z, d_\perp\rangle$ is an eigenstate of the diffraction operator $\hat{T}$ [26]:

$$\hat{T}|z, \boldsymbol{d}_\perp\rangle = i\tau(b, s; z, d_\perp)|z, d_\perp\rangle \tag{2.126}$$

where τ is the probability that a $q\bar{q}$ pair with definite $d_\perp$ and z scatters off the proton which depends also on the impact parameter b of the pair with respect to the proton. b is the Fourier conjugate of the transverse momentum transfer $\boldsymbol{q}_\perp$ ($\boldsymbol{q}_\perp = 0$ for forward scattering). Therefore we can write the forward amplitude for virtual Compton scattering ($\gamma^* p \to \gamma^* p$) as

$$\mathcal{A}(s, t=0) = \int d^2\boldsymbol{b}\mathcal{A}(\boldsymbol{b}, s) \quad ; \quad \mathcal{A}(\boldsymbol{b}, s) = \langle\gamma^*|\hat{T}|\gamma\rangle \ . \tag{2.127}$$

The hadronic fluctuation of the virtual photon is given by

$$|\gamma_{\text{hadronic}}\rangle = \int dz d^2\boldsymbol{d}_\perp \Psi(z, d_\perp; Q^2)|z, \boldsymbol{d}_\perp\rangle \tag{2.128}$$

where $\Psi(z, d_\perp, Q^2)$ is the light-cone photon wave function. Hence, the elastic amplitude $\mathcal{A}(\boldsymbol{b}, s)$ is given by

$$\mathcal{A}(\boldsymbol{b}, s) = i\int s dz d^2\boldsymbol{d}_\perp \Psi^*(z, d_\perp; Q^2)\Psi(z, d_\perp; Q^2)\int d^2\boldsymbol{b}\frac{\tau(s, \boldsymbol{b}; z, \boldsymbol{d}_\perp)}{s} \ . \tag{2.129}$$

The second integral defines the dipole cross-section $\hat{\sigma}$:

$$\hat{\sigma}(z, \boldsymbol{d}_\perp, s) \equiv \int d^2\boldsymbol{b}\frac{\tau(s, \boldsymbol{b}; z, \boldsymbol{d}_\perp)}{s} \ . \tag{2.130}$$

Hence we have reached the same expression for the forward amplitude for virtual Compton Scattering in the previous section (see (2.120)). In this way, we have verified that the factorisation of the elastic Compton scattering forward amplitude is valid beyond perturbation theory since large $d_\perp$ does not affect the validity of the factorisation in (2.129). However, the light-cone photon wavefunctions we calculated in Section 2.1 within pQCD can reliably be used only for small $d_\perp$ (Recall our discussion on the properties of the photon wavefunctions in Section 2.1.4). In the dipole model, we integrate over *all* dipole sizes $d_\perp$ and we definitely have a contribution from large sized dipoles. The extent of these non-perturbative effects depends on the physical process we are calculating.

Let us now show how the dipole model can be used to analyse various physical processes. First consider the total inclusive cross-section in Deep Inelastic Scattering (DIS). Using the optical theorem, we can immediately write

$$\sigma_{T,L}^{\gamma^* p \to X} = \sum_{h,\bar{h}} \int dz d^2\boldsymbol{d}_\perp \mid \Psi_{T,L}(z, d_\perp) \mid^2 \hat{\sigma} \tag{2.131}$$

where the sum is over all possible quark and antiquark helicities. For Deeply Virtual Compton Scattering, we have a real photon in the final state.

$$\gamma^* p \to \gamma p$$

and hence we evaluate the light-cone wave function of the final photon at $Q^2 = 0$. Though the light-cone photon wavefunction is well-defined in this limit, it is subject to the uncertainties we discuss in Section 2.2.4. The imaginary part of the amplitude is then given as

$$\mathcal{A}^{\gamma^* p \to \gamma p}(s, t = 0) = s \sum_{h,\bar{h}} \int dz d^2\boldsymbol{d}_\perp \Psi_T(z, d_\perp, Q^2) \Psi_T(z, d_\perp, 0) \hat{\sigma} \tag{2.132}$$

where the final state real photon forces the process to be purely transverse. Similarly, for vector meson production,

$$\gamma^* p \to V p$$

we simply need to replace the final state wavefunction with the *meson light-cone* *wavefunction*, $\Psi^v(z, d_\perp)$

$$\mathcal{A}^{\gamma^* p \to \gamma p}(s, t=0) = s \sum_{h,\bar{h}} \int dz d^2\boldsymbol{d}_\perp \Psi^\gamma(z, d_\perp, Q^2) \Psi^v(z, d_\perp) \hat{\sigma} \; . \tag{2.133}$$

We shall devote Chapter 4 to a detailed analysis of this process. For diffractive DIS, the forward differential cross-section is given by [3],

$$\frac{d\sigma^D_{T,L}}{dt}|_{t=0} = \int_0^1 dz \int d^2\boldsymbol{d}_\perp |\Psi^\gamma_{T,L}(z, d_\perp; Q^2)|^2 \frac{\hat{\sigma}^2}{16\pi} \; , \tag{2.134}$$

where the *square* of the dipole cross-section enters the amplitude.

For us to go further and do numerical calculations, we need to parameterize the dipole cross-section. We have just seen that in the general formulation, $\hat{\sigma}$ is an object which encodes the perturbative and non-perturbative interaction of the $q\bar{q}$ pair with the proton. In principle, it depends on the fraction of the photon's light-cone longitudinal momentum carried by the quark, z, the transverse size of the dipole $\boldsymbol{d}_\perp$ and the energy s. A non-perturbative calculation reveals a weak z dependence [59] and we shall completely neglect it in our work. pQCD tells us that it is related to the gluon density of the proton and (modulo scaling violations) it vanishes as $d_\perp^2$ as $d_\perp \to 0$. For large $d_\perp$, perturbation theory is useless, and we resort to Regge phenomenology to construct the dipole cross-section. Several authors have modelled the dipole cross-section [71, 75, 76, 73, 79]; for a concise summary, see e.g [80]. We shall discuss the Donnachie-Dosch dipole model [93] as applied to DVCS in Chapter 3. A popular and successful model is the Golec-Biernat-Wüsthoff [73] (GW) dipole model. The GW dipole cross-section has the attractively simple parametric form :

$$\hat{\sigma} = \sigma_0 \left(1 - \exp\left[\frac{-d_\perp^2 Q_0^2}{4(x_{\mathrm{mod}}/x_0)^\lambda} \right] \right) \; . \tag{2.135}$$

Here x_{mod} is a modified Bjorken variable[15]

$$x_{\mathrm{mod}} = x \left(1 + \frac{4m_f^2}{Q^2} \right) \; , \tag{2.136}$$

where m_f is the quark mass. The 3 free parameters x_0, σ_0 and λ were successfully fitted to F_2 data. Note that saturation in the energy variable s is explicit in (2.135), reflecting

[15]This modification allows to study the photoproduction limit [74].

the idea of parton saturation at high s (See Section 2.3.3). A recent refinement of the model takes into account DGLAP evolution at large Q^2 [74].

We shall now focus on two other models: The Forshaw-Kerley-Shaw (FKS) and McDermott-Frankfurt-Guzey-Strikman (MFGS) models.

2.5 Forshaw-Kerley-Shaw model

Forshaw et al. [71] proposed the following parametric form for the dipole cross-section[16]

$$\hat{\sigma}(W^2, d_\perp) = \hat{\sigma}_{\text{soft}}(W^2, d_\perp) + \hat{\sigma}_{\text{hard}}(W^2, d_\perp)\,, \tag{2.137}$$

each with a Regge type energy dependence on the dimensionless energy variable $d_\perp^2 W^2$:

$$\hat{\sigma}_{\text{soft}}(W^2, d_\perp) = a_0^S \left(1 - \frac{1}{1 + a_4^S d_\perp^4}\right) (d_\perp^2 W^2)^{\lambda_S} \tag{2.138}$$

$$\hat{\sigma}_{\text{hard}}(W^2, d_\perp) = (a_2^H d_\perp^2 + a_6^H d_\perp^6)\ \exp(-\nu_H d_\perp)(d_\perp^2 W^2)^{\lambda_H} \tag{2.139}$$

The free parameters of the model are determined by a fit to $F_2(x, Q^2)$ data. For small

λ_S	0.06 ± 0.01	λ_H	0.44 ± 0.01
a_0^S	30.0 (fixed)	a_2^H	0.072 ± 0.010
a_4^S	0.027 ± 0.007	a_6^H	1.89 ± 0.03
		ν_H	3.27 ± 0.01
B	7.05 ± 0.08	c^2	0.20 (fixed)
R	6.84 ± 0.02		
m_q^2	0.08 (fixed)	m_c^2	1.4 (fixed)

Table 2.1: Parameters for the FKS model specified by (2.137) and (2.143), in appropriate GeV based units throughout.

[16]In [71] a more complicated parametric form was used, but this simpler parametric form gives very similar results.

dipoles the hard term dominates yielding a behaviour

$$\hat{\sigma} \to a_2^H d_\perp^2 \; (d_\perp^2 W^2)^{\lambda_H} \qquad d_\perp \to 0 \tag{2.140}$$

in accordance with the pQCD prediction (see Section 2.1).[17] For large dipoles the soft term dominates with a hadron-like behaviour

$$\hat{\sigma} \approx a_0^S \; (d_\perp^2 W^2)^{\lambda_S} \qquad d_\perp \approx 1 \text{ fm}. \tag{2.141}$$

FKS chose $m_f^2 = 0.08$ GeV^2 corresponding roughly to a constituent mass for the light quark case and modified the light-cone photon wavefunction by multiplying by an adjustable Gaussian enhancement factor:

$$\psi_{T,L}(z, d_\perp, Q^2) \to \psi_{T,L}^{\text{pert.}}(z, d_\perp, Q^2)\sqrt{f(d_\perp)} \tag{2.142}$$

where

$$f(d_\perp) = \frac{1 + B\exp(-c^2(d_\perp - R)^2)}{1 + B\exp(-c^2 R^2)}. \tag{2.143}$$

This form enables the width and height of the enhancement to be controlled independently while keeping a factor of close to unity at small $d_\perp$. Let us investigate this effect for the DIS inclusive cross-section. Integrating out the angular and z dependence in (2.131) and adding together the longitudinal and transverse cross-sections, we have

$$\begin{aligned} \sigma^{\gamma^* p \to X} &= \int \mathrm{d}z \; \mathrm{d}^2 d_\perp \; (|\psi_T(z, d_\perp)|^2 + |\psi_L(z, d_\perp)|^2)\hat{\sigma}(s, d_\perp) \\ &= \frac{12}{\pi}\alpha_{e.m.} \int \mathrm{d}d_\perp H(d_\perp)\hat{\sigma}(s, d_\perp) \; . \end{aligned} \tag{2.144}$$

The resulting behaviour of $H(d_\perp)$ is shown in Figure 2.8: as can be seen, the enhancement is important for very low Q^2, but decreases rapidly as Q^2 increases. Other authors do not in general include an explicit enhancement factor, but achieve a similar effect, at least for $Q^2 > 1$ GeV^2, by varying the quark mass. Choosing a smaller quark mass increases the wavefunction at all large $d_\perp$, as illustrated in Figure 2.9. Golec-Biernat and Wusthoff [73], for example, used $m_q^2 = 0.02$ GeV^2, comparable with the pion mass squared. The FKS dipole model was subsequently found [72] to give good predictions for Diffractive DIS (see Section 1.5.2).

[17] Note that the dependence on $d_\perp$ is *not* quadratic.

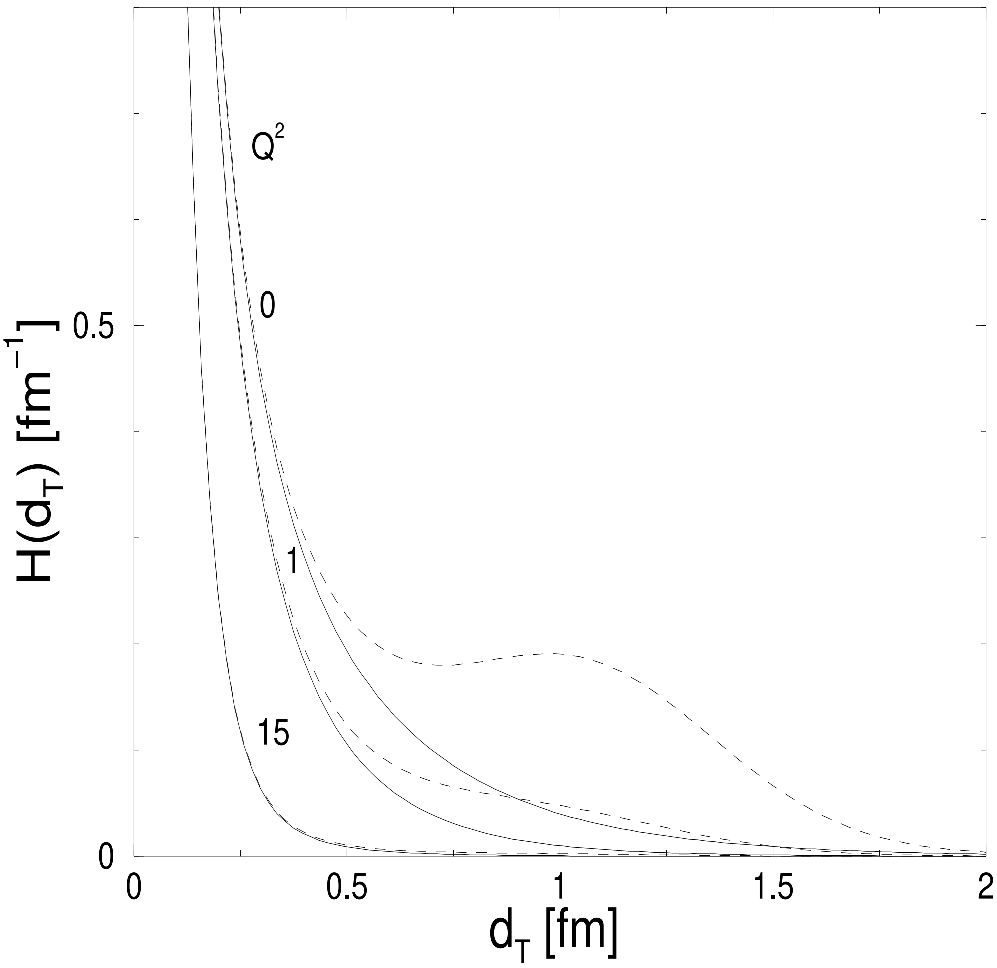

Figure 2.8: The weight function $H(d_\perp)$ for different Q^2 corresponding to the photon wavefunction obtained by FKS [71] with $m_q^2 = 0.08$ GeV^2. The peak at low Q^2 represents the modification to the perturbative photon wave function at large $d_\perp$.

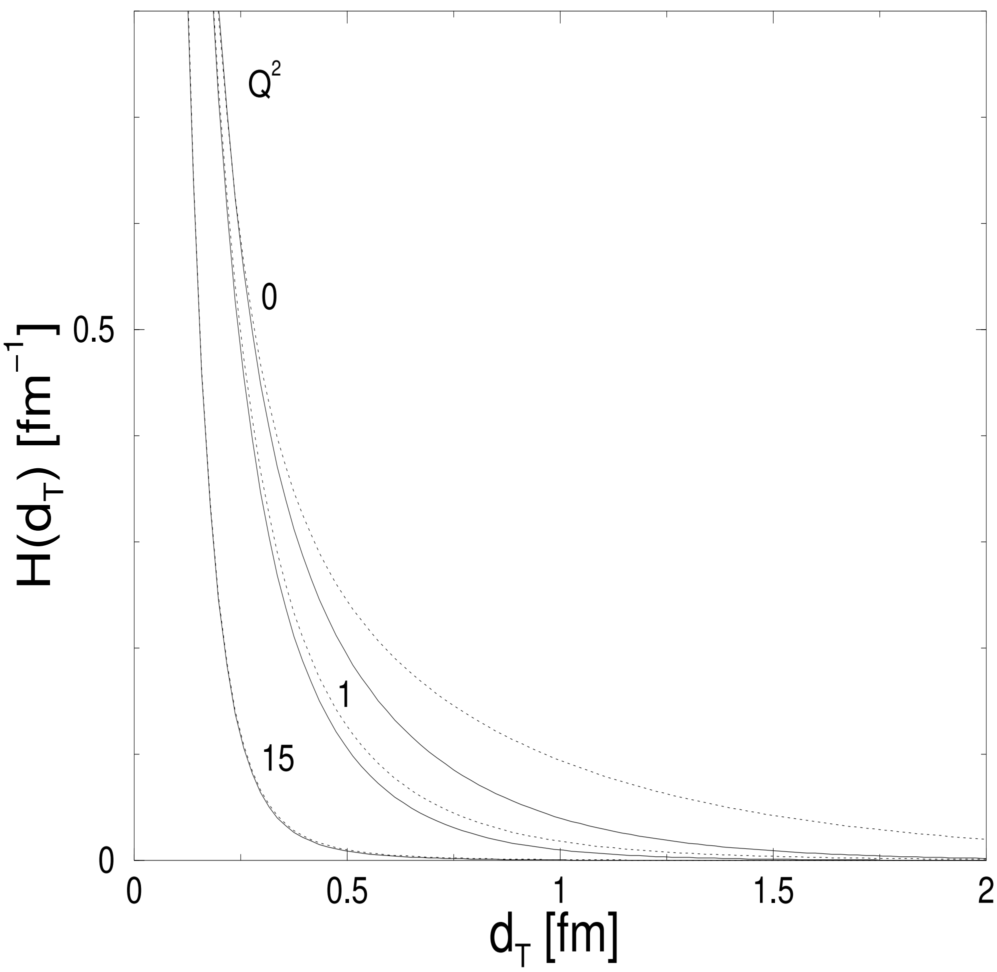

Figure 2.9: The weight function $H(d_\perp)$ for various Q^2 corresponding to photon wave-functions of perturbative form for $m_q^2 = 0.08$ GeV^2 (solid lines) and $m_q^2 = 0.02$ GeV^2 (dotted lines).

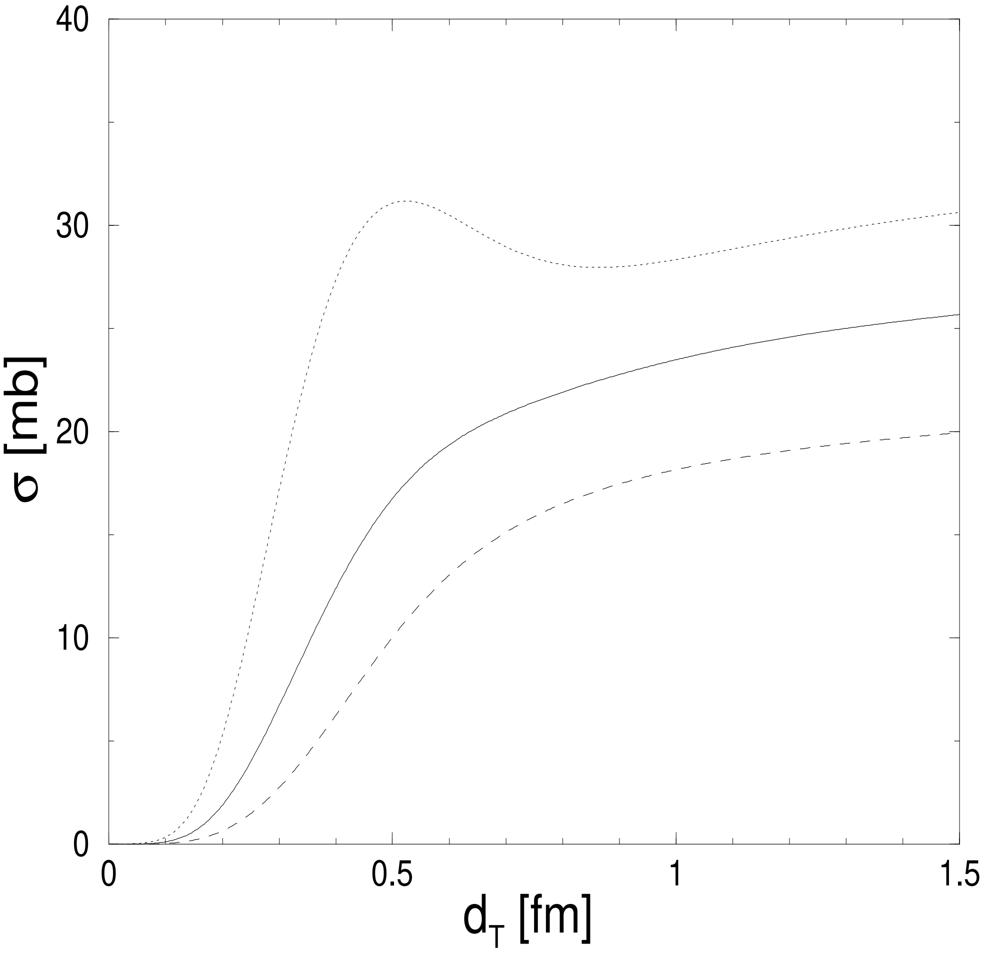

Figure 2.10: The FKS dipole cross section at $W = 10, 75, 300$ GeV (dashed, solid and dotted lines, respectively). Notice the onset of saturation effects at the top of the HERA region.

2.6 The McDermott-Frankfurt-Strikman-Guzey model

This model [75, 76] makes direct contact with pQCD, using (2.122) to relate the dipole cross-section to the gluon density. In an attempt to go beyond leading $\ln Q^2$ and $\ln(1/x)$, the gluon density and α_s are sampled at scales $\bar{Q}$ and x',

$$\hat{\sigma}_{\text{pQCD}}(x, d_\perp) = \frac{\pi^2 d_\perp^2}{3} \alpha_s(\bar{Q}^2) x g(x', \bar{Q}^2)\,, \tag{2.145}$$

where a $d_\perp$-dependence is introduced into the scales, x' and $\bar{Q}^2$. For the four momentum scale $\bar{Q}^2$, the phenomenological relation

$$\bar{Q}^2 = \frac{\lambda}{d_\perp^2} \tag{2.146}$$

was assumed where $\lambda = < d_\perp^2 > Q^2$. A theoretical procedure for defining $< d_\perp^2 >$ using the integral in $d_\perp$ for F_L in [77] gave a value of $\lambda \approx 10$. This value was used in [75], but it was later discovered that the inclusive cross sections are rather insensitive to its precise value in the range $\lambda = 4 - 15$ and that the lower value of $\lambda = 4$ appears to be favoured by the J/ψ-photoproduction data [76]. We shall adopt this lower value. The momentum fraction required to create a quark-antiquark pair of invariant mass $M_{q\bar{q}}^2 = (\boldsymbol{k}^2 + m_f^2)/(z(1-z))$ is

$$x' = \frac{M_{q\bar{q}}^2 + Q^2}{Q^2 + W^2}\,; \tag{2.147}$$

since k_T is Fourier conjugate to $d_\perp$ the following relationship was adopted [75] for a dipole of given transverse size $d_\perp$:

$$x' = x\left[1 + 0.75\frac{\lambda}{d_\perp^2(Q^2 + 4m_f^2)}\right]\,. \tag{2.148}$$

The dipole cross-section was then evaluated using the CTEQ4L gluon distributions [78] for a region $d_\perp \leq d_{T,c}$ in which (2.145) is appropriate, where the boundary $d_{T,c}$ is specified below. For large dipoles $d_\perp \geq d_{T,\pi} = 0.65$ fm, the form

$$\hat{\sigma}(d_\perp > d_{T,\pi}) = \hat{\sigma}(\pi P)\frac{3\, d_\perp^2}{2\, d_\perp^2 + d_{T,\pi}^2}\left(\frac{x_0}{x}\right)^{0.08}\,, \tag{2.149}$$

with an x-dependence characteristic of soft Pomeron exchange, is used, where $x_0 = 0.01$ and the value at $d_\perp = d_{T,\pi}\,,\ x = x_0$ is matched to the pion-proton total cross-section, $\sigma(\pi P) = 24$ mb. In the intermediate region $d_{T,c} < d_\perp < d_{T,\pi}$, the dipole cross-section was linearly interpolated between the boundary values at $d_{T,c}$ and $d_{T,\pi}$. For moderate x, the point $d_{T,c}$ is set by the boundary of the perturbative region in $d_\perp$: $d_{T,c} = d_{T,0} \equiv \sqrt{\lambda/Q_0^2} = 0.246$ fm, for $Q_0 = 1.6$ GeV which is the starting scale for the CTEQ4L partons (below this scale they are not defined). At small enough x, as a result of the rising gluon density, the small dipole cross section increases faster than the large dipole one and soon reaches hadronic size (tens of mb). This threatens to spoil the monotonic increase of $\hat{\sigma}$ with $d_\perp$. To prevent this the MFGS model implements taming corrections that guarantee that the small dipole cross section cannot reach more than half its value at $d_{T,\pi}$. This constraint implies a $d_{T,c}$ that shifts to increasingly small $d_\perp$.

Since the dipole cross-section depends on the gluon density, the skewedness of the particular process has to be taken into account. This means that the resulting dipole cross-section depends on the kinematics of a particular process and in this sense is not universal as expected in a general formulation. In anticipation to the DVCS analysis in Chapter 3, we show in Figure 2.11 the resulting MFGS dipole cross-section calculated for the DVCS process for which the skewedness parameter $\delta = x$. We adapted the skewed evolution package (which uses CTEQ4L gluon distribution as input) of Freund and Guzey [81] to produce these plots. We can see that the taming corrections are not important for $\lambda = 4$ in the HERA energy range. In conclusion, the MFGS model focuses on small dipoles, and while the behaviour for large dipoles is a sensible guess, no detailed attempt to resolve the intrinsic ambiguity in the wavefunction and cross-section for large dipoles discussed earlier has been made. For the DVCS analysis in Chapter 3, we shall restrict this model to $Q^2 > 1$ GeV^2, where one is relatively insensitive to this region due to the smallness of the wavefunction.

The MFGS model has a greater theoretical input than the FKS model but gives a less precise account of the DIS structure function F_2, its free parameters not being fitted to F_2 data. In contrast to the FKS model, it has not been used to predict Diffractive DIS.

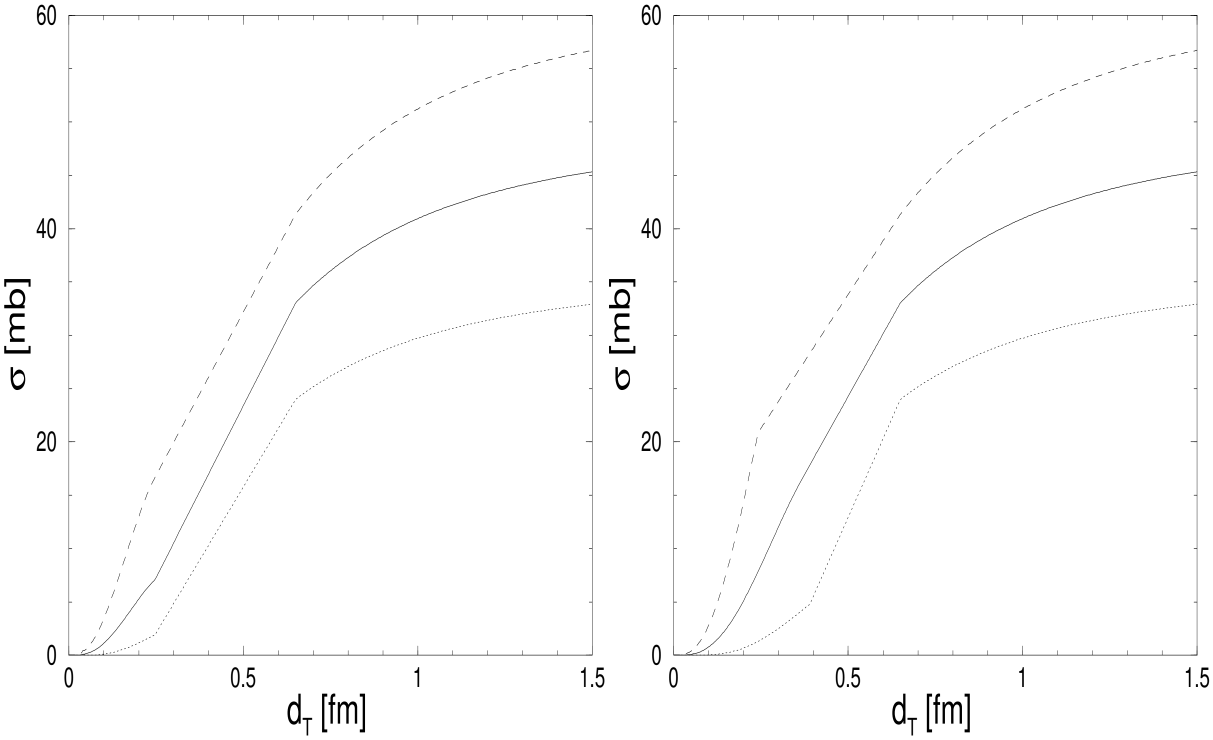

Figure 2.11: The MFGS dipole cross section at $W = 10, 75, 300$ GeV (dashed, solid and dotted lines, respectively). The shift of $d_{T,c}$ to smaller $d_\perp$ is not important for $\lambda = 4$ (left). The shift of $d_{T,c}$ to smaller $d_\perp$ is noticeable for $\lambda = 10$ (right).

Chapter 3

Deeply Virtual Compton Scattering

The first process we shall explore within the dipole model is Deeply Virtual Compton Scattering. DVCS is the diffractive production of a real photon in DIS,

$$\gamma^*(q) + p(p) \to \gamma(q') + p(p')$$

where the presence of the real photon in the final state forces the process to be purely transverse. This means that, at a given Q^2, DVCS is more sensitive than DIS to non-perturbative effects and at the same time is a good probe of the transition between the soft and hard regimes in the dipole model. In addition, if the virtuality of the initial photon goes to zero, the process reduces to real Compton scattering where the cross-section is known from real photoabsorption data. Hence, this limit can serve as a useful constraint on models [93]. We shall use the FKS and MFGS dipole models to calculate various DVCS observables. More generally, there is much interest in DVCS nowadays because it is the "cleanest" process (because of the real photon, an elementary quantum, in the final state) in which one can access a gpd. The results of our analysis have been published in [82].

3.1 Theoretical frameworks

The physics of DVCS can be described in two different formalisms (see e.g the concise summary in [85]). The first one is a hard scattering formalism based on a factorisation theorem proved in [86, 87].[1] The second approach is the colour dipole model. We shall briefly outline the pQCD approach, followed by an in-depth treatment of DVCS within the colour dipole model.

3.1.1 Hard scattering formalism

The factorisation theorem is valid at large Q^2, i.e at leading twist. The theorem asserts that the amplitude can be written as a convolution of a perturbatively calculable hard coefficient H with a generalised parton distribution (gpd) $f_{i/p}$ [86]:

$$\mathcal{H}_1 = \sum_i \int_{-1+x}^{1} dx_1 f_{i/p}(x_1, x_2, t, \mu) H_i\left(\frac{x_1}{x}, \frac{x_2}{x}, \mu^2\right) + \text{higher twist terms}\,. \qquad (3.1)$$

[1] A complete treatment of factorisation of DVCS is also given in [88].

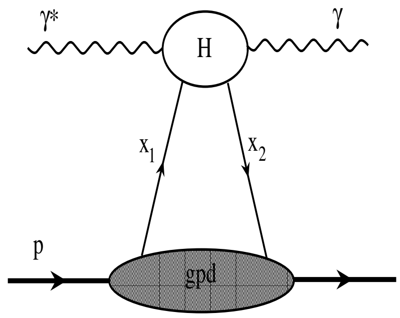

Figure 3.1: The DVCS process in the hard scattering formalism

The sum is over all parton species of type i. H_i is the hard scattering coefficient calculable in pQCD and $f_{i/p}$ is the generalised parton distribution. The soft and hard scattering regions are connected by two parton lines, the emitted parton carrying a fraction of longitudinal momentum x_1 while the returning parton carries longitudinal momentum fraction x_2 as shown in Figure 3.1. μ^2 is the factorisation/renormalisation scale appearing in parton distributions, taken to be equal to Q^2 here [86]. The subscript "1" (in $\mathcal{H}_1$) stands for the unpolarised (photon), (proton) helicity non-flip amplitude which survives the joint limit of small x and moderate t. In general, there are three other amplitudes to be taken into account, namely the unpolarised helicity flip amplitude and the two polarised counterparts [89]. The gpd at the starting scale Q_0^2 is a non-perturbative input. However, its evolution with Q^2 is given by DGLAP or Brodsky-Lepage type evolution equations [86].

Let us briefly review a leading order analysis of Frankfurt et al. [90]. Their starting point is to estimate the ratio

$$R \equiv \frac{\Im m \mathcal{A}(\gamma^* p \to \gamma^* p) \mid_{t=0}}{\Im m \mathcal{A}(\gamma^* p \to \gamma p) \mid_{t=0}} \,, \tag{3.2}$$

using a simple aligned jet model at the starting scale $Q_0^2 = 2.6$ GeV^2. This gives

$$R = \frac{Q_0^2}{Q_0^2 + M_0^2} \ln^{-1}(1 + Q_0^2/M_0^2) \approx 2 \; , \qquad (3.3)$$

for $M_0 \sim 0.4 - 0.6$ GeV. Hence, they could estimate the gpd at the input scale Q_0^2. The hard scattering amplitude is calculated using the quark box diagram shown in Fig. 3.2. The t dependence is introduced via the exponential ansatz (1.45) and the real part of the amplitude is reconstructed using a dispersion relation. The resulting predictions for the forward DVCS amplitude are in agreement with the H1 data [83]. We shall compare this estimation of the ratio R with our own in Section 3.3.

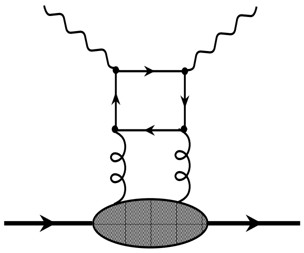

Figure 3.2: The leading order diagram for DVCS calculated in [90].

A detailed next to leading order analysis, using various models for the input GPDs has recently been completed [92].

3.1.2 Dipole framework

We believe a dipole analysis of DVCS is complementary to the QCD analysis we briefly outlined above. Going beyond leading twist, we can, in principle, establish quantitatively a regime in Q^2 for which the formal pQCD approach is valid. Previously, Donnachie and Dosch (DD) had given an analysis of DVCS within the dipole framework in [93]. The DD approach is based on a non-perturbative model with two

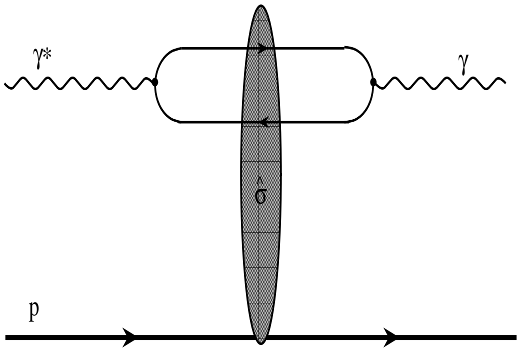

Figure 3.3: The DVCS process in the dipole model

typical non-perturbative parameters: The gluon condensate, $\langle g^2 FF \rangle$ and its correlation length a. The DD dipole cross-section is then given by

$$\hat{\sigma} = 0.098(\langle g^2 FF \rangle a^4)^2 d_\perp \left(1 - \exp\left(-\frac{d_\perp}{3.1a}\right)\right) . \tag{3.4}$$

In (3.4), the dipole cross-section has no energy dependence. This is implemented by multiplying (3.4) by a factor $(W/W_0)^{2\epsilon}$ where ϵ is the pomeron intercept and $W_0 = 20$ GeV. For large dipoles, $d_\perp > a$, the soft pomeron intercept, $\epsilon_s = 0.09$, is used while for small dipoles $d_\perp < a$, the hard pomeron intercept, $\epsilon_h = 0.42$, is chosen. Below the critical size $d_\perp^c = 0.16$ fm, the dipole cross-section is set to zero because the extrapolation of this non-perturbative model to large Q^2 overestimates small dipole contributions [93]. We compare the DD dipole cross-section with the FKS dipole cross-section in Figure 3.4 below. We note two features of the DD dipole cross-section. First, at $W = 75$ GeV, which is the average value of the H1 data on DVCS [83], the DD dipole cross-section is not unlike the FKS dipole cross-section, (except at large $d_\perp$ which is suppressed anyway by the photon light-cone wavefunction) and as we shall see both models are able to describe the data. Second, for higher energy ($W = 300$ GeV), the DD dipole cross-section develops a large discontinuity at the correlation

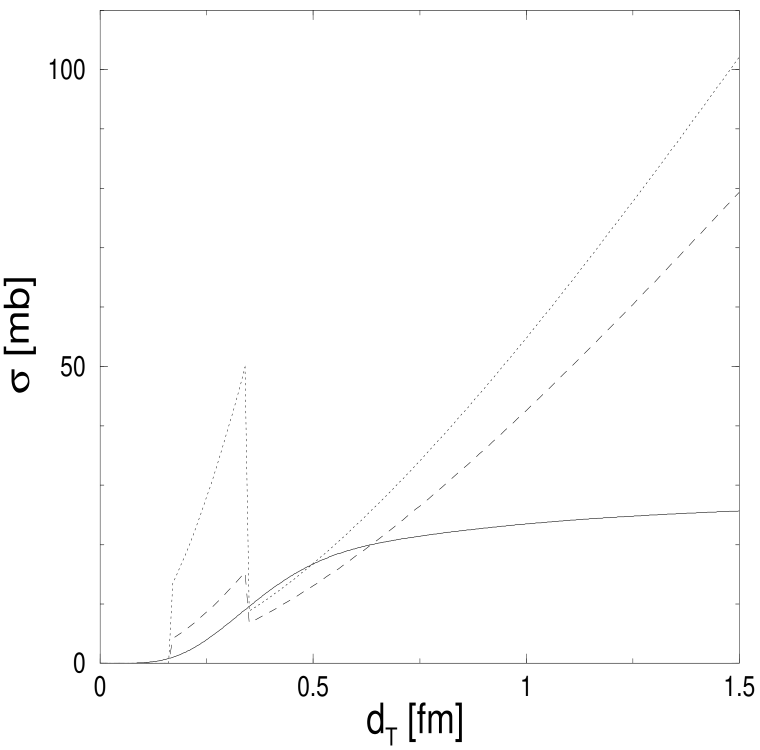

Figure 3.4: Solid line: FKS dipole cross-section at $W = 75$ GeV, dashed line: DD dipole cross-section at $W = 75$ GeV, dotted line: DD dipole cross-section at $W = 300$ GeV.

length a, the dipole cross-section for small dipoles exceeding that of large dipoles. This is not intuitively appealing but given that we have no precise knowledge of the analytic form of the dipole cross-section in the region matching small and large dipole sizes, we cannot exclude the possibility of this kind of behaviour as long as the model is able to describe experimental data.

Donnachie and Dosch chose to use $m_{u,d} = 0.21$ GeV, $m_s = 0.31$ GeV and $m_c = 1.3$ GeV in the photon light-cone wavefunctions without any enhancement factor (cf. FKS model). They obtain good agreement with data [93]. They also pointed out the importance of the real photoabsorption limit of DVCS.

Let us now turn to the calculation of the DVCS amplitude in the dipole model. The (dominant) imaginary part of the amplitude is given by

$$\Im m\mathcal{A} = \langle\gamma^*|\hat{T}|\gamma\rangle = s\int d^2\boldsymbol{d}_\perp\hat{\sigma}\int dz\Psi^*(d_\perp,z,0)\Psi(d_\perp,z,Q^2)\ . \tag{3.5}$$

where $\hat{\sigma}$ is the dipole cross-section. We first need to calculate the overlap of the initial and final photon wavefunctions, sum over all quark helicities, and convolute the resulting expression with the FKS or MFGS dipole cross-section. We have chosen a different notation $\mathcal{A}$ instead of $\mathcal{H}_1$ for two reasons. First $\mathcal{A}$ (unlike $\mathcal{H}_1$)[2] is the forward amplitude and second we define our amplitude including a factor of s (that is $\mathcal{A}$ have dimensions of GeV^2), whereas $\mathcal{H}_1$ is dimensionless. The simple relation between $\mathcal{A}$ and $\mathcal{H}_1$ is

$$\mathcal{H}_1 = e^{Bt/2}\frac{W^2}{4\pi\alpha_{e.m}\hbar c}\mathcal{A} \tag{3.6}$$

where we have included the t dependence of $\mathcal{A}$ using the exponential ansatz (1.45).

Let us calculate explicitly the amplitude $\mathcal{A}$. Since the final state photon is real, one of the photon wave function is evaluated at $Q^2 = 0$. Let us consider the longitudinal case first. From (2.104), we immediately see that the overlap of longitudinal photon wavefunction vanishes :

$$\Psi^{L^*}_{\pm\pm}(d_\perp,z,Q^2)\Psi^{L}_{\pm\pm}(d_\perp,z,0) = 0\ . \tag{3.7}$$

Therefore the only contribution to the DVCS amplitude is solely due to the transversely polarised photon. Using (2.105), with $\gamma = +$ and $h = +$ and $\bar{h} = -$, the

[2] The t dependence in $\mathcal{H}_1$ comes from the gpd.

overlap between the initial and final photon light-cone wavefunction is given by

$$\Psi^{T(\gamma=+)}_{+-}(d_\perp,z,Q^2)\Psi^{T(\gamma=+)}_{+-}(d_\perp,z,0) = \frac{3\alpha_{e.m}}{2\pi^2}\sum_{f=1}^{n_f} e_f^2\left[(1-z)^2\epsilon m K_1(\epsilon d_\perp)K_1(m_f d_\perp)\right] . \tag{3.8}$$

For $h=+$ and $\bar{h}=+$, we have

$$\Psi^{T(\gamma=+)}_{++}(d_\perp,z,Q^2)\Psi^{T(\gamma=+)}_{++}(d_\perp,z,0) = \frac{3\alpha_{e.m}}{2\pi^2}\sum_{f=1}^{n_f} e_f^2 m_f^2 K_0(\epsilon d_\perp)K_0(m_f d_\perp) . \tag{3.9}$$

Summing over $\bar{h}$ gives

$$\begin{aligned}\Psi^{T(\gamma=+)}_{h=+}(d_\perp,z,Q^2)\Psi^{T(\gamma=+)}_{h=+}(d_\perp,z,0) = \tfrac{3\alpha_{e.m}}{2\pi^2}\textstyle\sum_{f=1}^{n_f} e_f^2[(1-z)^2\epsilon m K_1(\epsilon d_\perp)K_1(m_f d_\perp)\\ +m_f^2 K_0(\epsilon d_\perp)K_0(m_f d_\perp)] .\end{aligned} \tag{3.10}$$

For $h=-$ and $\bar{h}=+$, the overlap is

$$\Psi^{T(\gamma=+)}_{-+}(d_\perp,z,Q^2)\Psi^{T(\gamma=+)}_{-+}(d_\perp,z,0) = \frac{3\alpha_{e.m}}{2\pi^2}\sum_{f=1}^{n_f} e_f^2\left[z^2\epsilon m_f K_1(\epsilon d_\perp)K_1(m_f d_\perp)\right] . \tag{3.11}$$

The overlap function vanishes for the configuration $\gamma=+$, $h=-$ and $\bar{h}=-$. Adding (3.10) and (3.11), (i.e summing over h) results in

$$\begin{aligned}\Psi^{T(\gamma=+)}(Q^2)\Psi^{T(\gamma=+)}(0) = \tfrac{3\alpha_{e.m}}{2\pi^2}\textstyle\sum_{f=1}^{n_f} e_f^2[(z^2+(1-z)^2)\epsilon m_f K_1(\epsilon d_\perp)K_1(m_f d_\perp)\\ +m_f^2 K_0(\epsilon d_\perp)K_0(m_f d_\perp)] .\end{aligned} \tag{3.12}$$

A similar calculation for $\gamma=-$, results in exactly the same expression. Since, we are *averaging* over photon polarisations and *summing* over all quark helicities, (3.12) is the final expression we need for the overlap of the photon light-cone wavefunctions. Note that in summing over quark flavours, we allow a charm contribution. The mass of the light quarks is taken to be $m^2_{u,d,s} = 0.08$ GeV^2 and that of the charm quark is taken to be $m_c^2 = 1.4$ GeV^2, which are the values chosen in the FKS model (See Table 2.1). There is no *a priori* reason to choose these values for the MFGS model, but recall that we restrict $Q^2 > 1.0$ GeV^2 in the MFGS model, so that anyway we are insensitive to the *light* quark masses in this model. We do *not* multiply the photon wavefunctions by the enhancement factor (2.143) in the MFGS case.

Convoluting this overlap function with the dipole cross-section and summing over the quark flavours, we get the imaginary part of the DVCS amplitude, (3.5).

3.2 The skewedness of the DVCS amplitude

Although to a good approximation, $t = 0$ in the DVCS process (see Chapter 1, Section 1.5.3), this does not mean that the momentum transfer at the proton vertex is zero [94]. To convert a virtual photon into a real photon, we have

$$(q + r)^2 = q'^2 = 0 \ , \tag{3.13}$$

where $r = p' - p$. Assuming $t = 0$, we have

$$q.r = \frac{Q^2}{2} \tag{3.14}$$

or

$$q.r = x(q.p) \tag{3.15}$$

where recall that x is Bjorken x. Choosing a frame in which $p = (p^+, \mathbf{0}, 0)$ and $q = (0, \mathbf{0}, q^-)$, this means

$$r^+ = xp^+ \tag{3.16}$$

that is the "+" component of the momentum transfer r is non-zero. For a general exclusive process,

$$r^+ = \xi p^+ \tag{3.17}$$

where ξ is called the *skewedness* of the amplitude. As we have just seen, the skewedness coincides with Bjorken x in the DVCS kinematics.

As we already mentioned in Section 2.6, we shall use the generalised (or skewed) gluon distribution in the MFGS dipole cross-section, (2.145), instead of the ordinary gluon distribution:

$$g(x', \bar{Q}^2) \rightarrow g(x', \bar{Q}^2, \xi) \tag{3.18}$$

with $\xi = x$. We use the computer code of Freund and Guzey [81] who modified the CTEQ4L package [78] to implement skewedness of the gluon distribution.

3.3 The FKS and MFGS dipole cross-section

Let us start by comparing the two dipole models we are going to use. Recall that the FKS dipole cross-section is universal: It does not depend on the particular physical process under investigation and we shall use exactly the same analytical form (with same parameters) as extracted from F_2 data. On the other hand, the MFGS dipole cross-section, for small $d_\perp$ depends on the gluon distribution and going beyond leading $\ln(1/x)$, we need use to use the skewed gluon distribution corresponding to the reaction under consideration. For DVCS, we shall use a skewed gluon distribution which (compared to the ordinary gluon distribution) has an additional dependence on the skewedness parameter, $\xi = x$ in this case. In this sense, there is a partial but controlled breakdown of the universality of the dipole cross-section [75].

In Figure 3.5, we compare both dipole cross-sections for $Q^2 = 4.5$ GeV^2 and $W = 75$ GeV which are the average values of Q^2 and W for the kinematic range of the H1 data for DVCS [83]. We find that the MFGS dipole cross-section is always greater than the FKS dipole cross-section. But recall in the FKS model, an enhancement factor modifies the photon light-cone wavefunction and that we cannot conclude at this stage that compared to the FKS model, the MFGS model will predict a larger cross-section for DVCS. On the contrary as we shall see, both models give very similar results for DVCS in the kinematic range of the H1 data.

3.4 Profiles in $d_\perp$

3.4.1 DVCS profiles

We now compare the contributions to the amplitudes arising from dipoles of different size. To do this, we perform the angular and z integrations to rewrite (3.5) as

$$\mathcal{A}(W^2, Q^2, t=0) = 2\pi \int dd_\perp p(d_\perp, Q^2) \tag{3.19}$$

where the profile function

$$p(d_\perp, Q^2) = \int dz d_\perp \Psi_T^*(z, d_\perp, Q^2) \hat{\sigma} \Psi_T(z, d_\perp, 0) \tag{3.20}$$

gives the relative contributions arising from dipoles of different size. The results for both models are shown in Figure 3.6. Two comments are in order regarding Figure 3.6:

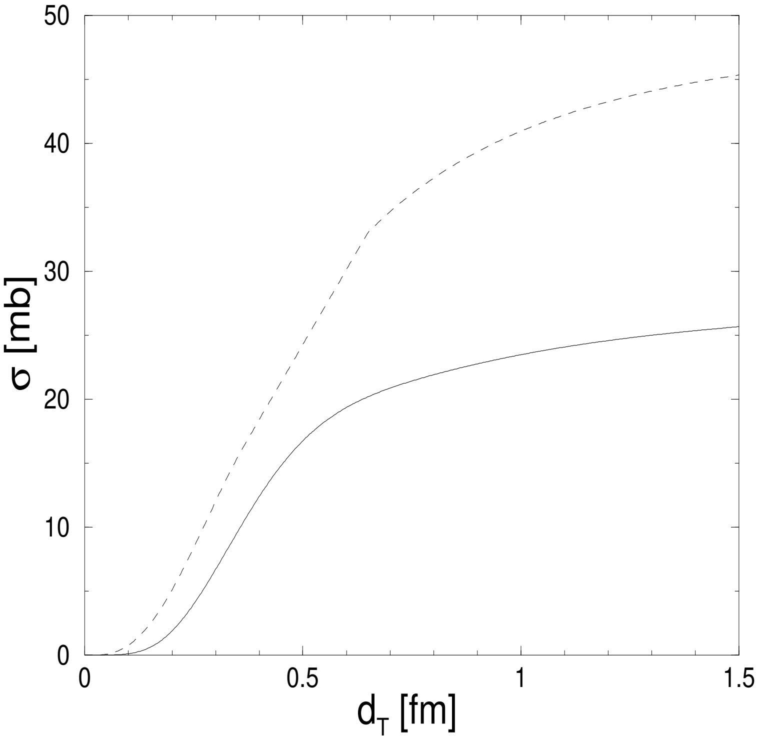

Figure 3.5: FKS dipole cross-section (solid line) and MFGS dipole cross-section (dashed line) at $W = 75$ GeV and $Q^2 = 4.5$ GeV^2. The difference between the MFGS dipole cross-section and the FKS dipole cross-section is significant.

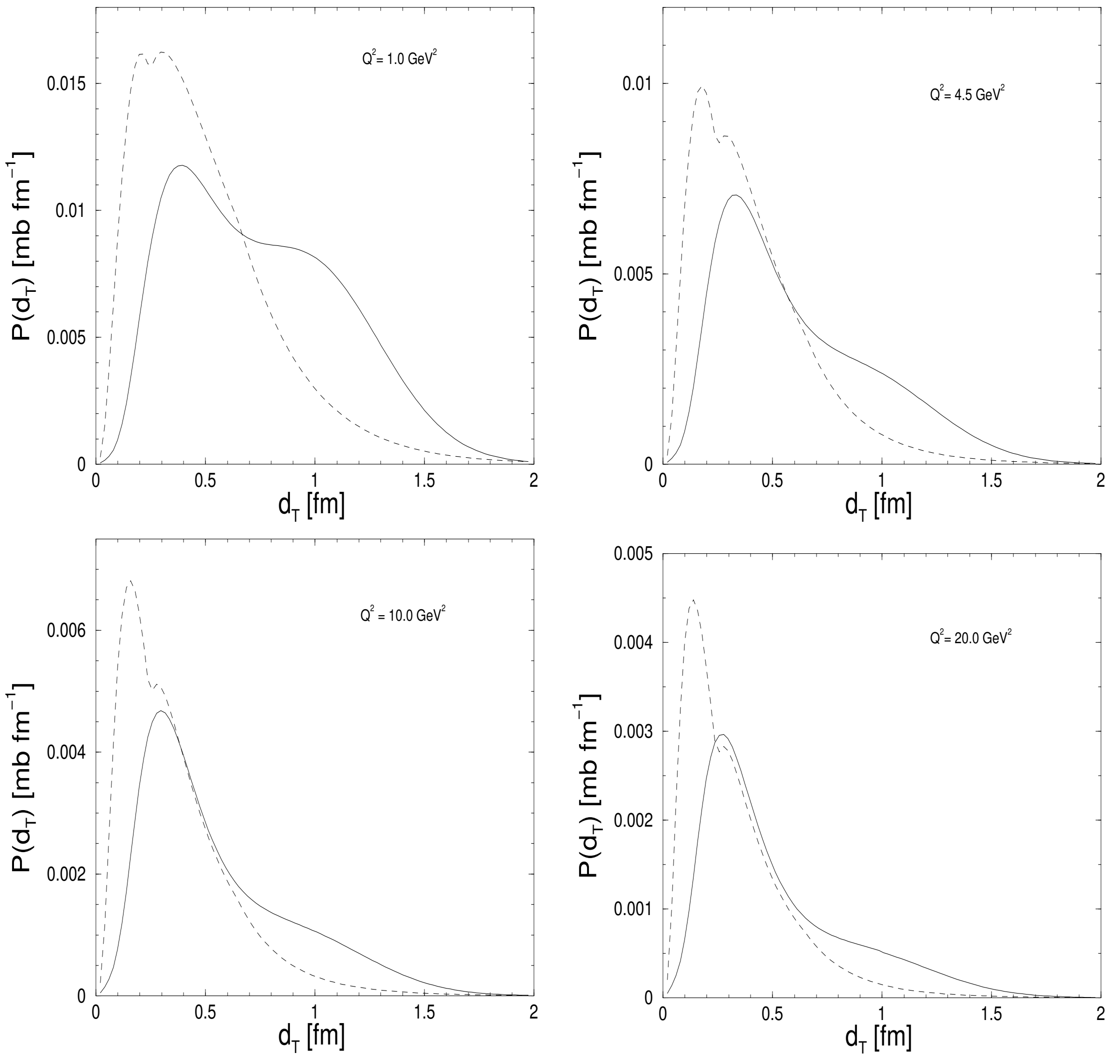

Figure 3.6: Profiles in $d_\perp$. Profiles shift to smaller $d_\perp$ as Q^2 decreases. MFGS profiles: dashed lines ; FKS profiles: solid lines

- As Q^2 increases, the profile shifts to smaller $d_\perp$. This can be readily understood in the light of our discussion of the photon wave functions in Section 2.3 : The photon wavefunctions suppress large dipoles at large Q^2. Put another way, as Q^2 *decreases*, we move progressively into the non-perturbative region where the contribution from large dipoles increases. This "Q^2 evolution" is analogous to the DGLAP evolution of pdfs, although no precise connection can be made at present [80].

- We see clearly that at any Q^2, the profiles for the two models are quite different. The peak is shifted to the left for the MFGS model. This means that the relative contribution of small dipoles is greater in the MFGS model. On the other hand, the FKS model has a large $d_\perp$ tail, which means that contributions from the large $d_\perp$ region is more important in this model than in the MFGS model. We therefore expect the MFGS model to predict a higher cross-section at large Q^2 and a lower cross-section at low Q^2 as compared to the FKS model.

3.4.2 Comparison with DIS profiles

It is also interesting to compare (3.20) to the corresponding profile function

$$\tilde{p}_T(d_\perp, Q^2) = \int dz\ d_\perp\ \psi_T^*(z, d_\perp, Q^2)\ \hat{\sigma}\ \psi_T(z, d_\perp, Q^2)\,, \tag{3.21}$$

for the forward Compton scattering amplitude in which both transverse photons have the same Q^2, which is related by the optical theorem to the transverse cross-section in DIS. The characteristic behaviour differences observed between DIS and DVCS are illustrated in Figures 3.7 and 3.8, using the FKS dipole model. For $Q^2 = 0$, the two profiles are obviously identical, and for all Q^2 they become identical for small $d_\perp$, since to leading order in $1/d_\perp$, the transverse wavefunction

$$|\psi_T^0(z, d_\perp, Q^2)|^2 \quad \rightarrow \quad \frac{3}{2\pi^2}\alpha_{e.m.} \sum_{q=1}^{n_f} e_q^2 \frac{z^2 + (1-z)^2}{d_\perp^2} \tag{3.22}$$

independent of Q^2. However, as can be seen, when Q^2 increases the large dipoles are less suppressed in the DVCS case than in the DIS case, so that the former is the "softer" process at any given Q^2.

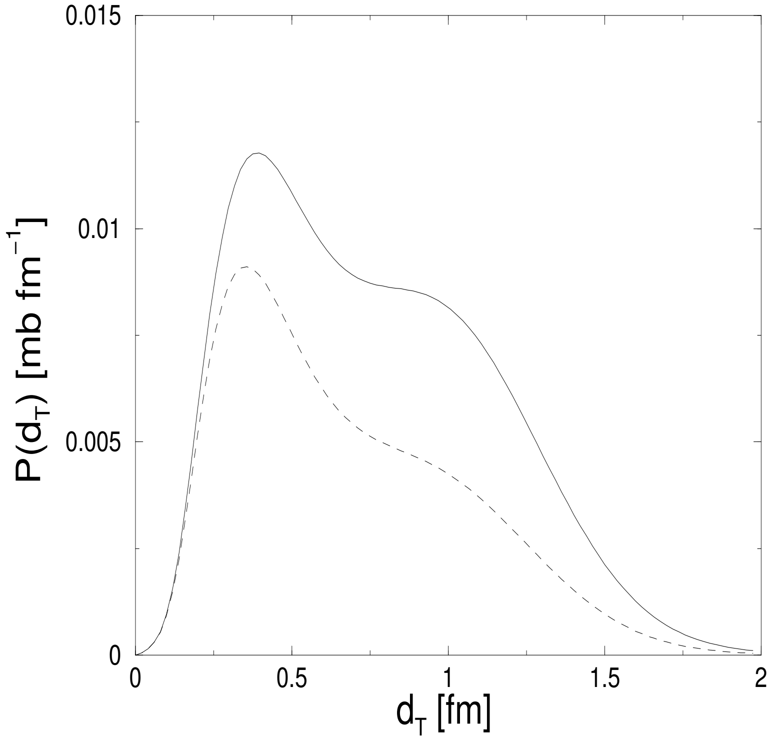

Figure 3.7: Comparison of the profile functions of (3.20, 3.21) for DVCS (solid line) and transverse DIS (dashed line) respectively at $Q^2 = 1.0$ GeV^2 and $W = 75.0$ GeV, employing the FKS model for the dipole cross section.

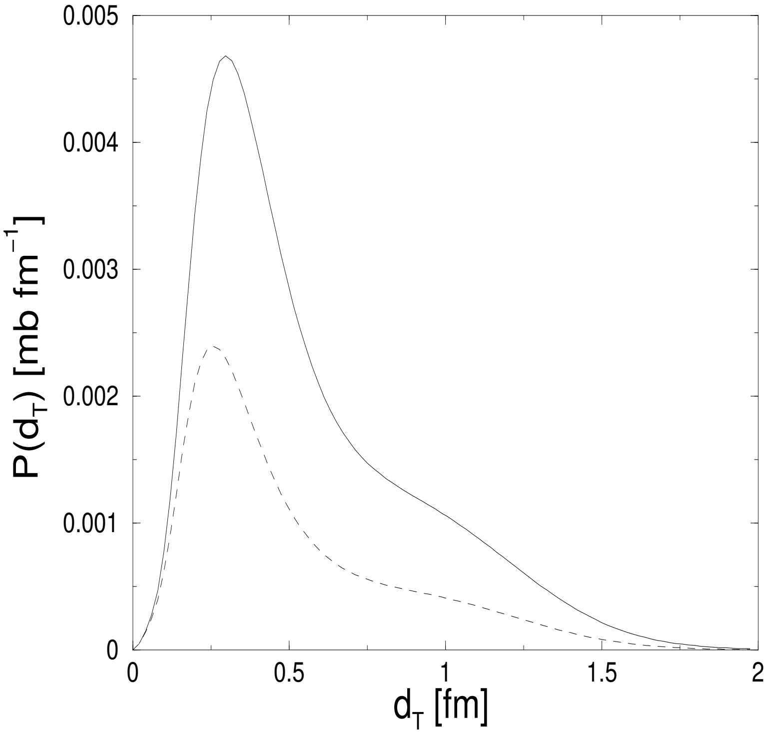

Figure 3.8: Comparison of the profile functions of (3.20, 3.21) for DVCS (solid line) and for transverse DIS (dashed line) at $Q^2 = 10.0$ GeV^2 and $W = 75.0$ GeV, employing the FKS model for the dipole cross section.

3.5 Ratio of "DIS" to DVCS imaginary amplitudes

We can also calculate the ratio R (See (3.2)). The predictions of our models are compared with (3.3) in Figure 3.9, suggesting somewhat larger values at $Q^2 = 2.6$ GeV^2, as can be seen. Notice that at $Q^2 = 0$, the ratio is *one* as expected. This can be shown

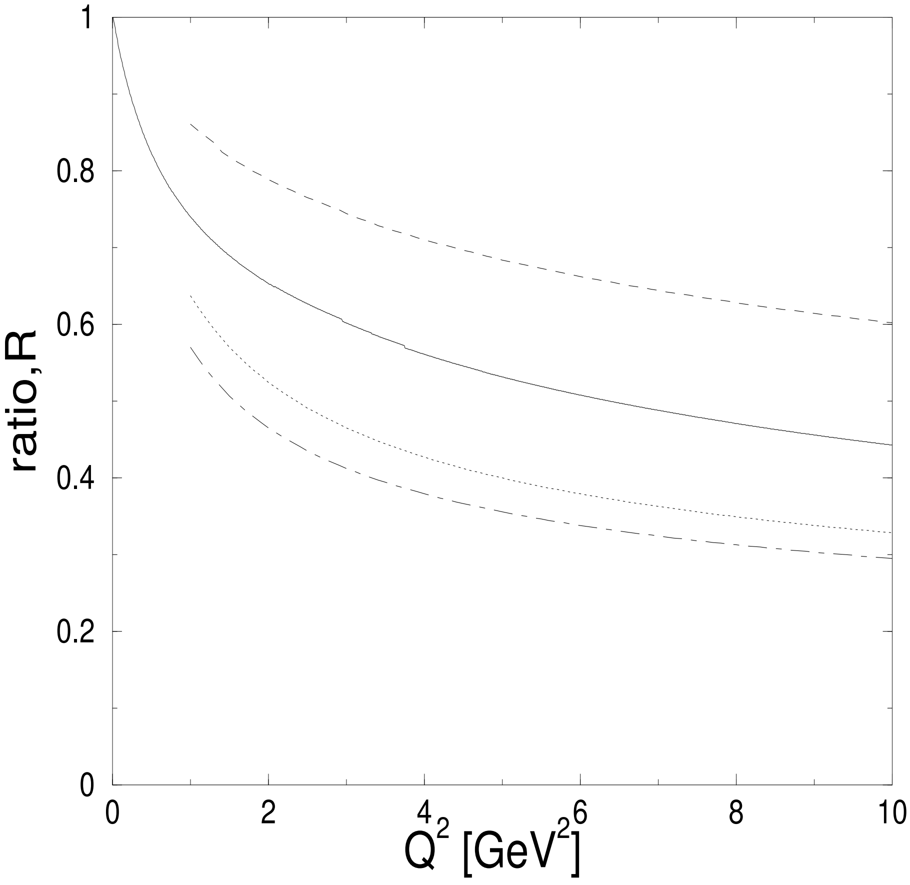

Figure 3.9: The ratio of the forward amplitudes for DIS and DVCS (see (3.2)) at $W = 75$ GeV: FKS (solid line); MFGS (dashed line); and the prediction of (3.3) for $M_0^2 = 0.6$ GeV^2(dotted line) and $M_0^2 = 0.4$ GeV^2 (dot-dashed line), respectively.

only in the FKS model which allows continuation to the photoproduction limit.

3.6 Reconstructing the real part of the amplitude

In the FKS model, the DVCS amplitude is given as a sum of two Regge terms, see (2.137). Using (1.34), it is straightforward to reconstruct the real part of the amplitude:

$$\Re e\mathcal{A} = \Im m\mathcal{A}^{\text{soft}} \tan\left(\frac{\lambda_s \pi}{2}\right) + \Im m\mathcal{A}^{\text{hard}} \tan\left(\frac{\lambda_h \pi}{2}\right) \tag{3.23}$$

where $\Im m\mathcal{A}^{\text{soft}}$ or $\Im m\mathcal{A}^{\text{hard}}$ are calculated using the soft term or the hard term of the FKS dipole cross-section respectively.

For the MFGS model, we need to do a two power fit to the imaginary amplitude first and then use (3.23). Some technical details are in order here. We found it necessary to do a constrained fit, precisely we fixed the soft Pomeron intercept,

$$\lambda_s = 0.08 \ . \tag{3.24}$$

The value that the fitting program MINUIT [95] give for the hard Pomeron intercept is[3]

$$\lambda_h = 0.31 \ , \tag{3.25}$$

which is physically reasonable. We do the fit for four values of Q^2: $Q^2 = 4.5$ GeV^2, $Q^2 = 9.0$ GeV^2, $Q^2 = 15.0$ GeV^2, $Q^2 = 20.0$ GeV^2, (covering the range over which the data is available), for $0 < W < 900$ GeV. Note that different fit values will be obtained for different ranges of Q^2 and W. A simple interpolation routine has then been designed to calculate the value of the real part for any other Q^2 value. The results are shown in Figure 3.10 and Figure 3.11. In Figure 3.10, we see that the imaginary amplitudes in the two models are very similar. However, for the real part of the amplitude, we notice that the FKS model shows steeper energy dependence at high energies.

Having calculated the real part of the amplitude, we shall now include this correction to our calculation of the total cross-section in what follows.

[3] For $Q^2 = 9.0$ GeV^2.

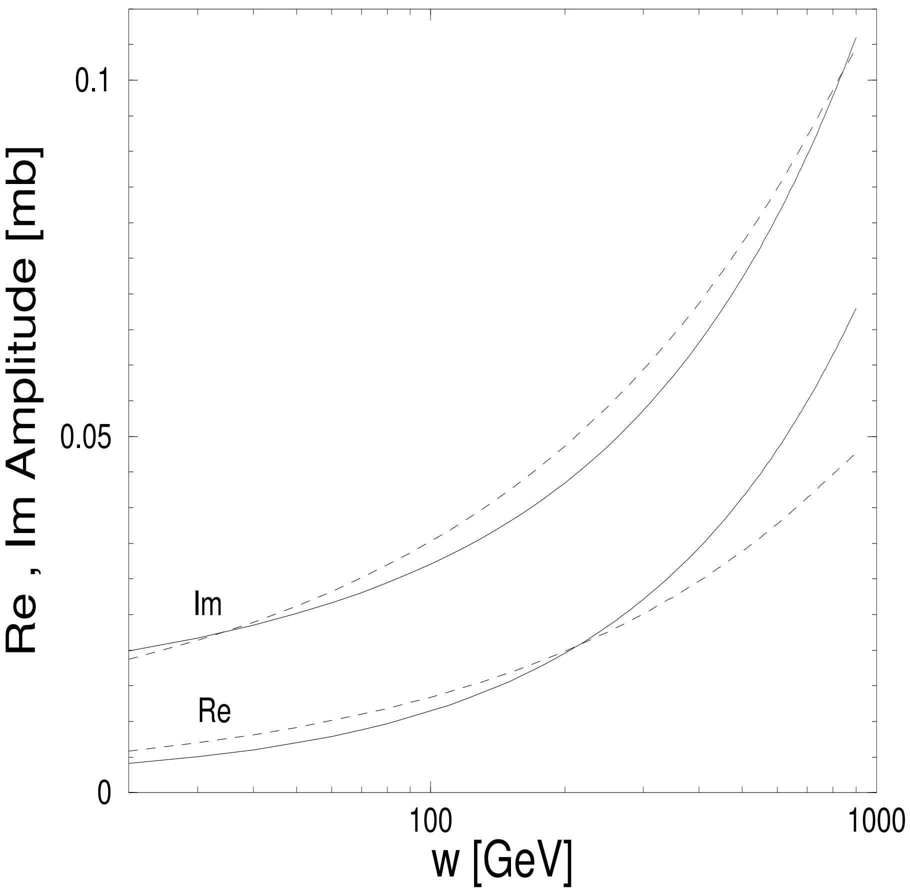

Figure 3.10: Real and imaginary parts of the DVCS amplitude for the FKS (solid lines) and MFGS (dashed lines) dipole models for $Q^2 = 4.5$ GeV^2.

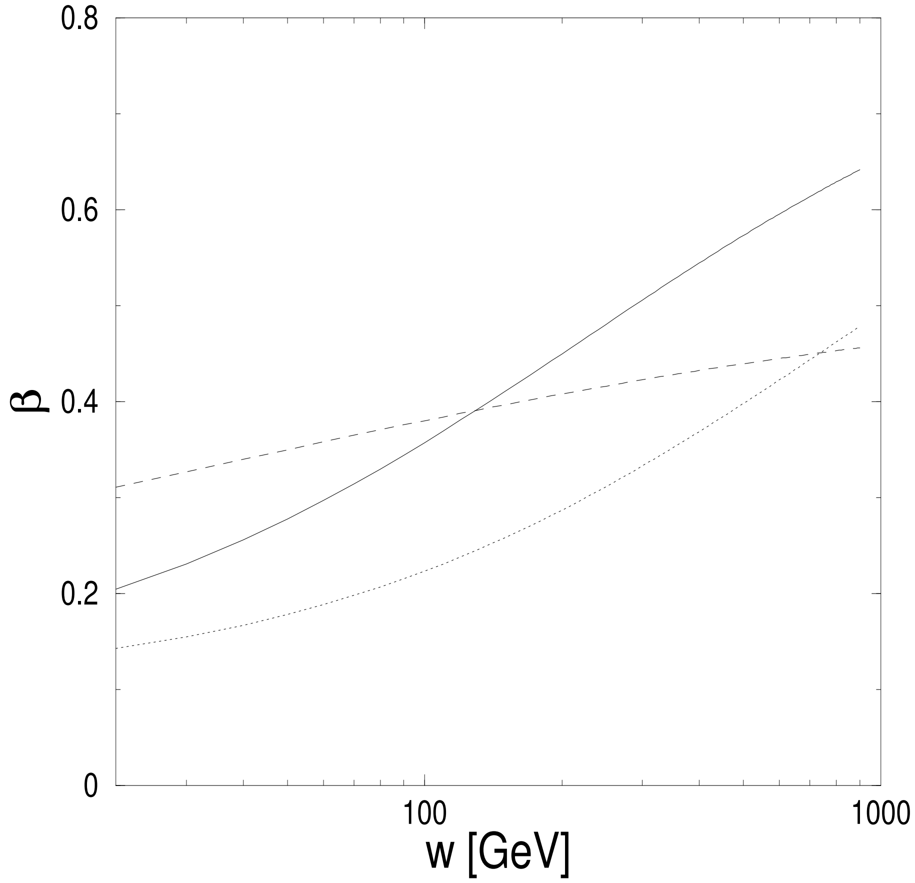

Figure 3.11: The ratio β of the real to imaginary parts of the DVCS forward amplitude at $Q^2 = 4.5$ GeV^2: FKS (solid line); MFGS (dashed line); and FKS at $Q^2 = 0$ GeV^2 (dotted line).

3.7 Photon level cross-section

3.7.1 Comparison with H1 data

The forward differential cross-section is given by

$$\frac{d\sigma}{dt}\mid_{t=0}=\frac{1}{16\pi s^2}\mid \mathcal{A}\mid^2 (1+\beta^2)\;. \tag{3.26}$$

Assuming the t dependence to be given by the usual exponential ansatz (1.44), the total cross-section is given by

$$\sigma(\gamma^* p\to\gamma p)=\frac{1}{B_{\rm DVCS}}\frac{d\sigma}{dt}\mid_{t=0}\;\;. \tag{3.27}$$

The Q^2 and W dependencies of the DVCS total cross-section are compared to H1 data in Figure 3.13 and Figure 3.12. In these figures, the vertical errors include statistical and systemaic errors added in quadrature, and the horizontal errors indicate the bin width of the data. We use the same value of $B_{\rm DVCS}=7.0$ GeV^{-2}, as used by H1 in their analysis [83]. It should be emphasised that the uncertainty in $B_{\rm DVCS}$ implies an associated uncertainty in the normalisation of the predictions, which could well be weakly Q^2 dependent.

As can be seen, the agreement with the H1 data [83] is encouraging for the basic features of the dipole models, despite the large statistical errors and the uncertainty in the diffractive slope parameter. Conversely, the close agreement between the predictions of the models out to energies well beyond the HERA energy range despite the fact that one implements saturation effects approximately and one does not, means that the total cross-section is not a good discriminator between them.

3.7.2 Comparison with ZEUS preliminary data

Recently, the ZEUS collaboration presented preliminary data on DVCS in the following kinematic range [84] :

$$2.0<Q^2<100\ \mathrm{GeV}^2\quad;\quad 10<W<180\ \mathrm{GeV} \tag{3.28}$$

First, let us show the FKS and MFGS dipole cross-sections evaluated at $W=89.0$ GeV and $Q^2=9.6$ GeV^2 in Figure 3.14. We notice that both dipole cross-section are quite

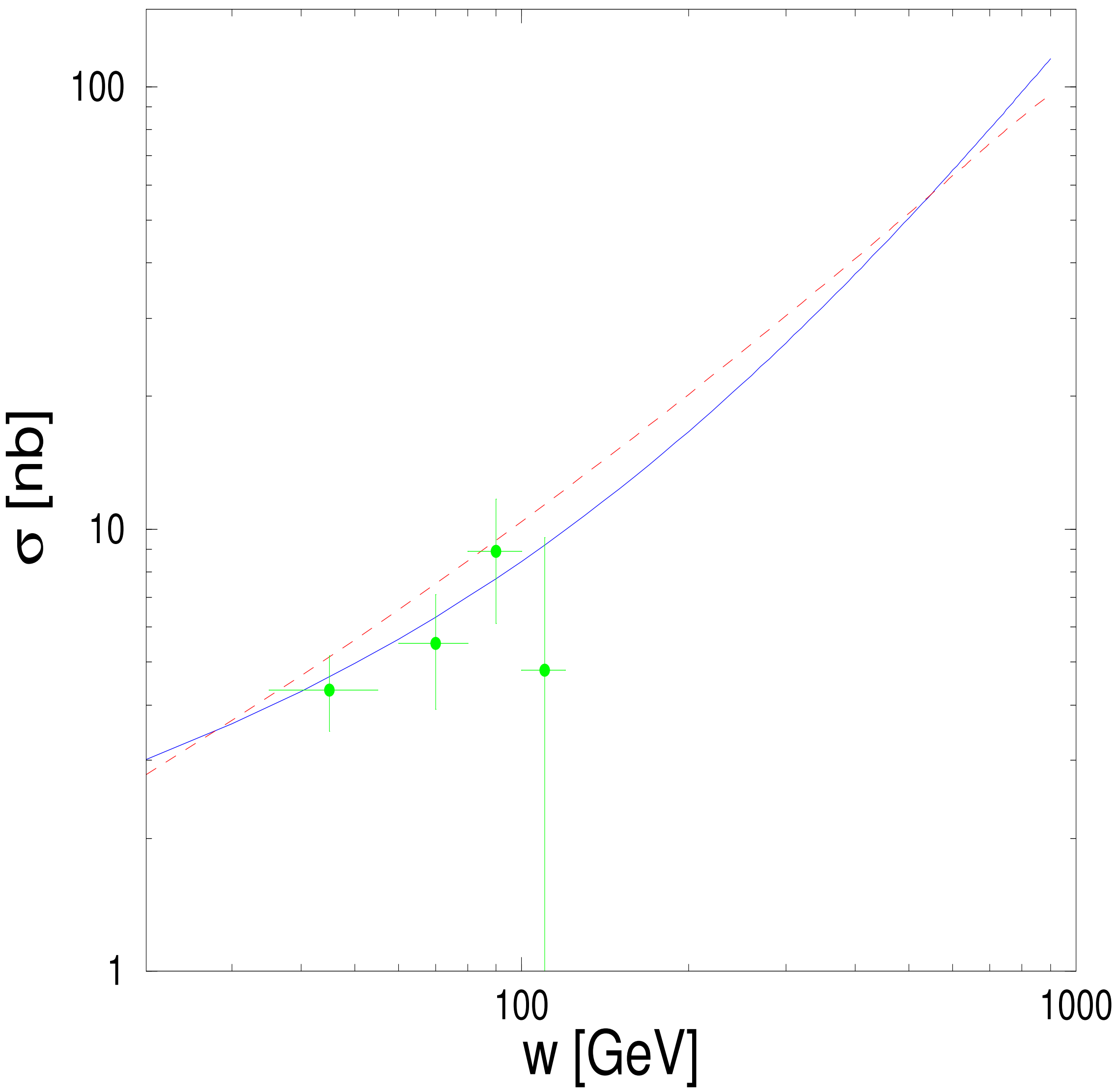

Figure 3.12: The energy dependence of the photon level DVCS cross section at fixed $Q^2 = 4.5$ GeV^2 : FKS (solid line); MFGS (dashed line). Data from H1 [83].

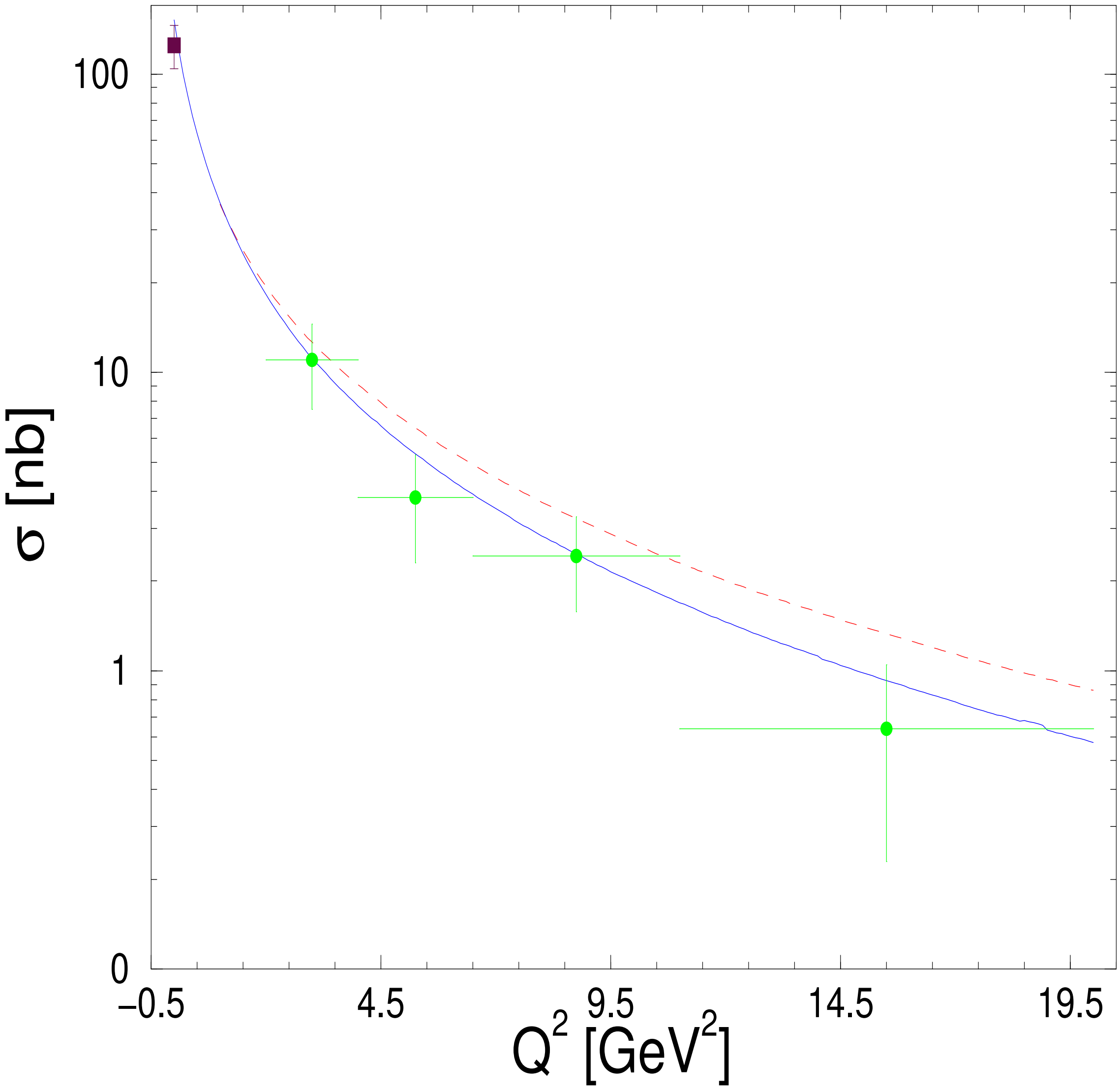

Figure 3.13: The Q^2 dependence of the photon level DVCS cross section at fixed $W = 75$ GeV : FKS (solid line); MFGS (dashed line). Data from H1 [83]. Note the photoproduction point (square data point) which is an important constraint on models. In our case, only the FKS model allows continuation to the photoproduction limit. The FKS curve (solid line) goes through the photoproduction point as shown.

similar except for large $d_\perp$. Hence, now we would expect the two models to give different predictions for DVCS cross-section in this kinematic range. Our predictions

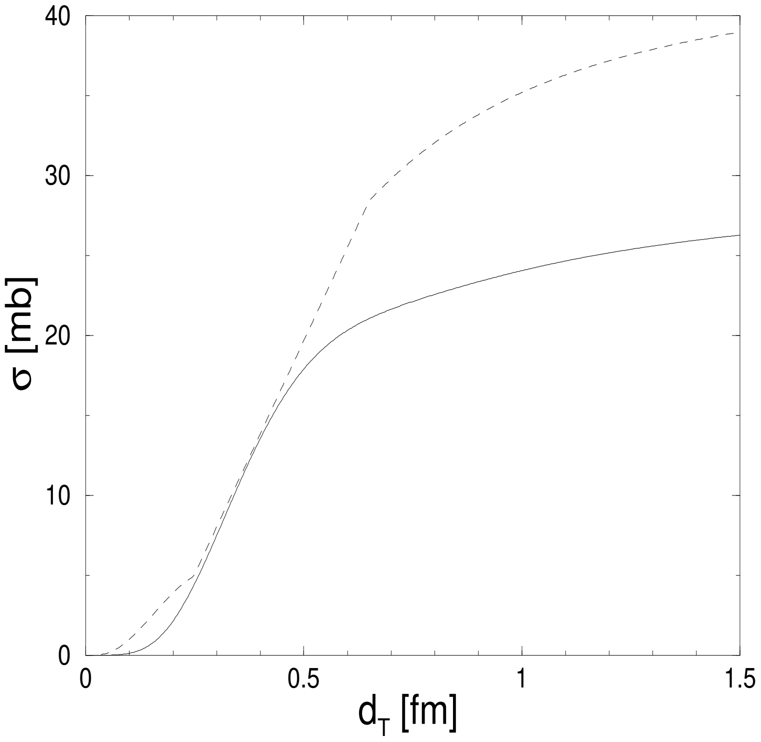

Figure 3.14: FKS dipole cross-section (solid line) and MFGS dipole cross-section (dashed line) at $W = 89.0$ GeV and $Q^2 = 9.6$ GeV^2. Except for large $d_\perp$, both models are quite similar.

compared to the new ZEUS data are shown in Figures 3.15 and 3.16. For this new kinematic range, we re-do the fit to the imaginary amplitude in the MFGS model, again constraining the soft Pomeron intercept to be 0.08 and calculated the real part exactly as before. We use a value of $B_{\mathrm{DVCS}} = 7.0$ GeV^{-2} for making these predictions. The two models give significantly different predictions in the kinematic range of the ZEUS data and the MFGS dipole model clearly gives a better description of the data.

In addition, we also note from [84] that the Q^2 dependence of the total cross-section is better described by the DD model [93] than the Frankfurt, Freund and Strikman calculation [90] while the W dependence of the cross-section is well described by both models.

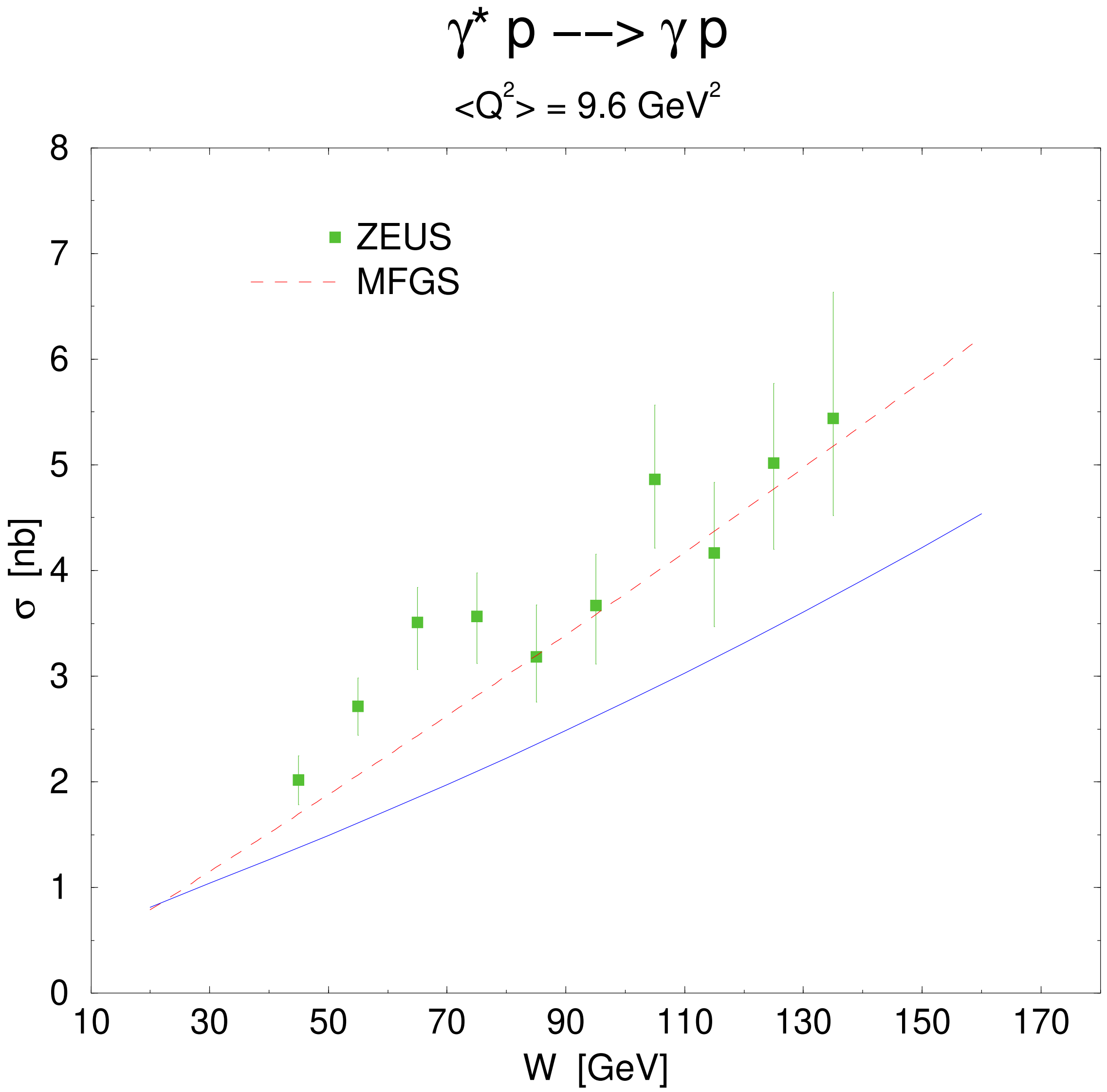

Figure 3.15: The energy dependence of the photon level DVCS cross section at fixed $Q^2 = 9.6\ \mathrm{GeV}^2$: FKS (solid line); MFGS (dashed line). *Preliminary* data from ZEUS [84].

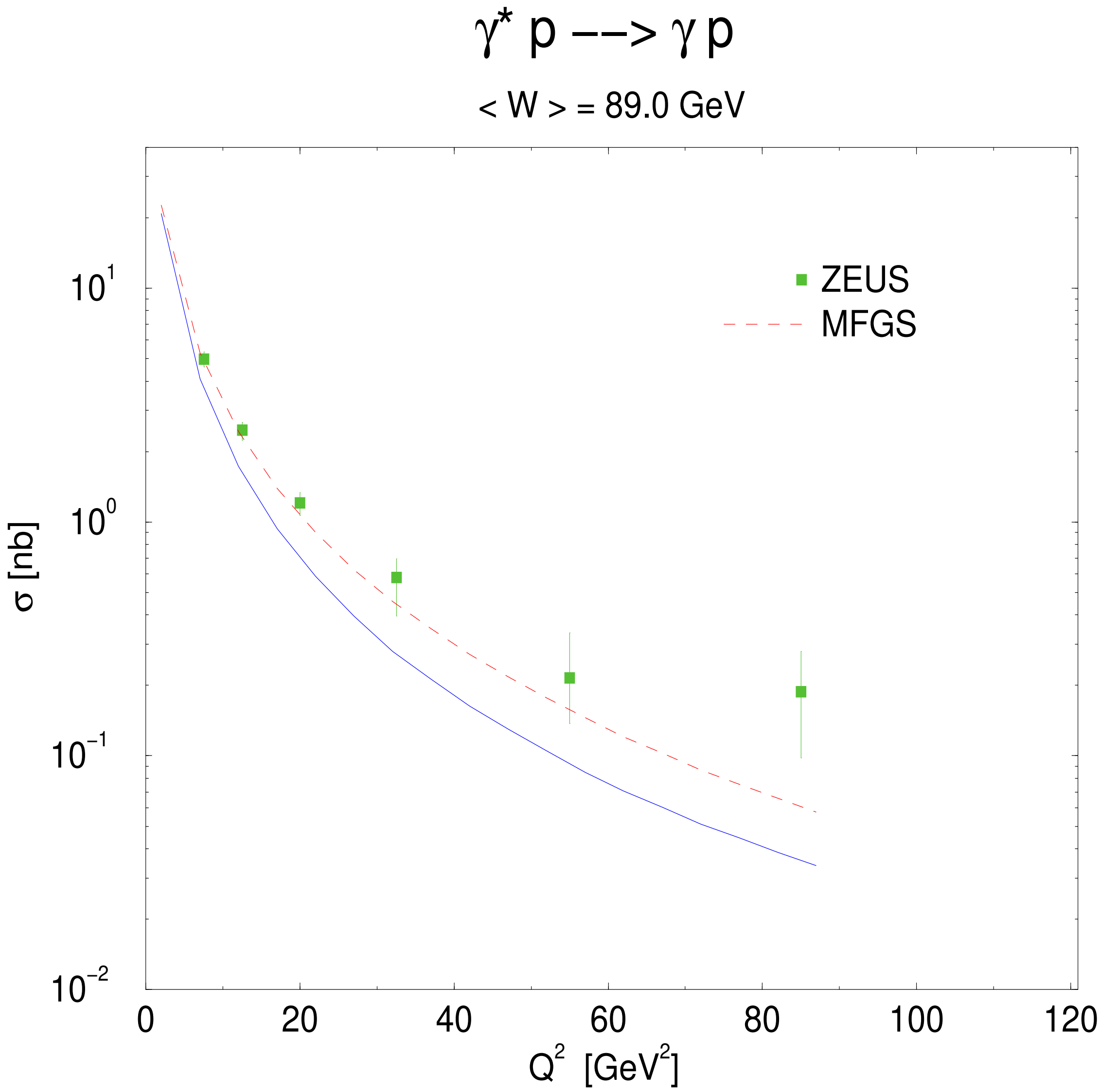

Figure 3.16: The Q^2 dependence of the photon level DVCS cross section at fixed $W = 89$ GeV : FKS (solid line); MFGS (dashed line). *Preliminary* data from ZEUS [84].

3.8 Lepton level process and asymmetries

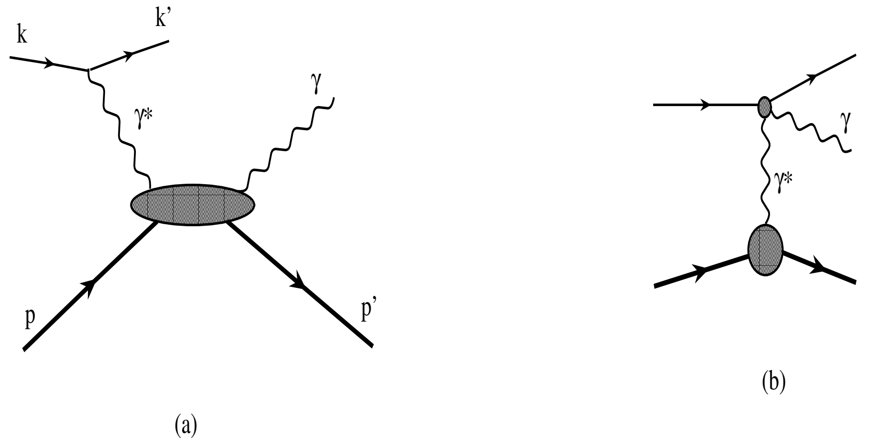

Figure 3.17: (a) : DVCS (b): BH. Here the upper blob means that the outgoing real photon can either attached to the incoming lepton or outgoing lepton.

At the lepton level, DVCS interferes with the QED Bethe-Heitler process in which a real photon is emitted off the lepton line instead. This interference is interesting since it offers us the unique opportunity to isolate the real and imaginary parts of the DVCS amplitudes via various azimuthal angle asymmetries. In this section, we follow closely here the presentation of [89, 92].

The triple differential cross-section of the lepton level process is given by [92]

$$\frac{d\sigma^3(e^\pm p \to e^\pm \gamma p)}{dx dQ^2 d\mid t\mid} = \int_0^{2\pi} d\phi \frac{d\sigma^4}{dx dQ^2 d\mid t\mid d\phi} = \frac{\alpha_{e.m}^3 x y^2}{8\pi Q^4}\left(1+\frac{4M^2x^2}{Q^2}\right)^{-1/2}\int_0^{2\pi} d\phi \mid \mathcal{T}^\pm \mid^2 \quad . \tag{3.29}$$

In (3.29), y is (in the proton's rest frame) the fraction of the incoming electron carried by the virtual photon; $y \sim (Q^2+W^2)/S$, where S is the total lepton-proton centre-of-mass energy (recall 1.57). M is the mass of the proton and the angle ϕ is the azimuthal angle between the hadron and lepton scattering planes. Later, we shall define asymmetries involving ϕ. The total amplitude $\mathcal{T}$ receives contributions from the pure DVCS amplitude, the pure BH amplitude and the interference between DVCS and BH. The BH amplitude is unambigously calculated within QED,

$$\mathcal{T}_{BH} = -\frac{e}{t}\varepsilon'^{*}_{\mu} L^{\mu\nu} J_{\mu} \tag{3.30}$$

where the $L^{\mu\nu}$ describes the leptonic tensor and J_{μ} is the hadronic current, parameterised in terms of the Pauli and Dirac elastic form factors of the proton [89].

The DVCS amplitude $\mathcal{T}$ is given by

$$\mathcal{T}^{\pm}_{DVCS} = \pm\frac{e^3}{q^2}\varepsilon'^{*}_{\mu} T^{\mu\nu}\bar{u}(k')\gamma_{\nu}u(k) \tag{3.31}$$

Here + sign is for a positron probe while − sign is for an electron probe. Notice that this sign difference for a positron and an electron probe cancels out for the BH amplitude since the two photons couple to the same lepton line in the BH process.

At small x and moderate t, it can be shown [89] that

$$T_{\mu\nu}(q, P, \delta) = -\tilde{g}_{\mu\nu}\frac{\bar{q}.V_{\mu}}{2\bar{P}.\bar{q}} \tag{3.32}$$

where

$$V_{\mu} = \bar{u}(P')\gamma_{\mu}\mathcal{H}_1 u(P)\ . \tag{3.33}$$

Here $\overline{P} = (P + P')/2$ and $\tilde{g}_{\mu\nu} = \mathcal{P}_{\mu\rho}g_{\rho\sigma}\mathcal{P}_{\sigma\nu}$ is a gauge invariant tensor constructed using the projection tensor $\mathcal{P}_{\mu\nu} \equiv g_{\mu\nu} - q_{\mu}q'_{\nu}/q.q'$ [89]. $\mathcal{H}_1$ is related to $\mathcal{A}$, the amplitude we have calculated in the previous section, via (3.6).

As we said earlier, the interference of DVCS with BH process offers a rare chance to isolate both the real and imaginary parts of the diffractive amplitude via azimuthal angle asymmetries. These asymmetries are conveniently discussed in a special frame with the proton at rest such that the direction of the vector $q \equiv k - k'$ defines the negative z axis. We can choose the incoming electron to have only a non-zero component along the positive x axis in the transverse $(x - y)$ plane. The azimuthal angle ϕ is the angle between the lepton $(x - z)$ and hadron scattering planes. The motivation for using this frame is that the u-channel BH lepton propagator has a particular simple Fourier expansion in the azimuthal angle ϕ [82]. Using this frame to specify ϕ, we now define the following three asymmetries:

- The (unpolarized) azimuthal angle asymmetry (AAA), measured in the scattering of an unpolarized probe on an unpolarized target, is defined by

$$\mathrm{AAA} = \frac{\int_{-\pi/2}^{\pi/2} d\phi (d\sigma^{DVCS+BH} - d\sigma^{BH}) - \int_{\pi/2}^{3\pi/2} d\phi (d\sigma^{DVCS+BH} - d\sigma^{BH})}{\int_0^{2\pi} d\phi (d\sigma^{DVCS+BH} - d\sigma^{BH})} \tag{3.34}$$

  where $d\sigma^{BH}$ is the pure BH term. The above approximation for the $u-$channel BH propagator leads to a non-trivial $\phi-$dependence of the pure BH term. To directly access the DVCS amplitudes, via the interference term, we define AAA with this piece subtracted.

- The single spin asymmetry (SSA), measured in the scattering of a longitudinally polarized probe on an unpolarized target, is defined by

$$\mathrm{SSA} = \frac{\int_0^{\pi} d\phi \Delta\sigma^{DVCS+BH} - \int_{\pi}^{2\pi} d\phi \Delta\sigma^{DVCS+BH}}{\int_0^{2\pi} d\phi (d\sigma^{DVCS+BH,\uparrow} + d\sigma^{DVCS+BH,\downarrow})}, \tag{3.35}$$

  where $\Delta\sigma = d\sigma^{\uparrow} - d\sigma^{\downarrow}$ and $\uparrow$ and $\downarrow$ signify that the lepton is polarized along or against its direction of motion, respectively.

- The charge asymmetry (CA) in the scattering of an unpolarized probe on an unpolarized target:

$$\mathrm{CA} = \frac{\int_{-\pi/2}^{\pi/2} d\phi \Delta d^C \sigma^{DVCS+BH} - \int_{\pi/2}^{3\pi/2} d\phi \Delta d^C \sigma^{DVCS+BH}}{\int_0^{2\pi} d\phi (d^+\sigma^{DVCS+BH} + d^-\sigma^{DVCS+BH})}, \tag{3.36}$$

  where $\Delta d^C \sigma = d^+\sigma - d^-\sigma$ corresponds to the difference of the scattering with a positron probe and an electron probe.

In the small-x limit, required for the dipole approximation, and at large Q^2, AAA and CA are directly proportional to the real part of the DVCS amplitude, and SSA to the imaginary part of the unpolarised amplitude (cf. Equations (30,40,43) of [89]). The predictions for both models are shown in Figure 3.18.[4] A measurement of the asymmetries would allow the predicted phase of DVCS amplitude for both models to be tested.

[4]M. McDermott adapted a code from [92] to produce these predictions.

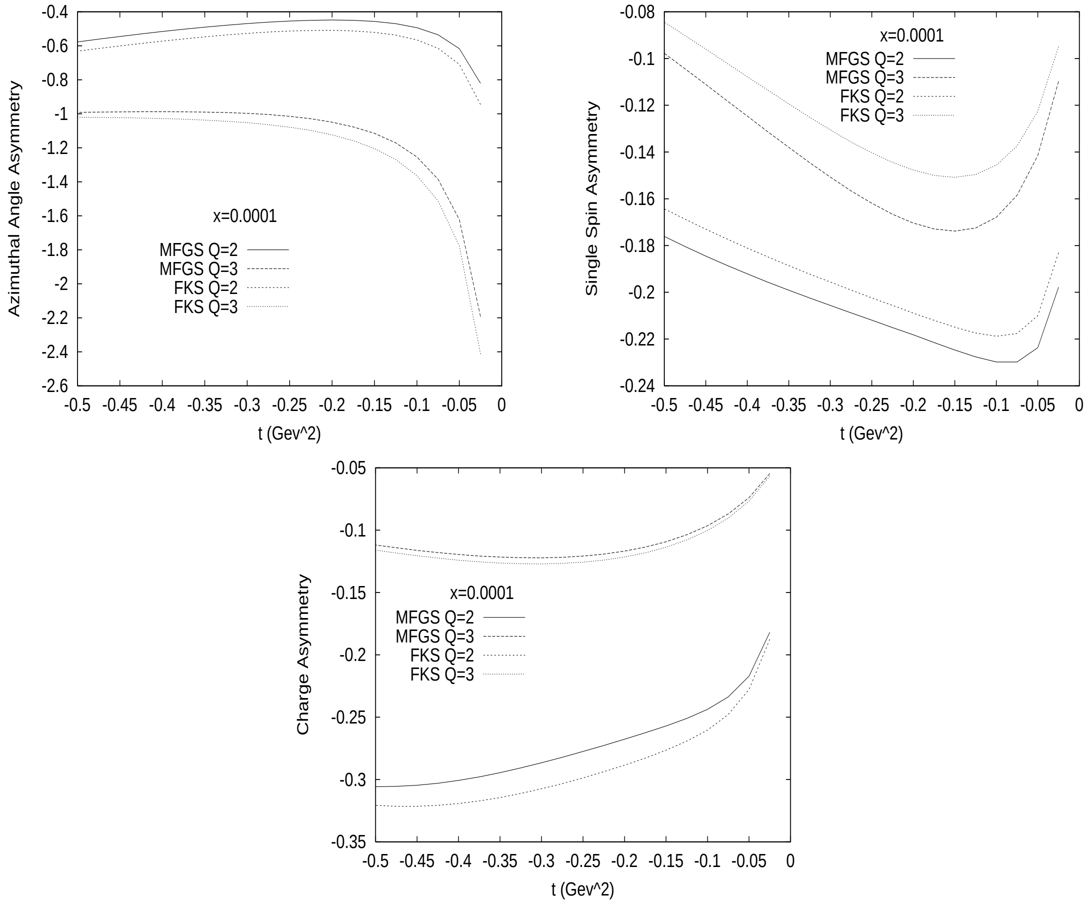

Figure 3.18: Compendium of results on asymmetries for fixed $x = 10^{-4}$, at two values of $Q = 2, 3$ GeV, accessible in the HERA kinematic range.

Chapter 4

Vector meson production

In this chapter, we investigate diffractive vector meson (ρ, ϕ and J/Ψ) electroproduction within the dipole model. The calculation is analogous to that for DVCS (see Chapter 3) in the sense that we only have to replace the (final state) photon light-cone wavefunction by that of the vector meson. This immediately introduces a major uncertainty in our analysis since the light-cone meson wavefunction is not known. Nevertheless, there exists a variety of phenomenologically well-constrained models of the meson light-cone wavefunction in the literature and we choose to explore and use two of them, one proposed by Nemchik, Nikolaev, Predazzi and Zakharov (NNPZ) [117, 118] and another by Dosch, Gousset, Kulzinger and Pirner (DGKP) [59]. The common feature, which is actually shared by all existing models [123], of both wavefunctions is the Gaussian dependence on the transverse size $d_\perp$. Having extracted the dipole cross-section from elsewhere and seen that it gives encouraging results for DVCS, it is tempting to argue that the dipole cross-section can be used to pin down the details of the meson wavefunction. It is in such a spirit that we shall use the FKS dipole cross-section to calculate vector meson production. In addition, we also give predictions for the GW dipole model, extending somewhat the recent analysis done by Caldwell and Soares (CS) [121].

After a short summary of the basic features of the HERA data, we discuss the contemporary theoretical frameworks used to calculate vector meson production. We then review the analysis of CS and explore in detail the derivation of the NNPZ meson light-cone wavefunction. We next introduce the DGKP wavefunctions before using both parametrisations to calculate vector meson production within the FKS and GW dipole models. Our analysis reveals some interesting conclusions which we present in the final section, together with our results.

4.1 Trends in the data

First, it is instructive to review the important features in the data. We shall focus on the energy and Q^2 dependence of the total cross-section, $\sigma(\gamma^* p \to V p)$ and the Q^2 dependence of ratio, $R = \sigma^L/\sigma^T$, where L and T denotes longitudinal and transverse polarisation of the photon (or vector meson) respectively. For a recent review of selected results from H1 and ZEUS on meson production, see [97]. Figure 4.1 (left) shows that the energy dependence of the cross-section for the light mesons is consistent with soft Pomeron exchange. On the other hand, the J/Ψ has a steeper energy dependence, reminiscent of hard Pomeron exchange. This is due to the large mass of the charm which provides a hard scale.

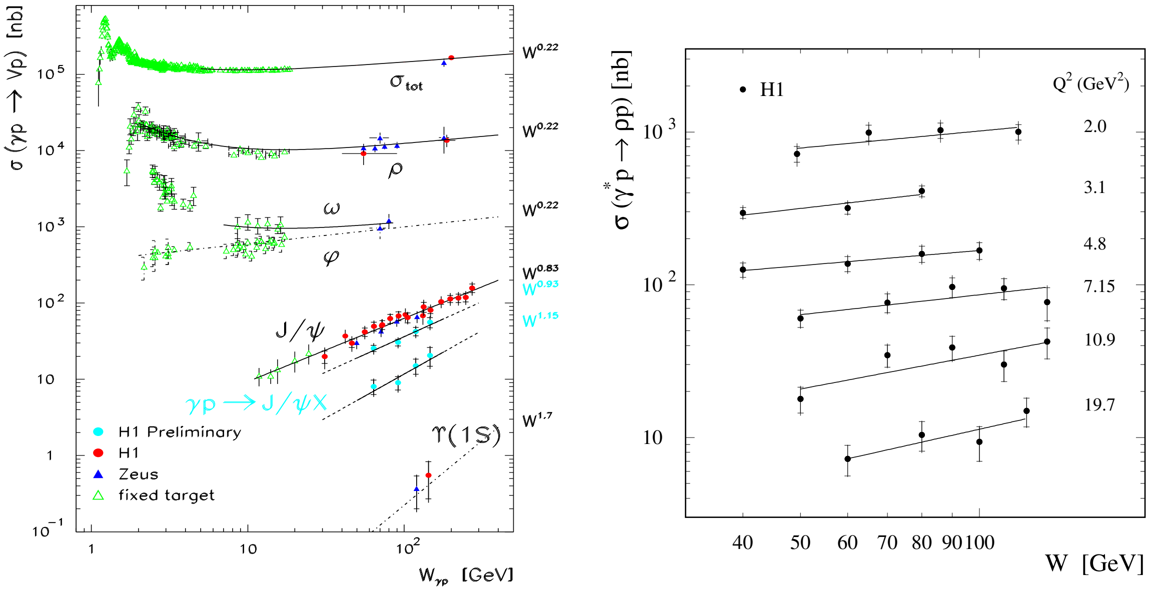

Figure 4.1: Left: Energy dependence of the total photoproduction cross-sections for the ρ, ω, ϕ, J/Ψ and Υ. The lines indicate W^n type power-law fits. Right: Energy dependence of the ρ cross-section at different Q^2 values. Deviation from soft Pomeron energy dependence is seen as Q^2 increases. Figures from [97].

For the light mesons, as Q^2 increases, deviations from soft Pomeron energy dependence become significant as we clearly see in Figure 4.1 (right). This deviation is also seen with increasing t. The obvious conclusion is *any* of the scales Q^2, M_v or t can serve as a hard scale in vector meson production, thus making a pQCD calculation reliable. Note also that the energy dependence of the cross-section for the J/Ψ does *not* steepen further upon increasing Q^2 as is shown in Figure 4.2 (left). The Q^2 dependence of the total cross-section for ρ production is shown in Figure 4.2. The data for the range in Q^2 (see solid line) can be fitted by [97]

$$\sigma(\gamma^* p \to \rho p) \sim \frac{1}{(Q^2 + M_\rho^2)^n} \tag{4.1}$$

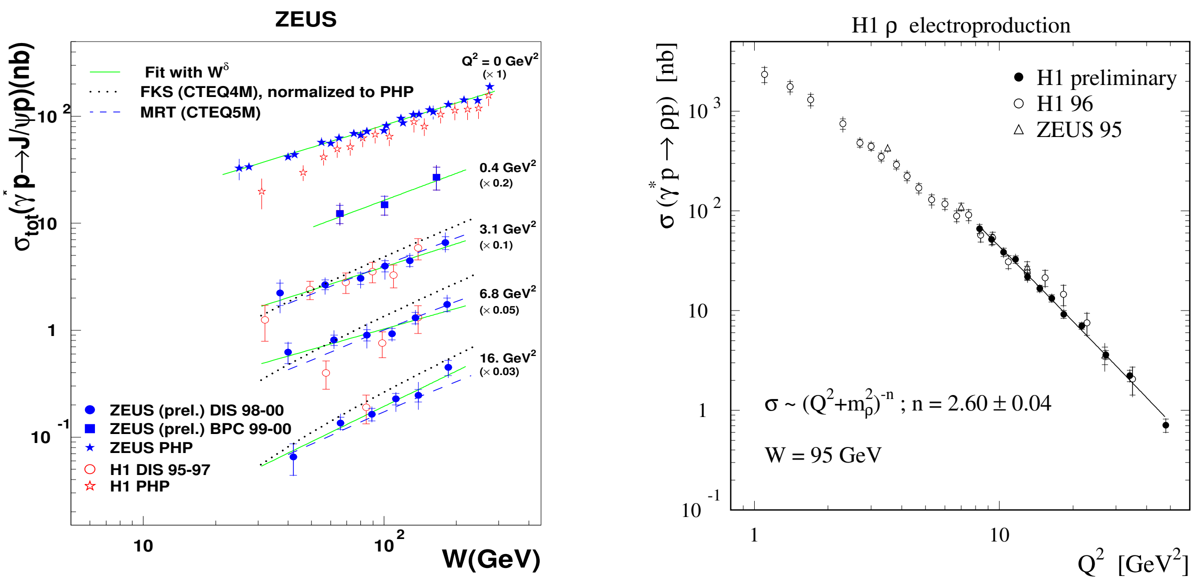

Figure 4.2: Left: The energy dependence of the cross-section for J/Ψ production. No further steepness is observed as Q^2 increases. Right: The Q^2 dependence of the cross-section for ρ production. Figures from [98].

with $n \approx 2.60$. At lower Q^2, the dependence is less steep. On the theory side, vector meson dominance predicts such a Q^2 dependence with $n = 2$. We shall see in the next Section, pQCD predicts $n \approx 2 - 2.5$ depending on the Q^2 range.

Figure 4.3 (left) shows the Q^2 dependence of the longitudinal to transverse ratio, $R = \sigma^L/\sigma^T$, indicating a gradual dominance of the longitudinal cross-section with increasing Q^2. At a given Q^2, the ratio R shows no apparent dependence on W as shown in Figure 4.3 (right). Experimentally, the polarisation of the vector meson is accessible through the measurement of the angular distributions of the decay products. Assuming s-channel helicity conservation (SCHC), R can then be deduced [96]. Although we shall always assume SCHC, it is worth noting that more recent experimental (see e.g [97]) and theoretical studies [100, 101] confirms SCHC violations. The largest amplitude violating SCHC is when a transversely polarised photon ($\gamma = +$) produces a longitudinal (light) vector meson, the ratio of that amplitude to the s-channel helicity conserving one (where a longitudinal photon produces a longitudinal meson) being proportional to $\sqrt{|t|}$ [44, 100]. This means that in the small t approximation, it is safe to assume SCHC.

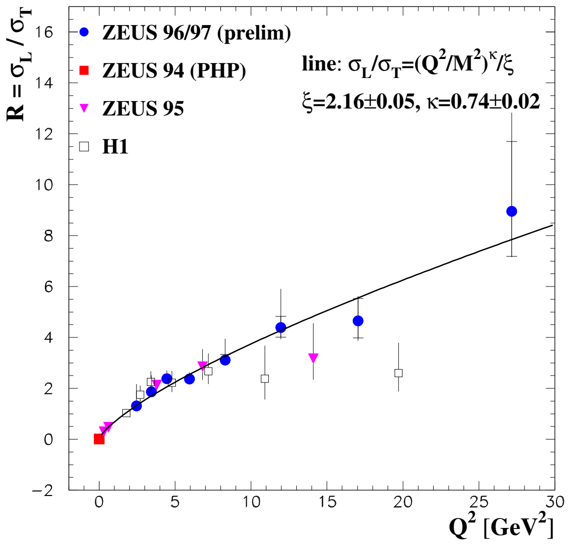

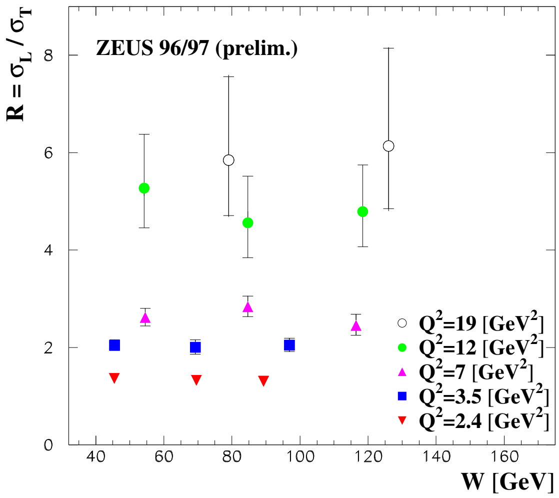

Figure 4.3: Left: the ratio, $R = \sigma_L/\sigma_T$ as a function of Q^2. The dominance of the longitudinal cross-section is gradually tamed as Q^2 increases. Right: the W-dependence of R at different values of Q^2. The data shows no apparent W-dependence at a given Q^2. Figures from [97].

4.2 Theoretical frameworks

There are various perturbative and non-perturbative approaches to analyse vector meson production.[1] Among the non-perturbative calculations [103], let us mention that of Dosch et al. [59] which is based upon the model of the stochastic vacuum, considering the dipole-proton interaction in a purely non-perturbative framework. Nevertheless, the photon splitting into the $q\bar{q}$ dipole and subsequent recombination into the vector meson are described by the light-cone wavefunctions of the photon and vector-meson respectively. We shall use their parametrisation (DGKP) of the meson light-cone wavefunction later.

We shall next proceed with a brief review of the existing pQCD calculations. Our aim is not to discuss how the different theoretical predictions compare to data but rather to review how they compare to each other. We shall then turn to the colour dipole approach and explore the existing calculations in some detail.

[1]for a review and complete list of references, see e.g [96, 44].

4.2.1 pQCD calculations

As we mentioned earlier, in the presence of a hard scale (Q^2, t or M_v^2 or some combination), a perturbative QCD calculation is legitimate. Ryskin [104] first derived a leading order formula for diffractive J/Ψ electroproduction. In this case, the J/Ψ mass provides the hard scale and the calculation remains valid in the photoproduction limit. The forward differential cross-section then reads

$$\frac{d\sigma}{dt}|_{t=0} = \frac{\Gamma_{ee}^{J/\Psi} M_{J/\Psi}^3 \pi^3}{48\alpha_{e.m}} \frac{\alpha(\bar{Q}^2)^2}{\bar{Q}^8}[xg(x,\bar{Q}^2)]^2 \left(1 + \frac{Q^2}{M_{J/\Psi}^2}\right) . \tag{4.2}$$

Here, $\Gamma_{ee}^{J/\Psi}$ and $M_{J/\Psi}$ are the the semi-leptonic decay width and mass of the J/Ψ respectively. The gluon density $g(x,\bar{Q}^2)$ is probed at the effective scales $\bar{Q}^2 = (Q^2 + M_{J/\Psi}^2)/4$ and $\bar{x} = 4Q^2/W^2$. To arrive at (4.2), a simple delta function $\delta^2(\boldsymbol{k})\delta(z-1/2)$ is used for the meson wavefunction. The quadratic dependence on the gluon density means that this process offers a good opportunity to constrain the parametrisation of the gluon density [105]. Notice that the W dependence comes solely from the $\bar{x}$ in the gluon density. Hence, the energy dependence is [44]

$$\sigma(\gamma^* p \to J/\Psi p) \sim W^{0.8} , \tag{4.3}$$

which is supported by the data, see Figure 4.1(left).

Brodsky et al. [106] generalised Ryskin's approach to include light mesons, working to the double logarithmic accuracy in $\ln Q^2$ and $\ln(1/x)$. The calculation is performed within light-cone perturbation theory and two different distribution amplitudes[2] are chosen for the meson wavefunction. They considered only longitudinal meson production and arrive at the following formula for the forward differential cross-section [106],

$$\frac{d\sigma^L}{dt}|_{t=0} = \frac{8\pi^4 f_v^2 \alpha_{e.m}\alpha_s^2(Q^2)\eta_v^2[xg(x,Q^2)]^2}{Q^6 N_c^2} , \tag{4.4}$$

where

$$\eta_v = \frac{1}{2}\frac{\int [dz/z(1-z)]\phi^v(z)}{dz\phi^v(z)} . \tag{4.5}$$

[2] The distribution amplitude is the light-cone wavefunction with the $\boldsymbol{k}$-dependence integrated out [60].

Regarding (4.4), let us only note the Q^{-6} dependence and the quadratic dependence on the gluon density and α_s which changes the Q^2 to some effective value, Q^{-n}, with $n \approx 4-5$ [97]. In (4.5), $\phi^v(z)$ is the distribution amplitude of the vector meson. The asymptotic form, $\phi^v \propto z(1-z)$ [58] and the Chernyak-Zhitnitsky form [107] for pions, $\phi^v \propto z(1-z)(1-2z)^2$ were chosen for the distribution amplitudes of the light meson. When choosing a simple delta function for the J/Ψ, the results of [106] reduce to those of [104].

Frankfurt et al. [108] quantified the kinematic limits of the pQCD approach, making several refinements to the pQCD formulae (4.4) including preasymptotic ($Q^2 \to \infty$) corrections. In a later paper [109], these same authors extended the formalism to transversely polarised meson production focusing on the J/Ψ and the Υ, for which the heavy quark mass guarantees the application of QCD factorisation. One of their main conclusions is that the J/Ψ *cannot* be considered as a non-relativistic system.

The above calculations have been put on firmer theoretical footing by Collins et al. [110] who proved a factorisation theorem for *longitudinal* vector meson production, to all orders of perturbation theory and encompassing all logarithmic corrections. The theorem is valid for asymptotic Q^2 and asserts that the amplitude can be factorised into a pQCD calculable part and a generalised parton distribution of the proton. This factorisation theorem is valid at any x, so that we can consider generalised quark distributions as well as generalised gluon distribution.

All calculations so far suffer from the lack of knowledge of the vector meson wavefunction. To circumvent this problem, Martin et al. [112] used an alternative approach based on parton-hadron duality. However, only ρ electroproduction can be considered in this framework.

Forshaw and Ryskin [111] used large t as a hard scale to predict the t dependence in vector meson production, using the BFKL equation. More recent developments along these lines can be found in [113].

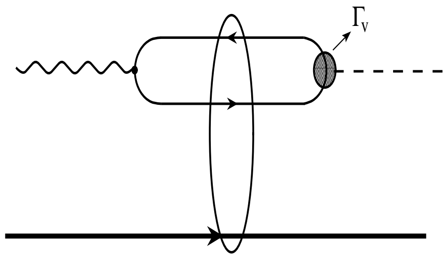

Figure 4.4: Vector meson production in the colour dipole model. Γ_v is the vertex function for the meson.

4.3 The colour dipole approach

As we already pointed out in Chapter 2, in the colour dipole model, the amplitude for vector meson production factorises as follows

$$\Im m\mathcal{A} = \langle V|\hat{\sigma}|\gamma^*\rangle = \int d^2\boldsymbol{d}_\perp \hat{\sigma} \int_0^1 dz \Psi_v^*(d_\perp, z)\Psi_{\gamma^*}(d_\perp, z; Q^2) \ . \tag{4.6}$$

where $\Psi_v(z, d_\perp)$ and $\Psi_{\gamma^*}(z, d_\perp; Q^2)$ are the light-cone wavefunctions of the vector meson and the photon respectively and $\hat{\sigma}$ is the dipole cross-section. Kopeliovich et al. [116] and Nemchik et al. [117, 118] considered vector meson production in the colour dipole framework. Nemchik et al. [117, 118] give explicit formulae for the forward longitudinal and transverse amplitudes (See Eqns. (7) and (8) of [118]) which we shall rederive later.[3] They propose a hybrid parametric form for the meson light-cone wavefunction, which is the sum of an oscillator and a Coulomb term. What we mean by this will become clear when we rederive the NNPZ parametrisation in Section 4.4.2. A novel feature of the analysis in [118] is the (first) extraction of the dipole cross-section from the vector meson production data. They also introduced the idea of

[3]Note that Eqn. (8) of [118] contains a mistake which was pointed out and corrected in [119]. See Section 4.6.1.

a scanning radius $d_\perp^s$ (r_s in their notation) at which the dipole cross-section is probed,

$$d_\perp^s \approx \frac{A}{\sqrt{M_v^2 + Q^2}}, \tag{4.7}$$

with $A \approx 6$, at large Q^2. Without knowing much about the meson wavefunction, we can explore the scanning radius idea of [117]. At large Q^2, the modified Bessel functions in the photon light-cone wavefunction are exponentially suppressed and small $d_\perp$ is favoured, implying a quadratic dependence of the dipole cross-section on $d_\perp^2$. Defining the profile function, $P(d_\perp)$ as

$$P(d_\perp) = 2\pi d_\perp \int dz \hat{\sigma} \Psi_v^*(d_\perp, z) \Psi_{\gamma^*}(d_\perp, z; Q^2) \tag{4.8}$$

and assuming that the vector meson wavefunction is sufficiently smooth in $d_\perp$, it follows that

$$p(d_\perp) \approx d_\perp^3 \exp(-\epsilon d_\perp) \; . \tag{4.9}$$

This function has a maximum at the scanning radius (4.7) with $A = 6$. The scanning radius (4.7) also tells us that the process is short-distance dominated if either Q^2 and/or M_v are large. Nevertheless, we should recall the assumption in deriving the scanning radius that $z \approx 1/2$. While this is certainly true for longitudinal vector meson production, the validity of this assumption in the transverse case depends on how much the end-points contributions are suppressed in the transverse meson light-cone wavefunction.

In [118], Nemchik et al. give predictions for vector meson production using an earlier parametrisation of the dipole cross-section and also invert the problem to extract the dipole cross-section from the data. One of their final comments is '*...As a matter of fact, if the dipole cross-section were known, the diffractive production $\gamma^* p \to Vp$ would be a unique local probe of the vector meson wavefunction at $r \approx r_s$* ($d_\perp \approx d_\perp^s$ in our notation); *this may well become one of the major applications of vector meson production...*', which is indeed the case in our present analysis.

Several other authors have investigated vector meson production in the colour dipole model [114, 115, 121, 123]. In [114], Frankfurt et al. applied the MFGS dipole model (see Chapter 2) to J/Ψ photoproduction. They reconsidered the scale setting in the gluon distribution, finding that the data favours a value $\lambda = 4$ (see Section 2.6, Chapter 2), which is precisely the value we used in DVCS analysis of Chapter 3. They also considered the effect of using a running quark mass and an energy-dependent diffractive slope. They further quantified the effect of skewedness of the gluon distribution finding it to be small (10% enhancement of the total cross-section).

In the more recent analysis of [123], the main focus is on investigating the onset of parton saturation in a model-independent way but as a by-product of their analysis, they give predictions on the forward longitudinal differential cross-section for the ρ meson using the GW dipole cross-section. Since they also use the NNPZ and DGKP parametrisations for the meson wavefunction, their results provide an useful cross-check for our own calculations.

Caldwell and Soares (CS) [121] used the Golec-Biernat-Wüsthoff dipole model to investigate ρ, ϕ and J/ψ electroproduction, using various parametrisations (with an increasing degree of sophistication) of the meson light-cone wavefunction. For the J/Ψ, they tried three different wavefunctions and for the light mesons ρ and ϕ, they used the harmonic oscillator wavefunction proposed in [118]. All free parameters are fixed using various constraints like the semi-leptonic decay width of the meson. We shall return to the choices of wavefunctions (and how they describe the data) made by CS in the next section.

4.4 Constructing the meson light-cone wavefunction

At present, we do not know how to construct the meson light-cone wavefunction from first principles in QCD. The best we can do is to use a physically reasonable ansatz which can describe both the short distance and long distance physics and the matching between the two. After reviewing the wavefunctions tried by Caldwell and Soares, we shall devote Section 4.4.1 to an in-depth analysis of the meson wavefunction proposed by Nemchik, Nikolaev, Predazzi and Zakharov (NNPZ) [118]. In Section 4.4.2, we discuss a different ansatz proposed by Dosch, Gousset, Kulzinger and Pirner (DGKP)

[59]. Note that other choices are available in the literature and for a review and references, we refer to e.g [108, 125, 126]. In particular, we note that the formal theoretical analysis of [125] forbids a factorising ansatz of the type $\phi(d_\perp)\xi(z)$ when $z \to 0$ or 1. Of course, if in a particular model, the end-points contributions are suppressed, this theoretical constraint has no *practical* importance.

4.4.1 Model-independent constraints on the meson wavefunction

Before discussing the different parametrisations for the meson light-cone wavefunctions, let us state the two main constraints on the meson light-cone wavefunction. The first one is the normalisation condition (2.76) which we shall rewrite in configuration space[4]

$$1 = \sum_{h,\bar{h}} \int d^2\boldsymbol{d}_\perp dz |\Psi^v_{h,\bar{h}}(\boldsymbol{d}_\perp, z)|^2 \,. \tag{4.10}$$

Second, the value of the light-cone wavefunction at the origin is related to the semi-leptonic decay width of the vector meson [106]:[5]

$$\int_0^1 dz \phi_v(d_\perp = 0, z) = \sqrt{\frac{\pi}{N_c}} \frac{f_v}{2e_f} \,. \tag{4.11}$$

where $\phi_v(d_\perp, z)$ is the scalar piece of the meson light-cone wavefunction; what we mean by this will become clear later, in Section 4.4.2. The coupling, f_v of the meson to electromagnetic current is related to the semi-leptonic decay width $\Gamma_{V\to e^+e^-}$ as follows [122],

$$\Gamma_{V\to e^+e^-} = \frac{4\pi\alpha_{e.m}}{3} \frac{f_v^2}{M_v} \,. \tag{4.12}$$

4.4.2 NNPZ wavefunction

Following [118], we shall construct the light-cone meson wavefunction in analogy with the photon light-cone wavefunction. The only but crucial difference, is an additional

[4]We omit to write a factor of 4π in the denominator, to be consistent with the normalisation conventions of the dipole formulation, see Chapter 2.

[5]This relation is true for the longitudinal meson light-cone wavefunction.

vertex factor for the vector meson, since we must account for its structure. The required vertex is therefore $\Gamma(z,\boldsymbol{k})\bar{v}\gamma^\mu u$ as shown in Figure 4.4. Proceeding in the same way as for the photon case (see Section 2.1.1), we can immediately write

$$\Psi^{L,T}_{h,\bar{h}}(\boldsymbol{k},z,M_v^2) = -ee_f\sqrt{z(1-z)}\frac{\overline{v}_{\bar{h}}(-\boldsymbol{k},1-z)\gamma.\varepsilon^{L,T}u_h(\boldsymbol{k},z)\Gamma(\boldsymbol{k},z)}{-z(1-z)M_v^2+\boldsymbol{k}^2+m_f^2}\ . \tag{4.13}$$

Choosing the longitudinal polarisation vector as

$$\varepsilon^L = \left(\frac{V^+}{M_v}, -\frac{M_v}{2V^+}, \mathbf{0}\right) \tag{4.14}$$

and the light-cone matrix elements [58, 59]

$$\bar{v}\gamma^+ u = 2\sqrt{z(1-z)}V^+\delta_{h,-\bar{h}}\ , \tag{4.15}$$

and

$$\bar{v}\gamma^- u = -\frac{\boldsymbol{k}^2+m^2}{\sqrt{z(1-z)}V^+}\delta_{h,-\bar{h}}\ , \tag{4.16}$$

we find that

$$\Psi^{v,L}_{h,\bar{h}}(\boldsymbol{k},z) = -\delta_{h,-\bar{h}}\left(\frac{z(1-z)M_v\Gamma(z,\boldsymbol{k})}{\boldsymbol{k}^2+m_f^2-z(1-z)M_v^2}+\frac{\Gamma(z,\boldsymbol{k})}{M_v}\right)\ . \tag{4.17}$$

Compared to the photon case, we have the additional vertex factor $\Gamma(z,\boldsymbol{k})$. This means that we do not get a delta function in $\boldsymbol{d}_\perp$ upon Fourier transformation and we cannot throw the "extra" term $\Gamma(z,\boldsymbol{k})/M_v$ away as we did for the $1/Q$ term in the photon case. At the same time, recall that we argued, in Section 2.1.1, that imposing gauge invariance takes the $1/Q$ term away in the photon case. Keeping the term in the meson case means that the light-cone meson wavefunction we obtain is *not* gauge invariant.[6]

Looking back at (2.92), we can rewrite the longitudinal photon wavefunction as

$$\Psi^{\gamma^*,L}_{h,\bar{h}}(\boldsymbol{k},z) = -\delta_{h,-\bar{h}}\sqrt{\frac{N_c}{4\pi}}ee_f 2Q\tilde{\phi}(\boldsymbol{k},z)\ . \tag{4.18}$$

where we have isolated the scalar part[7] of the photon light-cone wavefunction,

$$\tilde{\phi}_{\gamma^*}(\boldsymbol{k},z) = \frac{1}{\frac{\boldsymbol{k}^2+m_f^2}{z(1-z)}+Q^2}\ . \tag{4.19}$$

[6]Gluon emission must be considered to restore gauge invariance of the meson light-cone wavefunction, see the discussion in [126].

[7]This would indeed be the "light-cone photon wavefunction" in a toy model with scalar photons and (anti)quarks [127].

For the meson, the scalar part reads

$$\tilde{\phi}_v(\boldsymbol{k}, z) = \frac{\Gamma(\boldsymbol{k}, z)}{\frac{\boldsymbol{k}^2+m_f^2}{z(1-z)} - M_v^2} . \tag{4.20}$$

(4.20) as it stands is not very useful since we do not know $\Gamma(z, \boldsymbol{k})$. However, now that we have isolated the scalar part of wavefunction, we can deal with it separately. In fact, we shall make use of our knowledge of non-relativistic bound states to deduce an analytic form $\phi(\boldsymbol{k}, z)$. We shall solve Schrödinger equation for a particular potential and *boost* the Schrödinger wavefunction to a light-cone wavefunction. This boosting procedure being not well-defined, there exists several prescriptions in the literature to do the boost [128]. We shall use the most popular one proposed long-ago by Brodsky, Huang and Lepage (BHL) [129]. To obtain the BHL prescription, the off-shellness in the centre-of-mass frame is equated to that in the light-cone frame. For a meson with mass M_v and its constituents with momentum $k^\mu = (k_i^0, \vec{k})$, the off-shellness in the center-of-mass frame is

$$\epsilon_{CM} = M_v^2 - 4(\vec{k}^2 + m_f^2) . \tag{4.21}$$

Equating that to the off-shellness in the light-cone frame,

$$\epsilon_{LC} = M_v^2 - \frac{\boldsymbol{k}^2 + m_f^2}{z(1-z)} . \tag{4.22}$$

we obtain a connection between the 3-momentum $\vec{k}$ and the light-cone coordinates $\boldsymbol{k}$ and z,

$$\vec{k}^2 = \frac{\boldsymbol{k}^2 + m_f^2}{4z(1-z)} - m_f^2 \tag{4.23}$$

In terms of wavefunctions, this means that[8]

$$\phi^{\mathrm{S}}(\vec{k}^2) = \phi^{\mathrm{LC}}\left(\frac{\boldsymbol{k}^2 + m_f^2}{4z(1-z)} - m_f^2\right) . \tag{4.24}$$

(4.24) is the Brodsky-Huang-Lepage prescription which allows to infer the analytic form of a light-cone wavefunction using a Schrödinger wavefunction.

Let us first find the Schrödinger wavefunction for the following potential [117] :

$$V = V_{\text{Coulomb}} + V_{\text{oscillator}} \tag{4.25}$$

[8]For clarity, in the rest of this subsection, we denote a Schrödinger wavefunction by the superscript (S) and a light-cone wavefunction by the superscript (LC).

The Coulomb potential is

$$V_{\text{Coulomb}} = -\frac{4\pi\alpha_s C_F}{\vec{r}} \tag{4.26}$$

where $C_F = 4/3$ is a colour factor for quarks in a colour singlet. The harmonic oscillator potential is

$$V_{\text{oscillator}} = R\vec{r}^2 \tag{4.27}$$

where R is a free parameter.

Let us start with the Coulomb piece. Solving Schrödinger equation with the potential (4.26) we find

$$\phi^S(\vec{r}) = \mathcal{N}C \exp\left(\frac{-|\vec{r}|}{2Ca}\right) , \tag{4.28}$$

where a is the Bohr radius,

$$a = \frac{3}{8m_r\alpha_s} . \tag{4.29}$$

$\vec{r}$ is the relative 3-vector between the quark and the antiquark, $\mathcal{N}$ is a normalisation constant and C is a free parameter. m_r is the reduced mass ($m_r = m_f/2$) of the quark-antiquark system which naturally comes from the separation of variables in a non-relativistic two-body system. To be able to use the BHL prescription (4.24) we need to do a three-dimensional Fourier transform of (4.28) to momentum space,

$$\tilde{\phi}^S(\vec{p}) = \mathcal{N}C \int d^3\vec{r} \exp\left(\frac{-r}{2Ca}\right) \exp\left(-i\vec{p}.\vec{r}\right) . \tag{4.30}$$

which results in

$$\phi^S(\vec{p}) = \mathcal{N}\frac{64a^3C^4\pi}{(1+4C^2a^2p^2)^2} . \tag{4.31}$$

We can now use the BHL prescription to get the light-cone wavefunction,

$$\tilde{\phi}^{LC}(\boldsymbol{k}, z) = \mathcal{N}\frac{64C^4a^3\pi}{B^4}\frac{1}{(\beta^2+\boldsymbol{k}^2)^2} \quad ; \quad \beta^2 = \left(\frac{A}{B}\right)^2 , \tag{4.32}$$

where

$$A = 1 + \frac{C^2a^2m_f^2}{z(1-z)} - 4C^2a^2m_f^2 \tag{4.33}$$

and

$$B = \frac{C^2a^2}{z(1-z)} . \tag{4.34}$$

We still need to Fourier transform this light-cone wavefunction in configuration space so that we can use it within the colour dipole model. A two-dimensional Fourier transform to $d_\perp$ space gives

$$\phi^{LC}(d_\perp, z) = \frac{64\mathcal{N}C^4a^3}{2B^4}\int \frac{kdkJ_0(kd_\perp)}{(\beta^2+\boldsymbol{k}^2)^2} \tag{4.35}$$

where we have used the integral representation of the Bessel funtion. Using the identity (2.103), we can write

$$\int \frac{kJ_0(kd_\perp)dk}{(\beta^2+\boldsymbol{k}^2)} = \frac{r}{2\beta}K_1(d_\perp\beta)\ . \tag{4.36}$$

Therefore, the light-cone wavefunction in configuration space is

$$\phi^{LC}_{\text{Coulomb}}(d_\perp, z) = \mathcal{N}16C^4\frac{a^3}{AB^3}d_\perp K_1(d_\perp\beta)\ . \tag{4.37}$$

Recall that a is related to the strong coupling constant α_s via (4.29). We allow α_s to run according according to the following prescription [117]:

$$\alpha_s = \alpha \ \text{ for } \ d_\perp > d_\perp^s \quad \text{and} \quad \alpha_s(d_\perp) = \frac{4\pi}{\beta_0\log\left(1/\Lambda^2_{\text{QCD}}d_\perp^2\right)}\ . \tag{4.38}$$

where $d_\perp^s = 0.42$ fm, $\alpha_0 = 0.8$, $\Lambda_{\text{QCD}} = 0.2$ GeV and $\beta_0 = (33-2n_f)/3$, where n_f is the number of active flavours.

Now we find the wavefunction for the harmonic oscillator potential. The Schrödinger wavefunction in configuration space is

$$\phi^S(\vec{r}) = \mathcal{N}\exp\left(-\frac{|\vec{r}|^2R^2}{2}\right) \tag{4.39}$$

A three dimensional Fourier transformation to momentum space gives

$$\tilde{\phi}^S(\vec{k}) = \mathcal{N}(2\pi R^2)^{3/2}\exp\left(-\frac{k^2R^2}{2}\right)\ . \tag{4.40}$$

Applying the BHL prescription, we arrive at the following light-cone wavefunction:

$$\phi^{LC}(\boldsymbol{k}, z) = \mathcal{N}\exp\left[-R^2\left(\frac{\boldsymbol{k}^2+m_f^2}{8z(1-z)}\right)\right]\exp\left(\frac{m_f^2R^2}{2}\right)\ . \tag{4.41}$$

Finally a two-dimensional Fourier transform to $d_\perp$ space gives

$$\begin{aligned}\phi^{\text{LC}}_{\text{oscillator}}(d_\perp, z) \ &= \ \mathcal{N}\ 4z(1-z)\sqrt{2\pi R^2}\exp\left(-\tfrac{m^2R^2}{8z(1-z)}\right)\exp\left(-\tfrac{2z(1-z)d_\perp^2}{R^2}\right) \\ &\qquad \times\exp\left(\tfrac{m^2R^2}{2}\right)\ ,\end{aligned} \tag{4.42}$$

where a useful intermediate step in doing the above Fourier transform is

$$\int \exp\left[\frac{-R^2}{8z(1-z)}\left(k_j - \frac{i4z(1-z)j}{R^2}\right)^2\right] dk_j = \sqrt{\frac{\pi 8z(1-z)}{R^2}}\,, \tag{4.43}$$

with $j = x$ or y.

The sum of (4.37) and (4.42) is the light-cone wavefunction we shall use :

$$\phi^{\rm LC} = \phi^{\rm LC}_{\rm oscillator} + \phi^{\rm LC}_{\rm Coulomb} \tag{4.44}$$

Using (4.20), we can rewrite (4.17) as[9]

$$\Psi^{V,L}_{h,\bar{h}}(\boldsymbol{k}, z) = -\sqrt{\frac{N_c}{4\pi}}\delta_{h,-\bar{h}}\frac{1}{M_v z(1-z)}[m_f^2 + z(1-z)M_v^2 + \boldsymbol{k}^2]\tilde{\phi}(\boldsymbol{k}, z) \tag{4.45}$$

or equivalently in $d_\perp$ space,

$$\Psi^{V,L}_{h,\bar{h}}(\boldsymbol{d}_\perp, z) = -\sqrt{\frac{N_c}{4\pi}}\delta_{h,-\bar{h}}\frac{1}{M_v z(1-z)}[m_f^2 + z(1-z)M_v^2 - \partial^2_{d_\perp}]\phi(\boldsymbol{d}_\perp, z)\,. \tag{4.46}$$

where $\phi(\boldsymbol{d}_\perp, z)$ is the Fourier transform of $\tilde{\phi}(\boldsymbol{k}, z)$ given by (4.44).

In a similar way,[10] for the transverse case, we have

$$\Psi^{v,T(\gamma=+)}_{h,\bar{h}}(\boldsymbol{k}, z) = -\sqrt{\frac{N_c}{4\pi}}\frac{\sqrt{2}}{z(1-z)}[e^{i\theta_k}k(z\delta_{h+,\bar{h}-} - (1-z)\delta_{h-,\bar{h}+}) + m_f\delta_{h+,\bar{h}+}]\tilde{\phi}(\boldsymbol{k}, z) \tag{4.47}$$

and

$$\Psi^{v,T(\gamma=-)}_{h,\bar{h}}(\boldsymbol{k}, z) = -\sqrt{\frac{N_c}{4\pi}}\frac{\sqrt{2}}{z(1-z)}[e^{-i\theta_k}k((1-z)\delta_{h+,\bar{h}-} - z\delta_{h-,\bar{h}+}) + m_f\delta_{h-,\bar{h}-}]\tilde{\phi}(\boldsymbol{k}, z)\,. \tag{4.48}$$

After Fourier transformation to configuration space, the transverse meson light-cone wavefunctions become

$$\Psi^{v,T(\gamma=+)}_{h,\bar{h}}(\boldsymbol{d}_\perp, z) = \sqrt{\frac{N_c}{4\pi}}\frac{\sqrt{2}}{z(1-z)}[ie^{i\theta_{d_\perp}}(z\delta_{h+,\bar{h}-} - (1-z)\delta_{h-,\bar{h}+})\partial_{d_\perp} + m_f\delta_{h+,\bar{h}+}]\phi(\boldsymbol{d}_\perp, z) \tag{4.49}$$

and

$$\Psi^{v,T(\gamma=-)}_{h,\bar{h}}(\boldsymbol{d}_\perp, z) = \sqrt{\frac{N_c}{4\pi}}\frac{\sqrt{2}}{z(1-z)}[ie^{-i\theta_{d_\perp}}((1-z)\delta_{h+,\bar{h}-} - z\delta_{h-,\bar{h}+})\partial_{d_\perp} + m_f\delta_{h-,\bar{h}-}]\phi(\boldsymbol{d}_\perp, z) \tag{4.50}$$

[9] We extract a factor $\sqrt{\frac{N_c}{4\pi}}$ from the normalisation constant and drop the superscript (LC) on the scalar meson wavefunction ϕ from now on.

[10] For the transverse case, we do not have to worry about any "extra" term.

We fix the normalisation $\mathcal{N}$ using the normalisation condition (4.10). For the transverse case, (4.10) reads

$$1 = \frac{N_c}{2\pi}\int_0^1 \frac{dz}{z^2(1-z)^2}\int d^2\boldsymbol{d}_\perp \left\{m^2\phi^2(z,\boldsymbol{d}_\perp) + [z^2+(1-z)^2](\partial_{d_\perp}\phi(z,\boldsymbol{d}_\perp))^2\right\} \quad (4.51)$$

and for the longitudinal case,

$$1 = \frac{N_c}{2\pi}\int_0^1 \frac{dz}{M_v^2 z^2(1-z)^2}\int d^2\boldsymbol{d}_\perp\{[m_f^2 + z(1-z)M_v^2 - \partial_{d_\perp}^2]\phi(\boldsymbol{d}_\perp, z)\}^2 \quad (4.52)$$

where in both cases, we have summed over all quark and antiquark helicities. (4.51) and (4.52) being different, we find no *a priori* reason to assume the same normalisation constant for the longitudinal and transverse case. Nevertheless, for a given set of the free parameters R and C, it turns that the normalisation constant for the longitudinal case is not very different[11] from that for the transverse case. Thus, assuming the same normalisation constants for both cases as in [123, 118] can somewhat be justified but we find it more accurate not to do so.

4.4.3 CS choices for $\phi(\boldsymbol{k}, z)$

Caldwell and Soares [121] tried various analytic forms for $\phi(\boldsymbol{k}, z)$, starting with a simple delta function for the J/Ψ. The delta function restricts the $\boldsymbol{k}$ of the charm quark and antiquark to be zero and impose an equal sharing of longitudinal momentum, thus reflecting the assumed non-relativistic nature of the J/Ψ due to the heavy charm mass,

$$\phi^{J/\Psi}(\boldsymbol{k}, z) = \mathcal{N}\delta(z-1/2)\delta^2(\boldsymbol{k})\ , \quad (4.53)$$

The normalisation is fixed using the semi-leptonic decay width constraint (4.11). Though we expect this wavefunction to be somewhat unrealistic, CS found good agreement with the HERA data for the W dependence, though the normalisation is not correct in the photoproduction case. However the delta function wavefunction cannot describe the longitudinal to transverse ratio data. Allowing some transverse momentum $\boldsymbol{k}$ for the quarks, they used the Gaussian wavefunction proposed in [105],

[11] about 30% for the ρ case with $R^2 = 8.0\ \mathrm{GeV}^{-2}$ and $C = 0.25$. See Table 2.

$$\phi^{J/\Psi}(\boldsymbol{k}, z) = \mathcal{N}\delta(z - 1/2) \exp\left(-a\frac{\boldsymbol{k}^2}{m_c^2}\right) \,, \tag{4.54}$$

with $a = 4.68$ and the charm mass, $m_c = 1.43$ GeV, the normalisation being again obtained from the decay width constraint. The Gaussian wavefunction changes the normalisation allowing a better description of the W dependence of the total cross-section, in the photoproduction limit. However, the Gaussian wavefunction gives exactly the same prediction as the simple delta function for the ratio, $R = \sigma_L/\sigma_T$, thus failing to describe the data. Going a step further, CS used a double Gaussian function

$$\phi^{J/\Psi}(\boldsymbol{k}, z) = \mathcal{N} \exp[-c^2(z - 1/2)^2] \exp\left(-a\frac{\boldsymbol{k}^2}{m_c^2}\right) \,, \tag{4.55}$$

which changes the normalisation of the W dependence slightly as compared to the Gaussian wavefunction case but has the virtue of better describing the ratio data.

For the light mesons, ρ and ϕ, CS followed the relativistic approach of [118], but keeping only the harmonic oscillator term of the NNPZ wavefunction. They chose $R^2 = 15.5$ GeV^{-2} for the ρ and $R^2 = 8.0$ GeV^{-2} for the ϕ, taken from lattice calculations [121]. For ρ production, the normalisation for the Q^2 and W dependencies of the cross-section is not particularly well described while a good description of the ratio $R = \sigma_L/\sigma_T$ data is obtained. Similar conclusions hold for ϕ production. We highlight this inability to describe simultaneously the total cross-section and ratio data with the same set (only R here) of free parameters. As we shall see later, our own conclusions are similar.

4.4.4 DGKP wavefunctions

DGKP proposed the following ansatz for the light-cone meson wavefunction in $d_\perp$-space [59]

$$\Psi_v^L(\boldsymbol{d}_\perp, z) = z(1-z)\frac{\delta_{h,-\bar{h}}}{\sqrt{2}}\frac{\sqrt{2\pi}f_v}{\sqrt{N_c}e_f} f(z) e^{-\omega_L^2 d_\perp^2/2} \,, \tag{4.56}$$

$$\Psi_v^{T(\gamma=+)}(\boldsymbol{d}_\perp, z) = \left(\frac{i\omega^2 d_\perp e^{i\theta_{d_\perp}}}{M_v}[z\delta_{h+,\bar{h}-} - (1-z)\delta_{h-,\bar{h}+}] + \frac{m_f}{M_v}\delta_{h+,\bar{h}+}\right)\frac{\sqrt{2\pi}f_v}{\sqrt{N_c}e_f} f(z) e^{-\omega_T^2 d_\perp^2/2} \,, \tag{4.57}$$

$$\Psi_v^{T(\gamma=-)}(\boldsymbol{d}_\perp, z) = \left(\frac{i\omega^2 d_\perp e^{-i\theta_{d_\perp}}}{M_v} [(1-z)\delta_{h+,\bar{h}-} - z\delta_{h-,\bar{h}+}] + \frac{m_f}{M_v}\delta_{h+,\bar{h}+} \right) \frac{\sqrt{2}\pi f_v}{\sqrt{N_c} e_f} f(z) e^{-\omega_T^2 d_\perp^2/2} , \tag{4.58}$$

Notice that the $d_\perp$ dependence is simply Gaussian and that the DGKP wavefunction is factorised into a $d_\perp$ and z dependent functions which explicitly violates the Halperin-Zhitnisky theoretical constraint (see Section 4.4). Nevertheless, since the end-points contributions are suppressed, this has no practical consequence [122]. The function $f(z)$ is that proposed by Wirbel, Stech and Bauer [120],

$$f_\lambda(z) = \mathcal{N}_\lambda \sqrt{z(1-z)} e^{-M_v^2(z-1/2)^2/2\omega_\lambda^2} \quad ; \quad \lambda = T \text{ or } L . \tag{4.59}$$

The parameters $\mathcal{N}_\lambda$ and ω_λ are fixed using the leptonic decay width constraint (4.11) and the normalisation condition (4.10). Squaring (4.56) and summing over all quark and antiquark helicities, we have

$$\sum_{h,\bar{h}} \Psi_{h,\bar{h}}^{L*} \Psi_{h,\bar{h}}^{L} = |\Psi_v^L|^2 = \frac{2\pi^2 f_v^2}{N_c e_f^2} z^2(1-z)^2 f_L^2(z) \exp(-\omega_L^2 d_\perp^2) . \tag{4.60}$$

Similarly squaring either (4.57) or (4.58), and summing over all quark and antiquark helicities, we find

$$\sum_{h,\bar{h}} \Psi_{h,\bar{h}}^{T} \Psi_{h,\bar{h}}^{T} = |\Psi_v^T|^2 = \frac{2\pi^2 f_v^2}{N_c e_f^2} \frac{\omega_T^4 d_\perp^2}{M_v} \left[z^2 + (1-z)^2 + \frac{m_f^2}{M_v^2} \right] f_T(z)^2 \exp(-\omega_T^2 d_\perp^2) . \tag{4.61}$$

Plugging the above expressions in the normalisation condition (4.10) and doing the trivial Gaussian integration over $d_\perp$, we arrive at the following normalisation conditions on the longitudinal and tranverse DGKP meson light-cone wavefunctions (see also [59])[12]

$$\omega_\lambda = \frac{\sqrt{2}\pi^{3/2} f_v}{\sqrt{N_c} e_f} \sqrt{I_\lambda} , \tag{4.62}$$

with

$$I_L = \int_0^1 dz z^2 (1-z)^2 f_L^2(z) , \tag{4.63}$$

and

$$I_T = \int_0^1 dz \frac{[z^2 + (1-z)^2]\omega_T^2 + m_f^2}{M_v^2} f_T^2(z) , \tag{4.64}$$

[12]our normalisation conditions differ from that of [59] by a factor of $1/4\pi$.

which allows us to calculate the normalisation $\mathcal{N}_{L,T}$ given $\omega_{L,T}$. Thus we have a different set of values of $\{\mathcal{N},\omega\}$ for the longitudinal and transverse case. In what follows, we shall use the values for $\omega_{L,T}$ given in [59] to calculate the normalisation using (4.62). We shall not adjust any parameters to fit the data.

4.5 Comparison between the NNPZ and the DGKP wavefunctions

The obvious common feature of the NNPZ and DGKP models is the Gaussian dependence on the transverse $d_\perp$. The helicity structure of both wavefunctions follow that of the photon light-cone wavefunction. While the specific z-dependence is different, the end-point contributions are suppressed in both cases. Both the NNPZ and DGKP wavefunctions are subject to the normalisation condition (4.10) and the semi-leptonic decay width constraint (4.11).

We find the NNPZ model theoretically more sophisticated for two main reasons. First, the wavefunction is modified by a Coulomb term which enhances the wavefunction as the transverse size $d_\perp$ goes to zero, this feature being absent in the DGKP model. Secondly, the NNPZ wavefunction is rigorously derived in analogy with the photon light-cone wavefunction and includes additional terms like the double derivative of the spatial part of the meson wavefunction in the longitudinal case, which are absent in the DGKP model. We can also add that the NNPZ cannot be factorised into the form $\phi(d_\perp)\xi(z)$ while the DGKP wavefunction is explicitly written in this form, thus violating the Halperin-Zhitnitsky constraint.

On the other hand, we find no a priori reason to assume the same set of free parameters for the longitudinal and transverse light-cone wavefunctions. In the DGKP model, different values of the free parameters are chosen for the longitudinal and transverse wavefunctions while NNPZ assume the same set of values for both cases.

Nevertheless, we shall use the NNPZ and DGKP in their original formulation but we shall remove the semi-leptonic decay width constraint on the NNPZ wavefunction, tuning the parameters R and C in order to fit the data with the FKS dipole cross-section. We leave possible modifications of the DGKP and NNPZ models for a future analysis.

The modulus square (summed over all quark and antiquark helicities) of the NNPZ and DGKP wavefunctions for the ρ meson, are shown in Figure 4.5 and 4.6.

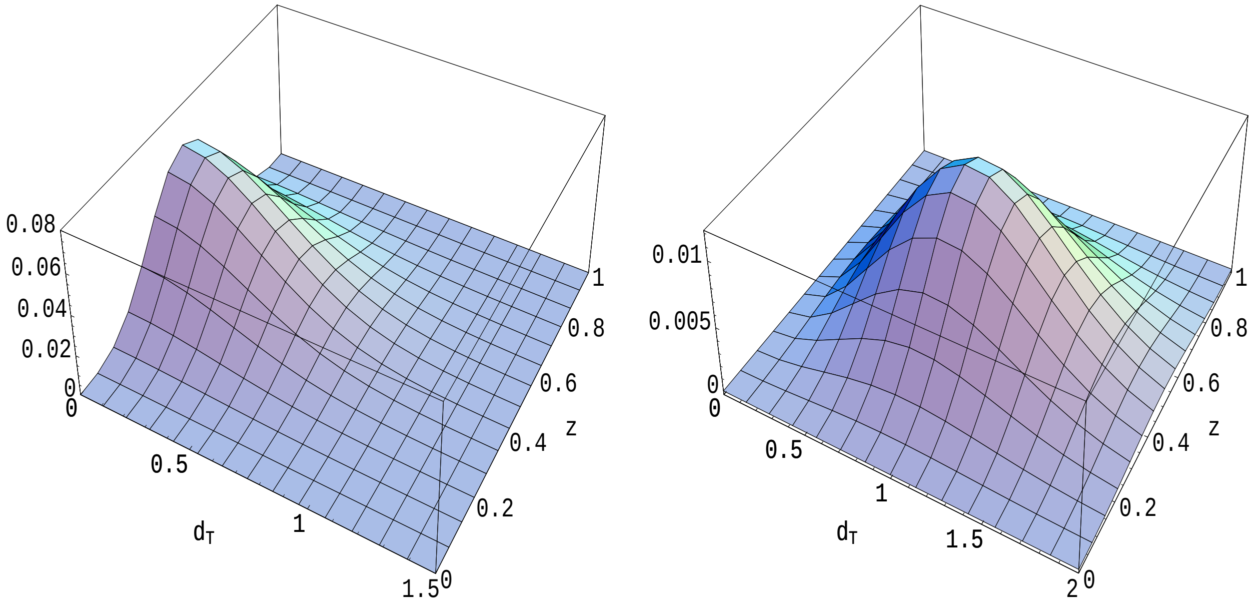

Figure 4.5: The modulus square of the DGKP wavefunctions. Left: $|\Psi_v^L|^2$ in units of GeV^2 with $\omega_L = 0.330$ GeV. Right: $|\Psi_v^T|^2$ in units of GeV^2, $\omega_T = 0.219$ GeV. End points contributions, $z \sim 0$ or 1 are suppressed in both the longitudinal and transverse cases. The transverse wavefunction extends more to larger $d_\perp$ and vanishes as $d_\perp \to 0$.

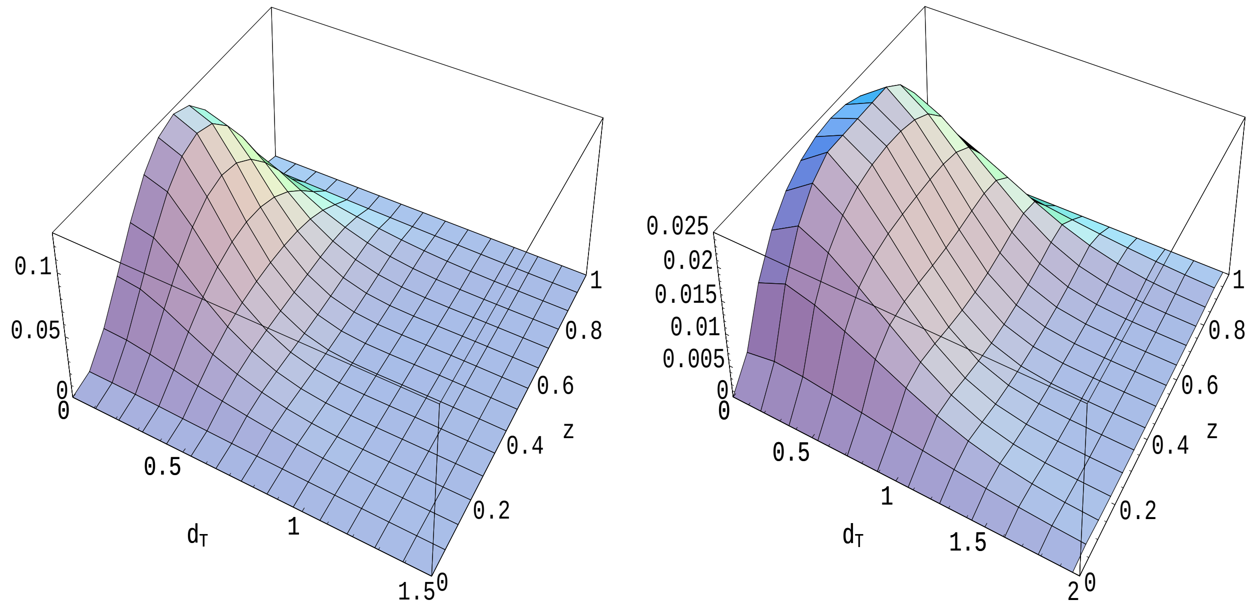

Figure 4.6: The modulus square of the NNPZ wavefunction with $R = 8.0$ GeV^2 and $C = 0.25$. Left: $|\Psi_v^L|^2$ in units of GeV^2. Right: $|\Psi_v^T|^2$ in units of GeV^2. End points contributions, $z \sim 0$ or 1 are suppressed in both the longitudinal and transverse cases. The transverse wavefunction extends more to larger $d_\perp$ and does not vanish as $d_\perp \to 0$, except at the end-points of z.

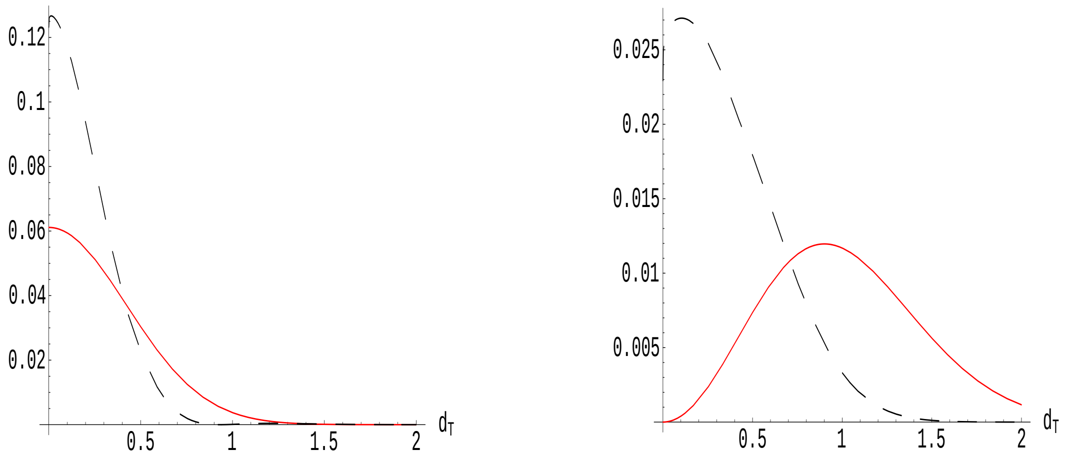

Figure 4.7: The DGKP (solid line) and NNPZ (dashed curve) wavefunctions for the ρ meson at fixed, $z = 0.5$. Left: Longitudinal wavefunctions. Right: Transverse wavefunctions.

4.6 Longitudinal and transverse amplitudes

4.6.1 NNPZ amplitudes

Having constructed the meson light-cone wavefunction, it is now straightforward to calculate the longitudinal and transverse amplitudes for vector meson production using (4.6). Using the NNPZ wavefunction, we find

$$\begin{aligned}\mathcal{A}^L = \tfrac{N_c e_f \sqrt{4\pi\alpha_{e.m}}}{(2\pi)^2}\tfrac{2Q}{M_v}\int d^2\boldsymbol{d}_\perp \hat{\sigma}\int dz\{[m_f^2 + z(1-z)M_v^2]K_0(\epsilon d_\perp)\phi_v(d_\perp, z) \\ +K_0(\epsilon d_\perp)\partial^2_{d_\perp}\phi_v(z, d_\perp)\}\ .\end{aligned} \tag{4.65}$$

for the longitudinal amplitude and

$$\begin{aligned}\mathcal{A}^T = \tfrac{N_c e_f \sqrt{4\pi\alpha_{e.m}}}{(2\pi)^2}\int d^2\boldsymbol{d}_\perp \hat{\sigma}\int_0^1 dz[z^2 + (1-z)^2]\partial_{d_\perp}K_0(\epsilon d_\perp)\partial_{d_\perp}\phi_v(d_\perp, z) \\ +m_f^2 K_0(\epsilon d_\perp)\phi_v(z, d_\perp)\ .\end{aligned} \tag{4.66}$$

for the transverse amplitude. (4.66) is exactly the formulae given in [118]. The only difference in (4.65) is that the term $K_0(\epsilon d_\perp)\partial^2_{d_\perp}\phi(z, d_\perp)$ is integrated by parts and the surface term neglected. Strictly speaking, this is justified only if the dipole cross-section is slowly varying with $d_\perp$, which excludes the case of high Q^2 when the small $d_\perp$ region is probed and the dipole cross-section has a quadratic dependence on $d_\perp$. This mistake was pointed out and corrected by the same authors in [119] which we follow here. As also argued in [119], this term (proportional to $\boldsymbol{k}^2$ in momentum space), is a relativistic correction for the case of heavy quarkonium like the J/Ψ and for the light mesons at high Q^2. We confirm this statement in our calculation which also means a consistency check of our own calculation. In Figure 4.8, we show the effect of removing the relativistic correction term in the longitudinal amplitude. In the transverse amplitude, we can also identify the term proportional to the derivative of the meson wavefunction (or proportional to $\boldsymbol{k}$ in momentum space) as a relativistic correction. This time, we find that removing this term makes a significant difference as shown in Figure 4.9. Note that this crucially depends on the parameter R we choose for a particular meson, which controls the exponential suppression of high $\boldsymbol{k}$ in the meson wavefunction, hence in the production amplitude. We show here the effect of relativistic corrections for the values of R we shall use to fit the data as we shall see in the next Section. To keep our calculation completely general, we use (4.65) and (4.66) for all three vector mesons. As argued in [117], a simple evaluation of the

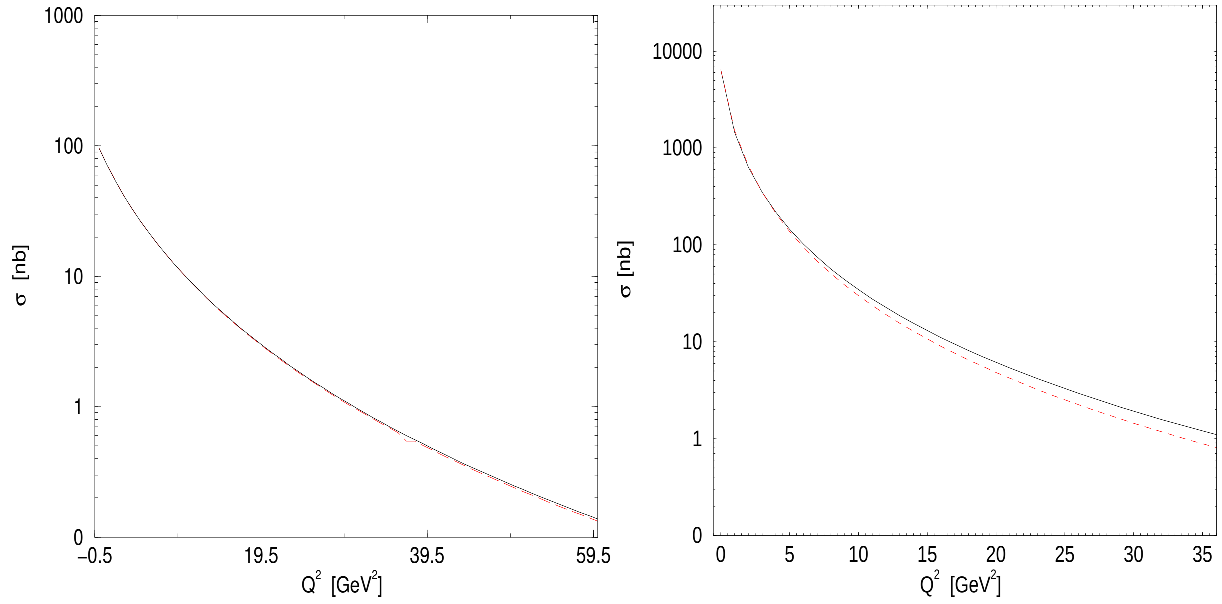

Figure 4.8: Left: The effect of the relativistic correction term ($\propto \partial^2_{d_\perp}\phi(z, d_\perp)$) in the longitudinal amplitude in J/Ψ production with $W = 90$ GeV, $R = 4.0$ GeV^{-2} and $C = 0.5$. Right: The effect of the relativistic correction term in the longitudinal amplitude in ρ production with $W = 75$, $R = 8.0$ GeV^{-2} and $C = 0.5$ GeV. We can clearly see that the relativistic correction is negligible for the J/Ψ while it is negligible for low Q^2 for the ρ. The dashed line is produced by removing the relativistic term. Here σ is the total cross-section for J/Ψ or ρ production.

imaginary amplitudes (4.65) and (4.66) at the value of the scanning radius, with the further assumption $z \approx 1/2$, gives

$$\mathcal{A}^T \propto d_\perp^{s2}\hat{\sigma}(d_\perp^s, W^2) \propto \frac{1}{(Q^2+M_v^2)^2} \, , \tag{4.67}$$

$$\mathcal{A}^L \propto \frac{Q}{M_v} d_\perp^{s2}\sigma(d_\perp^s, W^2) \propto \frac{Q}{M_v(Q^2+M_v^2)^2} \, . \tag{4.68}$$

This means that the longitudinal to transverse cross-section ratio, R is given by

$$R = \frac{\sigma_L}{\sigma_T} \approx \frac{Q^2}{M_v^2} \, . \tag{4.69}$$

indicating that the longitudinal cross-section dominates over the transverse cross-section as Q^2 increases. This feature is shared by all models of diffractive meson leptoproduction [117]. Nevertheless, the linear rise of R with Q^2 as suggested by is *not* supported by the data as can be clearly seen in Figure 4.3.

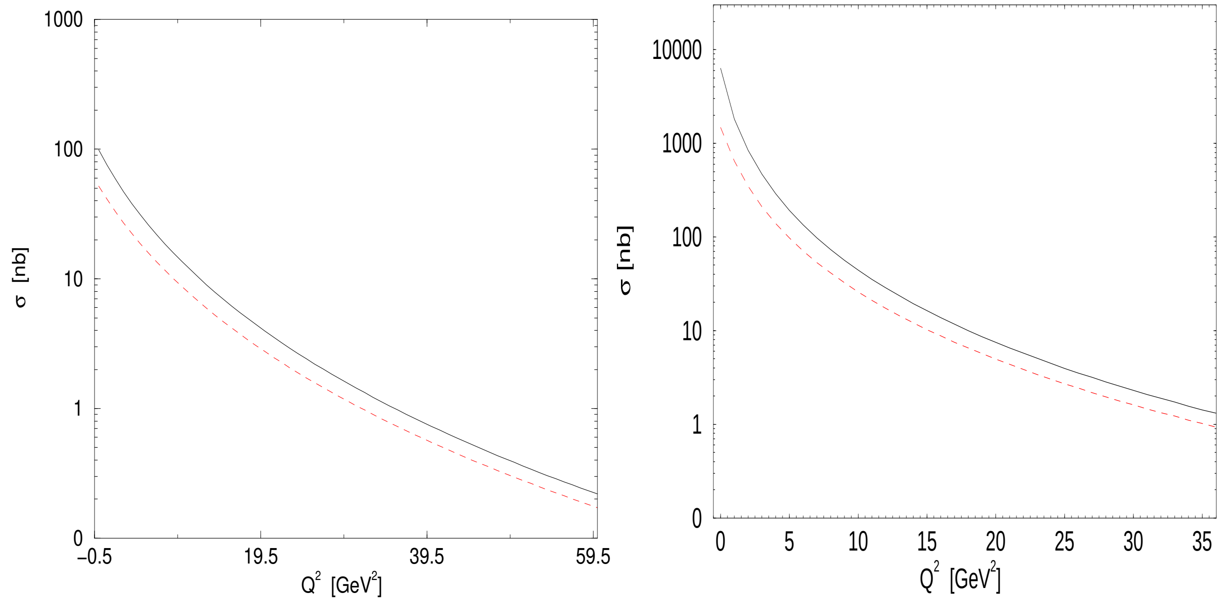

Figure 4.9: Left : The effect of the relativistic correction term ($\propto \partial_{d_\perp}\phi(z, d_\perp)$) in the transverse amplitude in J/Ψ production. $W = 90$ GeV, $R = 4.0$ GeV^{-2} and $C = 0.5$. Right: The effect of the relativistic correction term in the transverse amplitude in ρ production. $W = 75$, $R = 8.0$ GeV^{-2} and $C = 0.5$ GeV. We see that the relativistic correction is significant in both cases; the dashed line is produced by removing the relativistic term. Here σ is the total cross-section for J/Ψ or ρ production.

4.6.2 DGKP amplitudes

Using the DGKP light-cone meson wavefunction, we find that the longitudinal amplitude is given by

$$\mathcal{A}^L = \int d^2\boldsymbol{d}_\perp \hat{\sigma} \int dz \sqrt{\alpha_{e.m}} f_v z(1-z) f(z) e^{-\omega^2 d_\perp^2/2} 2z(1-z) Q K_0(\epsilon d_\perp) \;, \tag{4.70}$$

and for the transverse amplitude,

$$\mathcal{A}^T = \int d^2\boldsymbol{d}_\perp \hat{\sigma} \int dz \sqrt{\alpha_{e.m}} f_v f(z) e^{-\omega^2 d_\perp^2/2} \left(\frac{\omega^2 \epsilon d_\perp}{M_v} [z^2 + (1-z)^2] K_1(\epsilon d_\perp) + \frac{m_f^2}{M_v} K_0(\epsilon d_\perp) \right) . \tag{4.71}$$

4.6.3 The total cross-section

As for the case of DVCS, we first calculate the forward differential cross-section and divide by the diffractive slope to find the total cross-section,

$$\sigma(\gamma^* p \to V p) = \frac{d\sigma/dt|_{t=0}}{B} \;. \tag{4.72}$$

Here, we use a parametrisation for B given in [121],

$$B = 0.60 \left(\frac{14}{(Q^2 + M_v^2)^{0.26}} + 1 \right) . \tag{4.73}$$

4.7 Results

Having set up the theoretical framework, we are now ready to make numerical predictions and compare with experimental data. A few comments are in order before proceeding.

First, we must decide which quark mass we shall use, given that the different dipole models and meson wavefunctions models propose different values for the quark mass. The FKS dipole model uses the set[13] $\{m_{u,d,s} = \sqrt{0.08}, m_c = \sqrt{1.4}\}$, GW dipole model, $\{m_{u,d,s} = 0.14, m_c = 1.43\}$, the NNPZ model, $\{m_{u,d} = 0.15, m_s = 0.30, m_c = 1.30\}$ while DGKP model uses $\{m_{u,d} = 0.0, m_s = 0.14, m_c = 1.43\}$. For consistency, we shall choose a particular set and use it for both the meson and photon light-cone wavefunction (and in the dipole cross-section in the case of the GW dipole). When using the NNPZ wavefunction, we shall use the FKS set of quark masses and when using the DGKP wavefunction, we shall use the DGKP set. We note that using the DGKP set of quark masses with the FKS dipole, is not strictly correct since the parameters of the FKS dipole are fitted with the FKS set of quark masses (and the enhancement factor for the photon light-cone wavefunction).

Second, as already mentioned earlier, we shall treat the parameters R and C of the NNPZ wavefunction as free and tune them to fit the data, using the FKS dipole cross-section. This is because we are unable to fit the total cross-section data using the original set of parameters in the NNPZ wavefunction as determined in [117].[14] With the chosen set of R and C, we make a few predictions (for comparison purposes) with the GW dipole model. However, we shall only focus on and discuss the FKS predictions. When using the DGKP wavefunction, we use the parameters ω_L and ω_T as given in [59]. We summarise the parameters and normalisations of the DGKP and

[13] in units of GeV.

[14] These parameters are checked to be consistent with the semi-leptonic decay width constraint [117].

NNPZ wavefunctions in Table 4.1

NNPZ	R^2	C	$\mathcal{N}_L$	$\mathcal{N}_T$
ρ	8.0	0.25	0.035	0.027
ϕ	6.0	0.8	0.016	0.014
J/Ψ	2.0	0.9	0.026	0.024
DGKP	ω_L	ω_T	$\mathcal{N}_L$	$\mathcal{N}_T$
ρ	0.330	0.219	4.238	3.231
ϕ	0.365	0.270	4.396	3.207
J/Ψ	0.680	0.580	5.360	2.569

Table 4.1: Parameters and normalisations of the longitudinal and transverse NNPZ and DGKP light-cone wavefunction for the three different mesons, in appropriate GeV based units throughout.

4.7.1 ρ production

Our results using the NNPZ wavefunction for the W and Q^2 dependence of the total cross-section and the ratio, $R = \sigma_L/\sigma_T$ as a function of Q^2 are shown in Figures 4.10, 4.11 and 4.12. Note that we have adjusted the free parameters R and C of the NNPZ wavefunction in order to fit the Q^2 dependence of the total cross-section, giving $R^2 = 8.0\ \mathrm{GeV}^{-2}$ and $C = 0.25$. We then use these same values to predict the W dependence of the total cross-section and the ratio data. In addition, for comparison, we show the predictions of the GW dipole model, using the same set of free parameters. In adjusting the values of R and C in order to fit the Q^2 and W dependence of the total cross-section, we are unable to fit the ratio data. Conversely, in adjusting the free parameters to fit the ratio data, we are unable to fit the Q^2 and W dependence of the total cross-section. In conclusion, *we cannot describe simultaneously the Q^2 (W) dependence of the total cross-section and the ratio $R = \sigma_L/\sigma_T$, with the same set of free parameters.*

Our predictions using the DGKP wavefunction are shown in Figures 4.13, 4.14 and 4.15. The total cross-section data for the light mesons is not well described particularly in the photoproduction limit. We find a faster increase of the longitudinal to transverse cross-section ratio with increasing Q^2, giving a better description of the (few) data points at low Q^2. However, since the error bars on most of the ratio data points are large, we *cannot* conclude that the DGKP gives an better overall description of the ratio data compared to the NNPZ wavefunction. Recall that no fitting procedure is applied in the DGKP case; we simply use the parameters of the DGKP wavefunction as determined in the original formulation of the model [59].

Comparing the NNPZ and the DGKP predictions, we can see in Figures 4.13 and Figure 4.10 that the DGKP curve overshoots the photoproduction data point while the NNPZ curve does not reach it. We also notice in Figures 4.14 and 4.11 that the DGKP curve is above the NNPZ curve at the lowest Q^2 value, $Q^2 = 0.47$ GeV^2. We understand this as follows : First, recall that in the photoproduction limit, only the transverse amplitude contributes. Looking back at Figure 4.7, we see that the DGKP transverse wavefunction extends more to larger $d_\perp$ than the NNPZ wavefunction which means that in the photoproduction (or low Q^2) limit, the DGKP wavefunction will give a higher cross-section.

We find that the GW dipole model gives similar predictions as the FKS dipole model when using the NNPZ wavefunction.

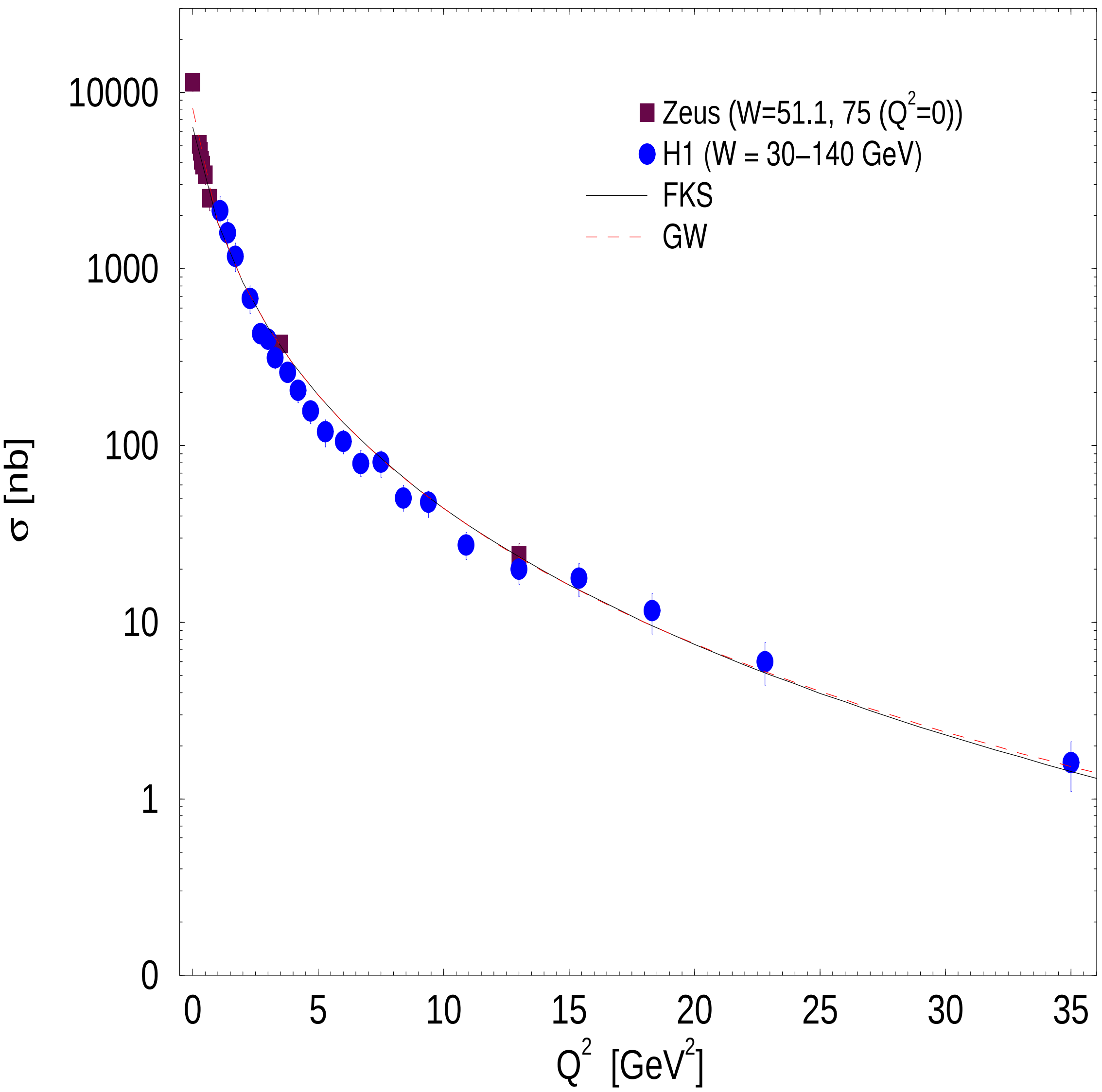

Figure 4.10: The Q^2 dependence of the total cross-section for ρ production in the FKS (solid line) and GW (dashed line) dipole models, at $W = 75$ GeV. The free parameters of the NNPZ wavefunction are set to $R^2 = 8.0$ GeV^{-2} and $C = 0.25$.

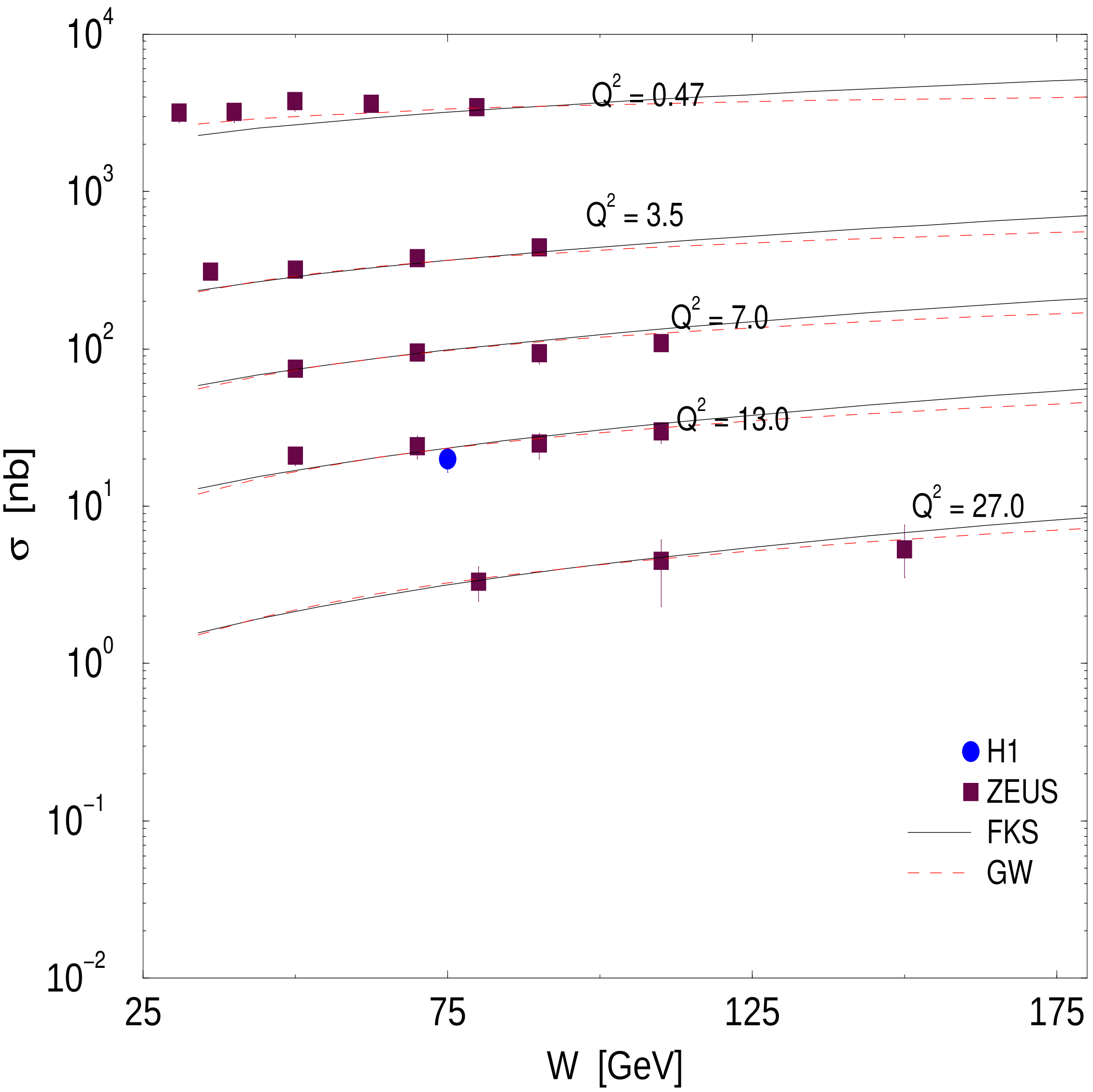

Figure 4.11: The energy dependence of the total cross-section for ρ production in the FKS (solid line) and GW (dashed line) dipole models, at various Q^2 values. The free parameters of the NNPZ wavefunction are set to $R^2 = 8.0\ \mathrm{GeV}^{-2}$ and $C = 0.25$. Data from [132].

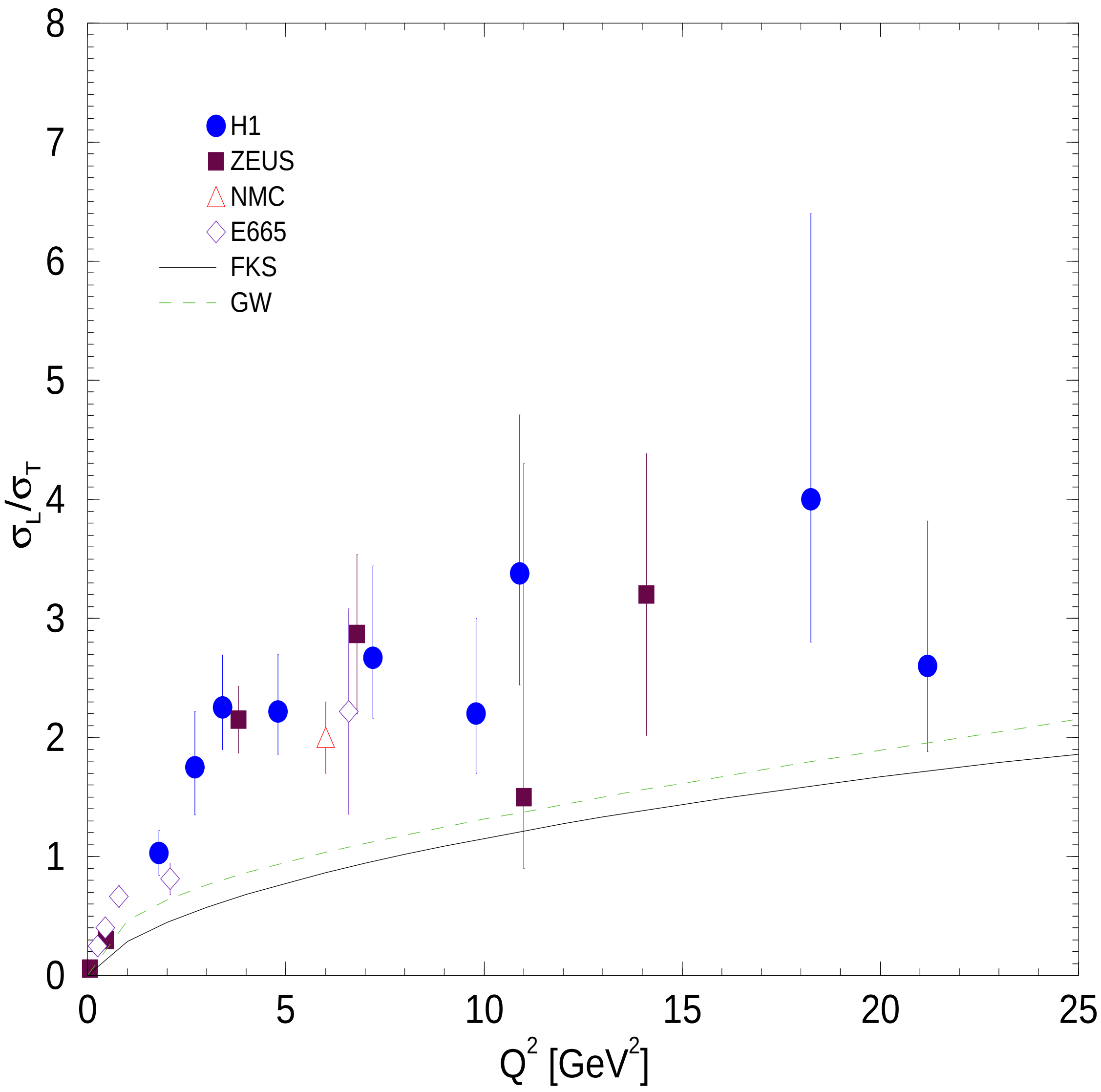

Figure 4.12: The Q^2 dependence of the longitudinal to transverse ratio σ_L/σ_T in the FKS (solid line) and GW (dashed line) dipole models. The free parameters of the NNPZ wavefunction are set to $R^2 = 8.0$ GeV^{-2} and $C = 0.25$. We clearly predict a slower dominance of the longitudinal cross-section over the transverse cross-section than that suggested by the data. Data from [131, 133, 135, 134].

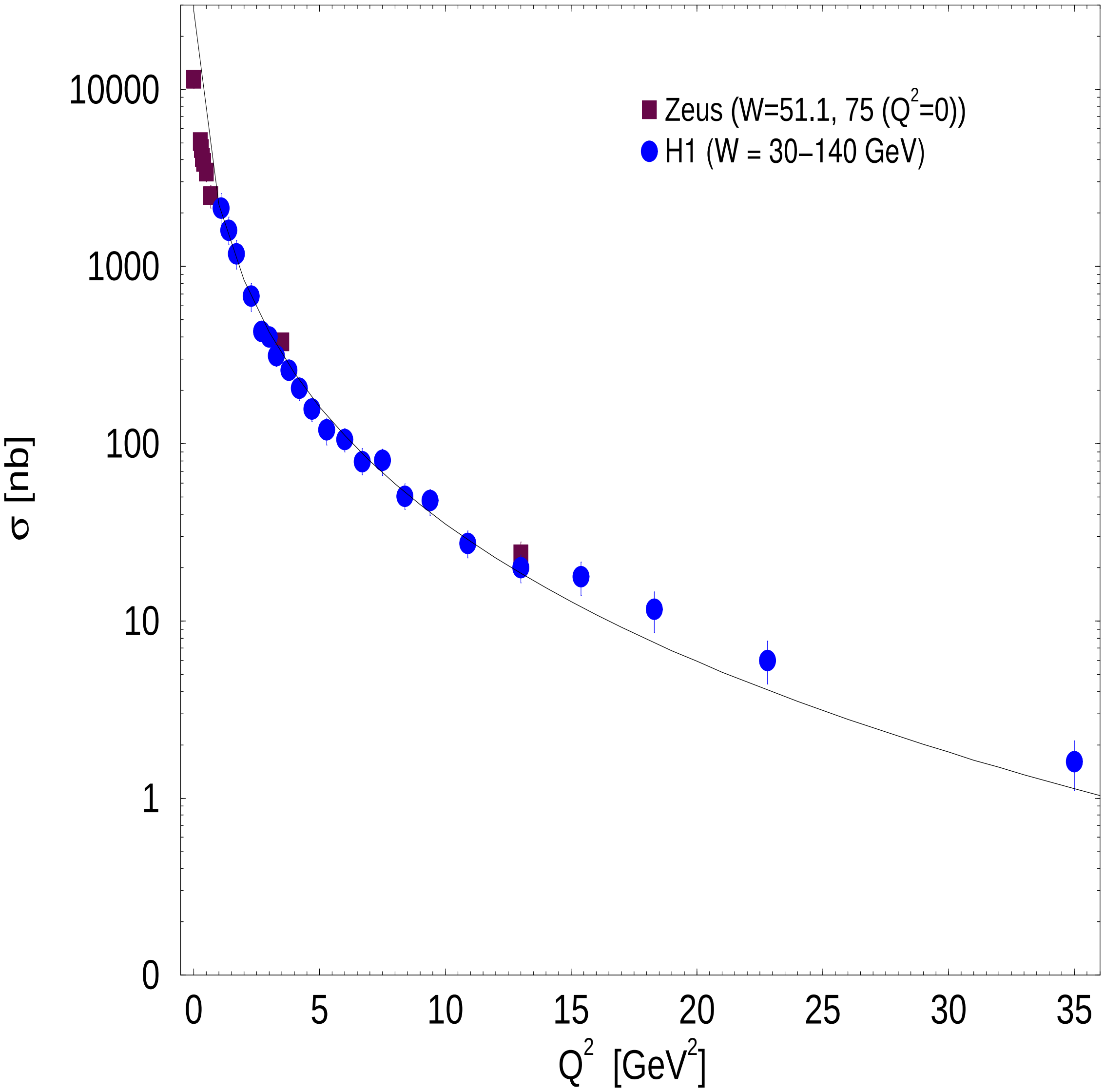

Figure 4.13: The Q^2 dependence of the total cross-section for ρ production in the FKS model with the DGKP wavefunction, at $W = 75$ GeV, using the DGKP wavefunction. Data from [131, 132].

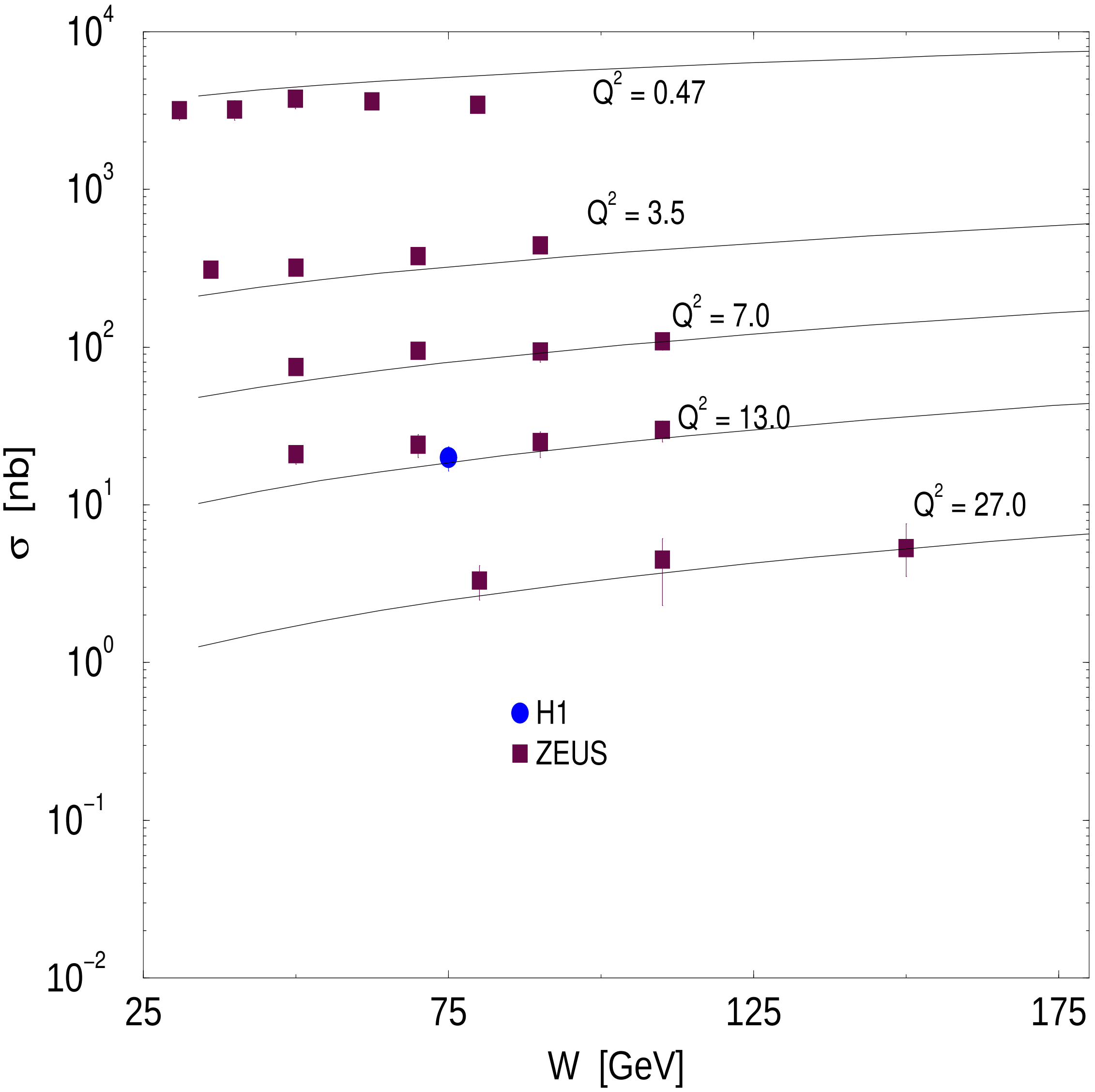

Figure 4.14: The energy dependence of the total cross-section for ρ production in the FKS model with the DGKP wavefunction, for different Q^2 values. Data from [132].

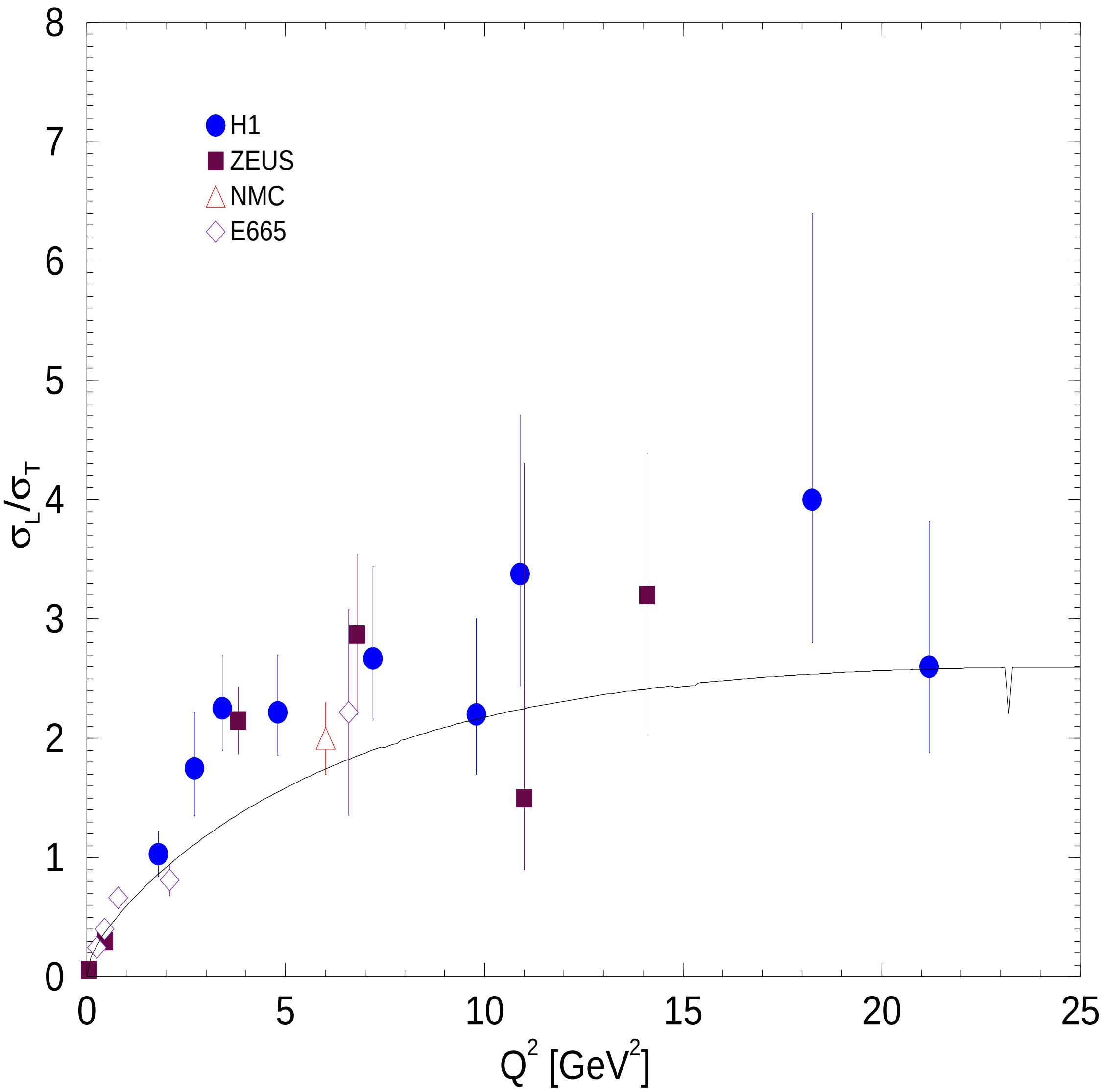

Figure 4.15: The longitudinal to transverse cross-section ratio, $R = \sigma_L/\sigma_T$, for ρ production in the FKS model with the DGKP wavefunction, at $W = 75$ GeV. Data from [131, 133, 135, 134].

4.7.2 ϕ production

In the NNPZ model, using $R^2 = 6.0$ GeV^{-2} and $C = 0.8$, we obtain a reasonable fit for the Q^2 dependence of the total cross-section as shown in Figure 4.16. Our prediction for the W dependence of the total cross-section is consistent with the few published data, see Figure 4.17. On the other hand, as shown in Figure 4.18, we predict a too slow rise of the ratio, $R = \sigma_L/\sigma_T$ compared to that suggested by the data. Our conclusion is therefore same as for the ρ: we are unable to fit simultaneously the total cross-section and the ratio data with the same set of free parameters of the NNPZ wavefunction. However note that fewer data is available for the ϕ; so we favour this conclusion with less confidence than for the ρ case.

Our predictions with the DGKP wavefunction are shown in Figures 4.19, 4.20 and 4.21. As for the ρ, the total cross-section is not well described particularly in the photoproduction limit. The DGKP wavefunction predicts a faster rise of the longitudinal to transverse cross-section ratio as compared to the NNPZ wavefunction. However, because of the few data points with large error bars, we do not conclude that the DGKP wavefunction gives a better description of the ratio data.

Again as in the ρ case, comparing Figures 4.16 and 4.19, we find the DGKP curves to exceed the NNPZ curve in the photoproduction limit. We favour the same argument as in the ρ case to explain this observation although we have not compared explicity the DGKP and NNPZ ϕ wavefunction as we did for the ρ case.

We notice that the GW dipole model cannot describe the data with these particular values for the free parameters in the NNPZ wavefunction.

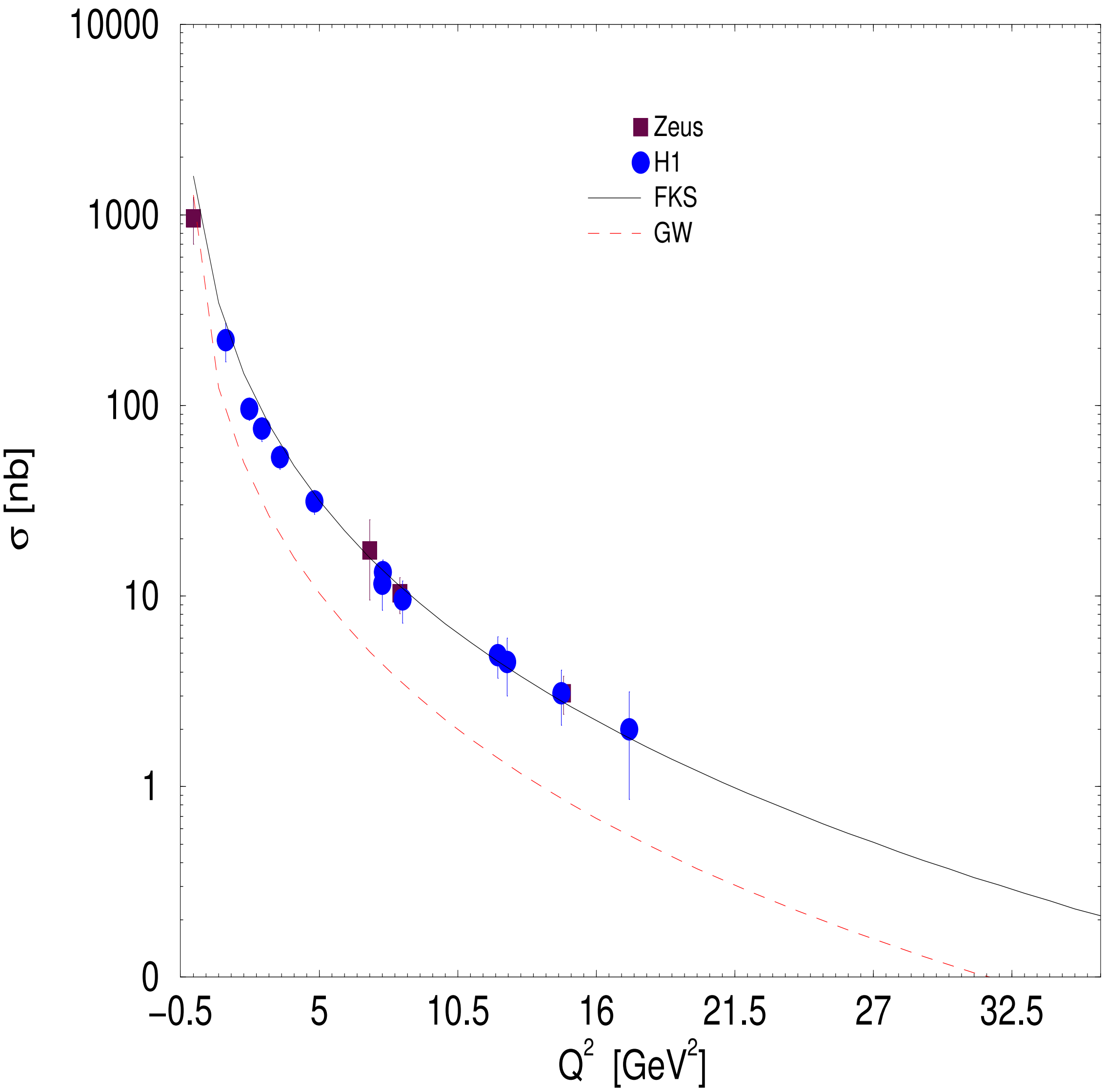

Figure 4.16: The Q^2 dependence of the total cross-section for ϕ production in the FKS (solid line) and GW (dashed line) dipole model. The free parameters of the NNPZ wavefunction are set to $R^2 = 6.0\ \mathrm{GeV}^{-2}$ and $C = 0.8$. Data from [136, 137, 138, 139].

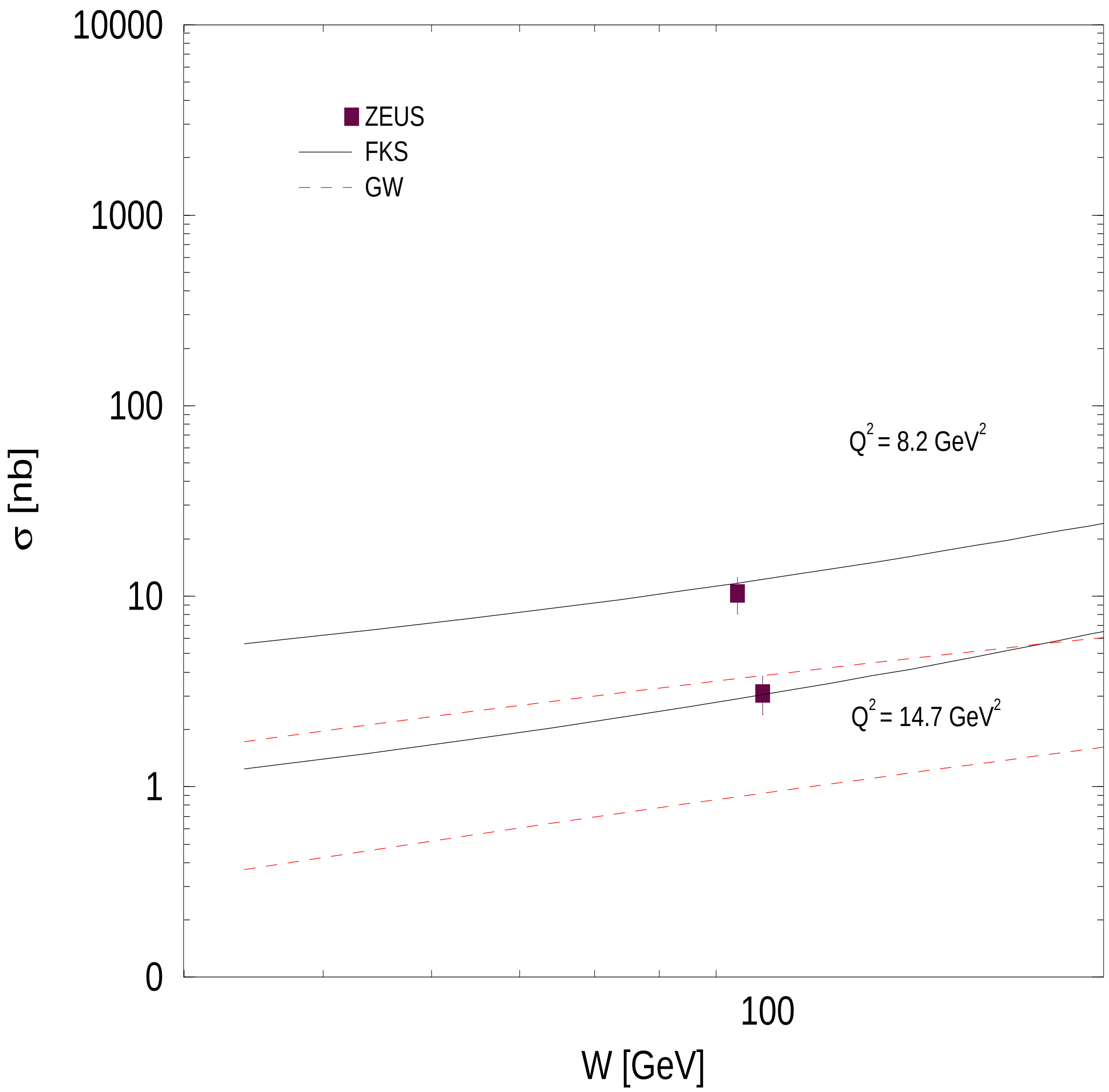

Figure 4.17: The energy dependence of the total cross-section for ϕ production in the FKS (solid line) and GW (dashed line) dipole model, at $W = 90$ GeV. The free parameters of the NNPZ wavefunction are set to $R^2 = 6.0\ \mathrm{GeV}^{-2}$ and $C = 0.8$. Data from [141].

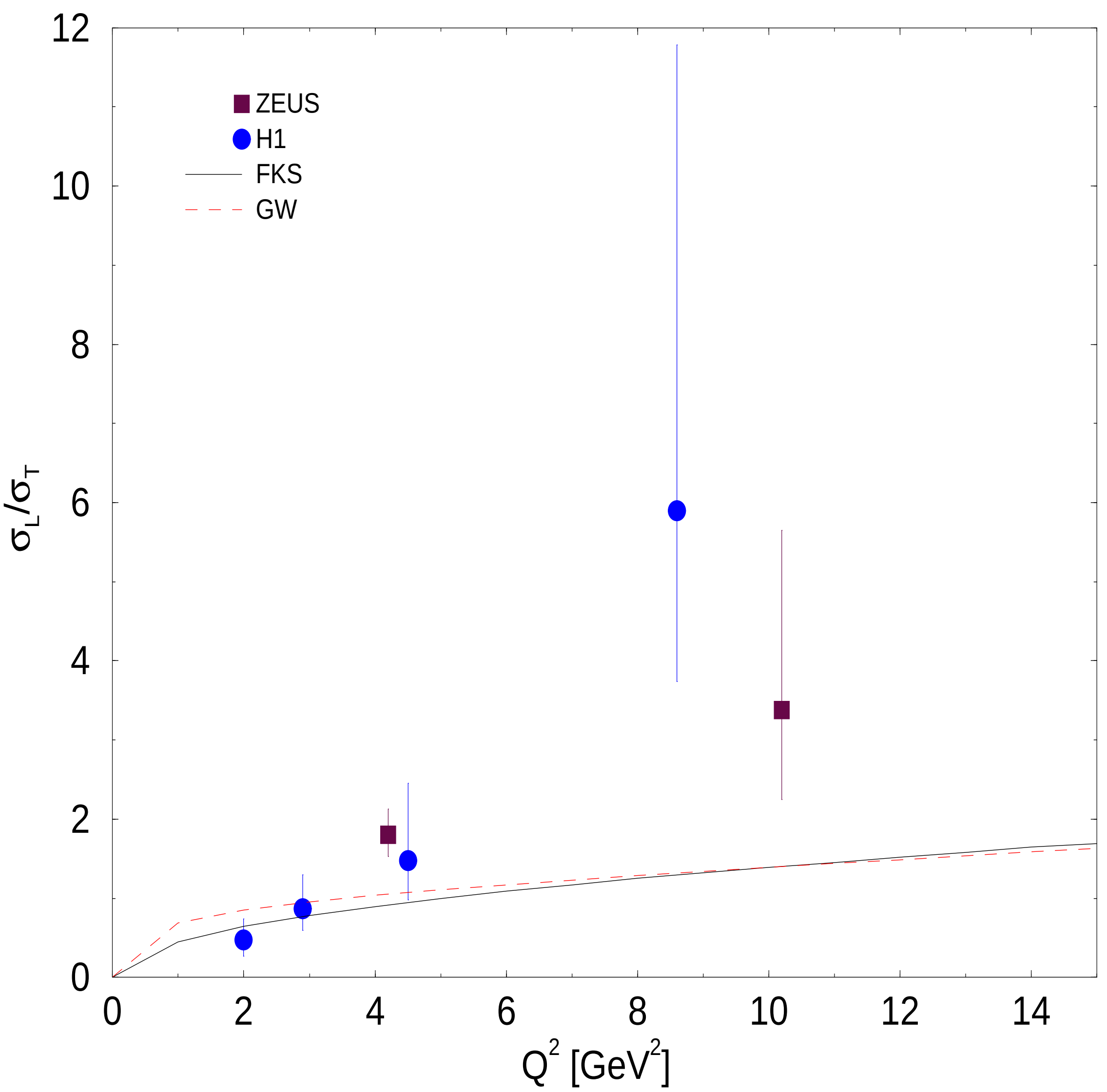

Figure 4.18: The Q^2 dependence of the longitudinal to transverse ratio σ_L/σ_T for ϕ production in the FKS (solid line) and GW (dashed line) dipole model, at $W = 90$ GeV. The free parameters of the NNPZ wavefunction are set to $R^2 = 6.0$ GeV^{-2} and $C = 0.8$. We predict a too slow dominance of the longitudinal cross-section over the transverse cross-section than that suggested by the data. Data from [136, 140].

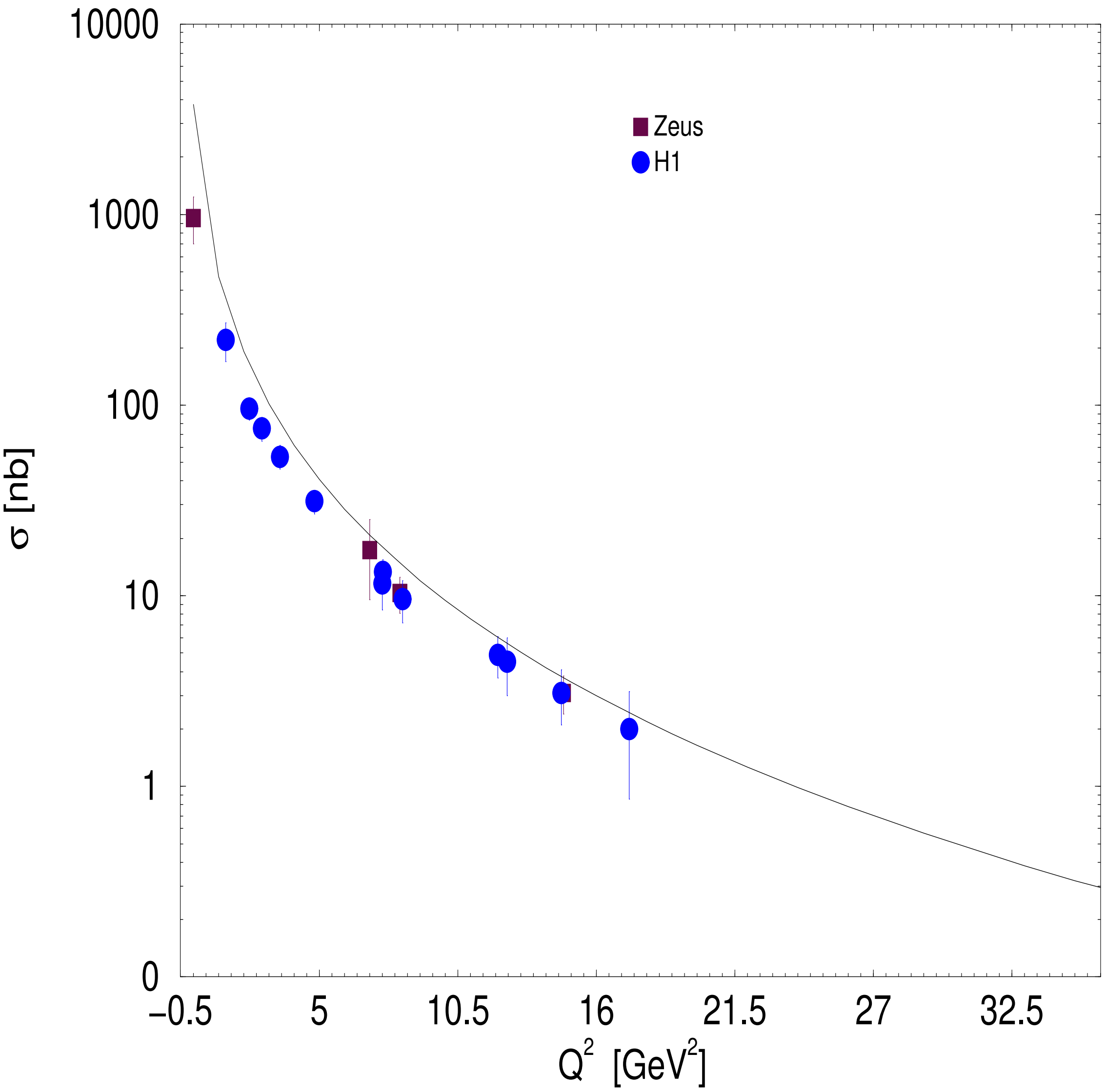

Figure 4.19: The Q^2-dependence of the total cross-section for ϕ production in the FKS model at $W = 90$ GeV, using the DGKP wavefunction. Data from [136, 137, 138, 139].

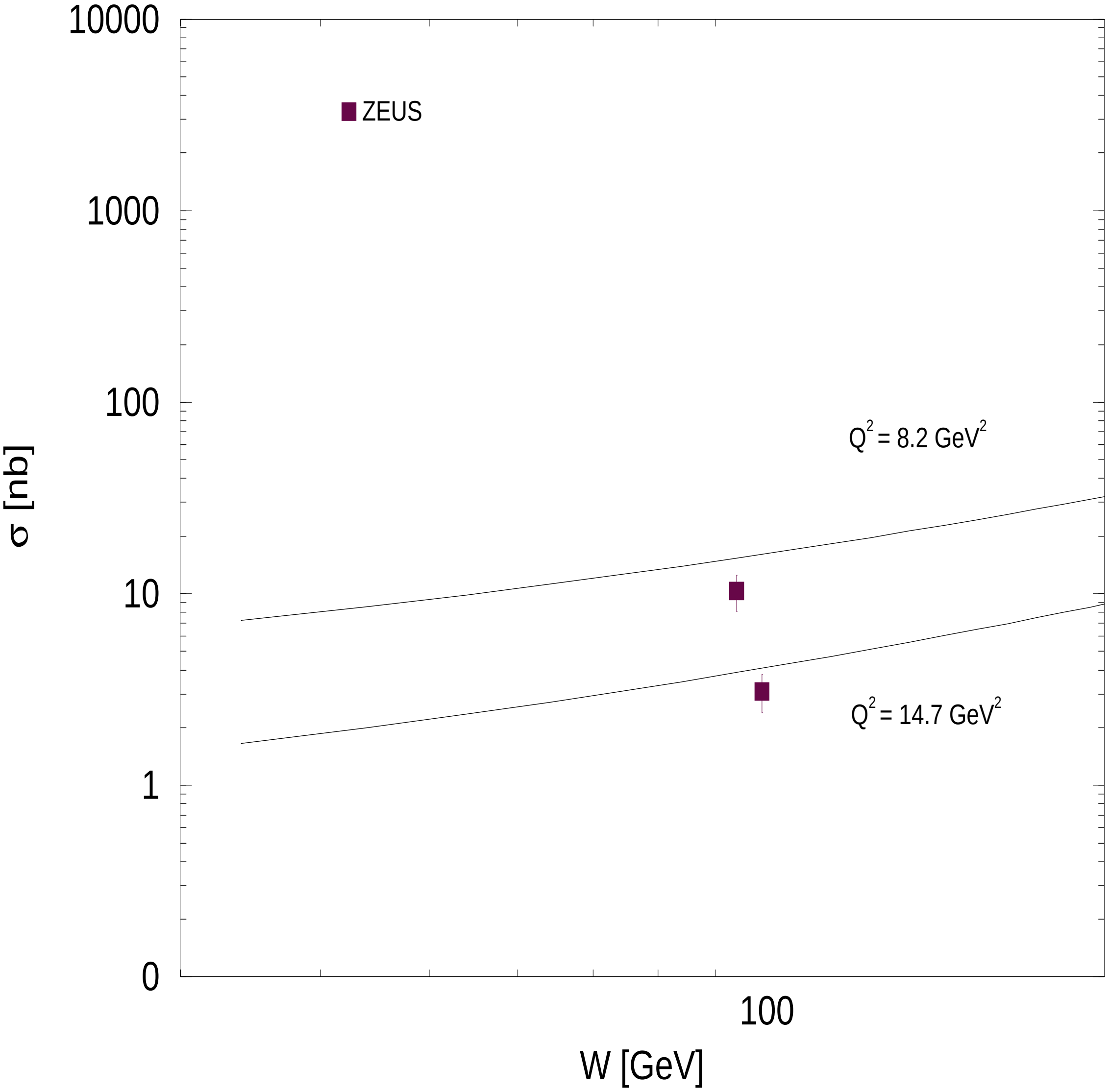

Figure 4.20: The energy dependence of the total cross-section for ϕ production in the FKS model at $W = 90$ GeV, using the DGKP wavefunction. Data from [141].

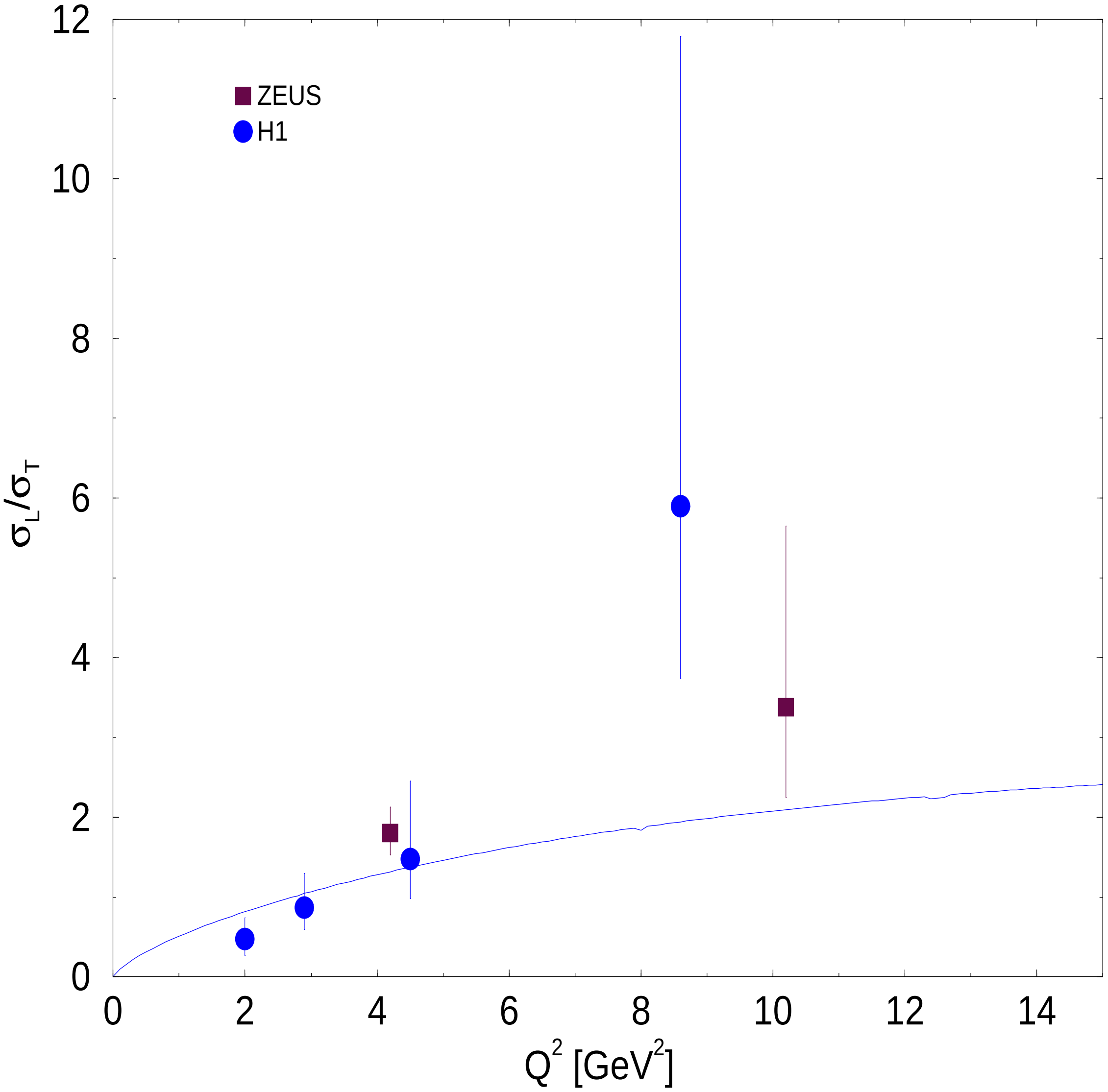

Figure 4.21: The longitudinal to transverse cross-section ratio for ϕ production in the FKS model, using the DGKP wavefunction. Data from [136, 140].

4.7.3 J/Ψ production

Because of the relatively large mass of the charm quark and J/Ψ meson, we expect the physics of J/Ψ production to be different from that of ρ and ϕ production. For example, we have already seen in Section 4.6, the relativistic correction in the longitudinal amplitude is negligible in a large range of Q^2 for the J/Ψ case. We choose $R^2 = 2.0$ GeV^{-2} and $C = 0.9$ so as to have a reasonable fit for the Q^2 dependence of the total cross-section. Using these values of R and C, we find that the normalisation of the total cross-section at $Q^2 = 0$ (where there is a greater number of data points) to be slightly higher than that suggested by the data. For higher Q^2 values, a reasonable description of the data is obtained, see Figure 4.23. In contrast with the ρ and ϕ case, we *are* able to describe the ratio data with the same values for R and C. However, note that fewer data points are available for J/Ψ ratio data with large error bars. We understand qualitatively these results as follows : The relatively large charm mass makes J/Ψ production more short-distance dominated at the same Q^2 value, as compared to light meson production. Therefore at a given Q^2, the transverse amplitude is relatively more suppressed resulting in more rapidly increasing ratio of longitudinal to transverse cross-section. We leave a more quantitative analysis of our results to a future work.

With the DGKP wavefunction, we also achieve a rather good simultaneous description of the available total cross-section and ratio data. In contrast to what we observed for the light mesons, we notice that, in the photoproduction limit, the DGKP wavefunction predicts a *lower* cross-section than the NNPZ wavefunction.

Finally, we note that the predictions of the GW dipole model are not very different from those of the FKS dipole model when using the NNPZ wavefunction.

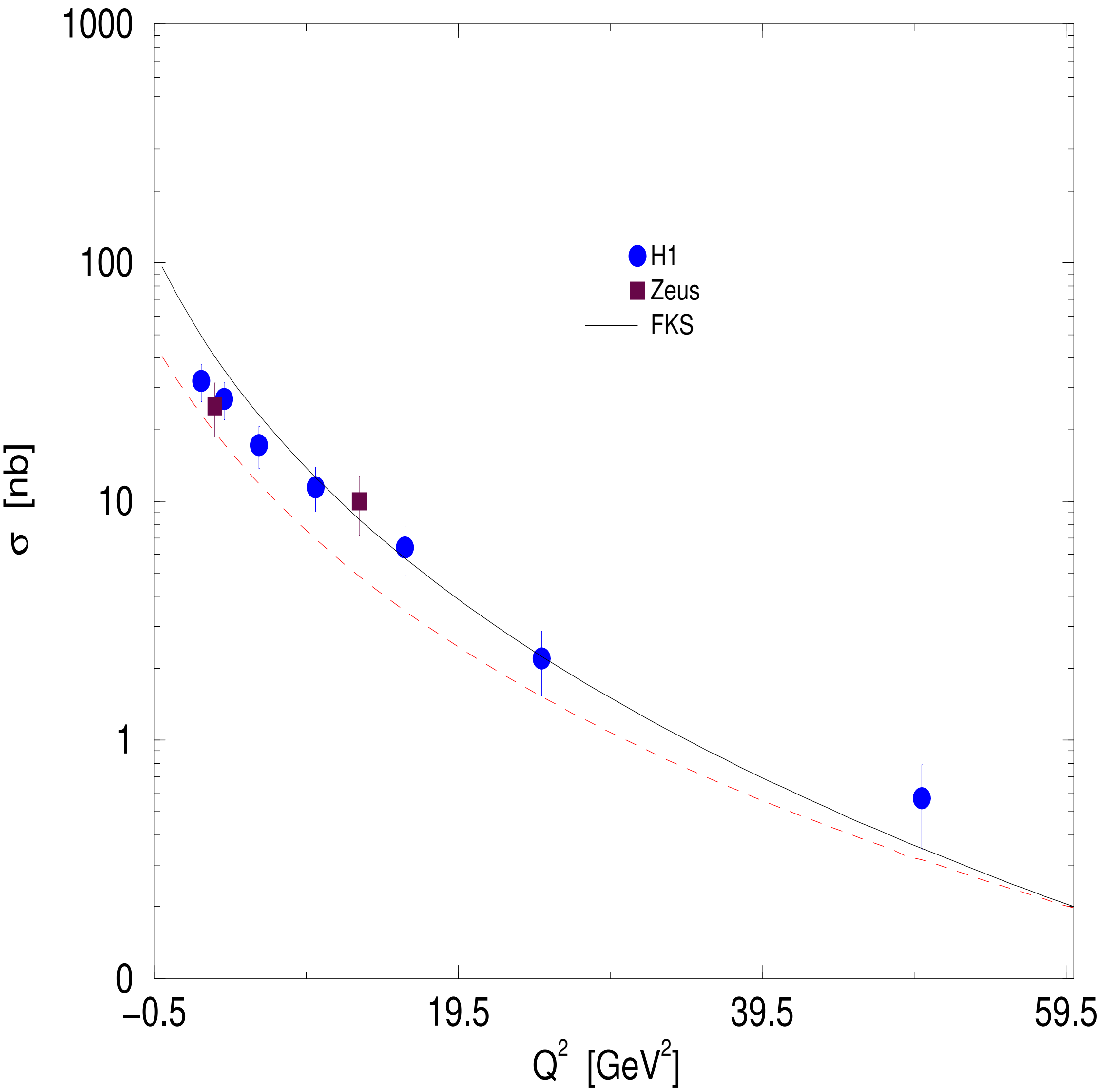

Figure 4.22: The Q^2 dependence of the total cross-section for J/Ψ production in the FKS (solid line) and GW (dashed line) dipole model, at $W = 90$ GeV. The free parameters of the NNPZ wavefunction are set to $R^2 = 2.0$ GeV^{-2} and $C = 0.9$. Data from [142, 143].

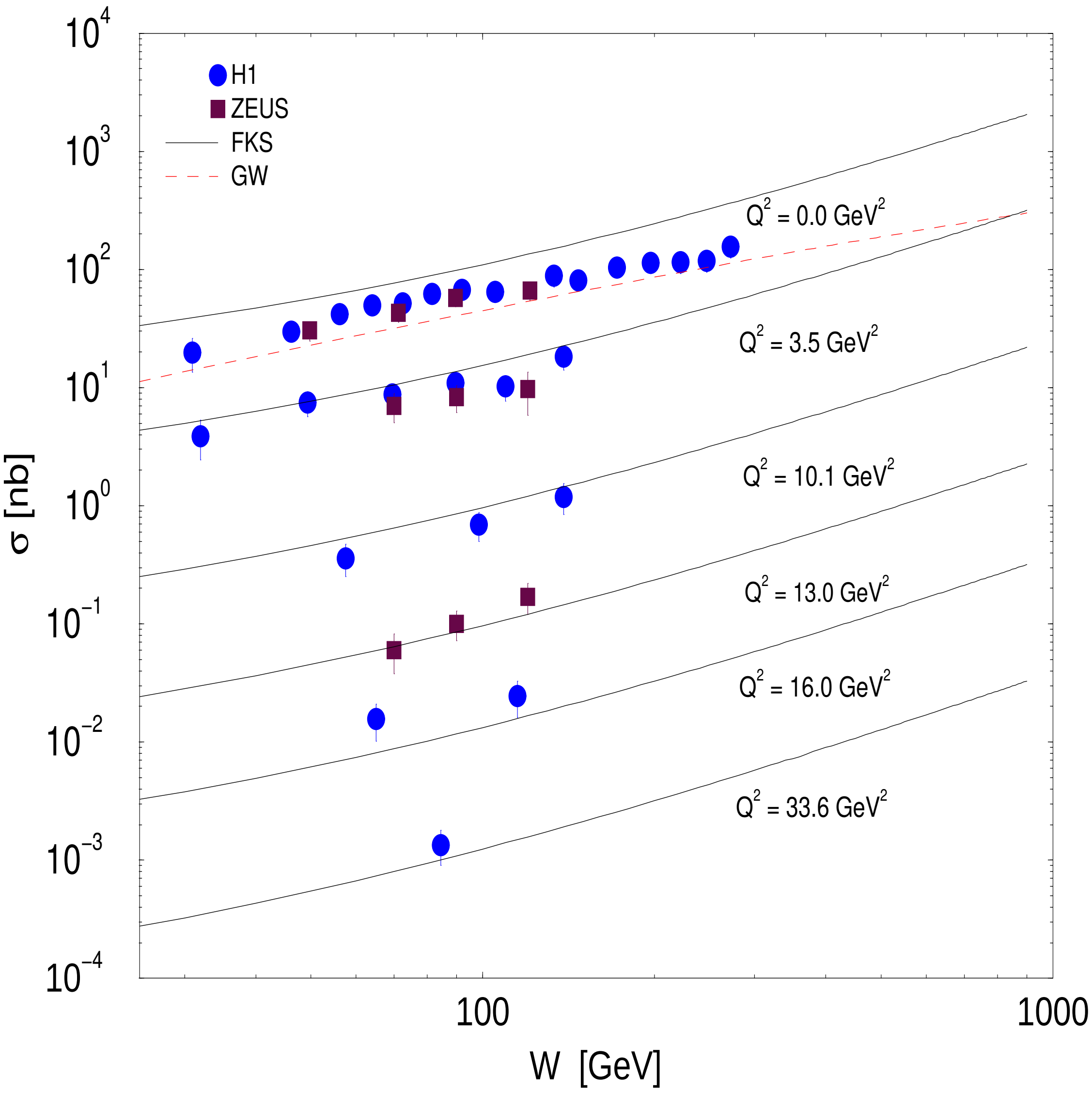

Figure 4.23: The energy dependence of the total cross-section for J/Ψ production in the FKS (solid line) and GW (dashed line) dipole model, at different Q^2. The free parameters of the NNPZ wavefunction are set to $R^2 = 2.0$ GeV^{-2} and $C = 0.9$. For clarity of presentation, the data and theoretical curves have been scaled as follows : $Q^2 = 3.5 : \times 1/3, Q^2 = 10.1 : \times 1/15, Q^2 = 13.0 : \times 1/100, Q^2 = 16.0 : \times 1/500, Q^2 = 33.6 \times 1/1000$. Data from [144, 142, 143, 145, 146].

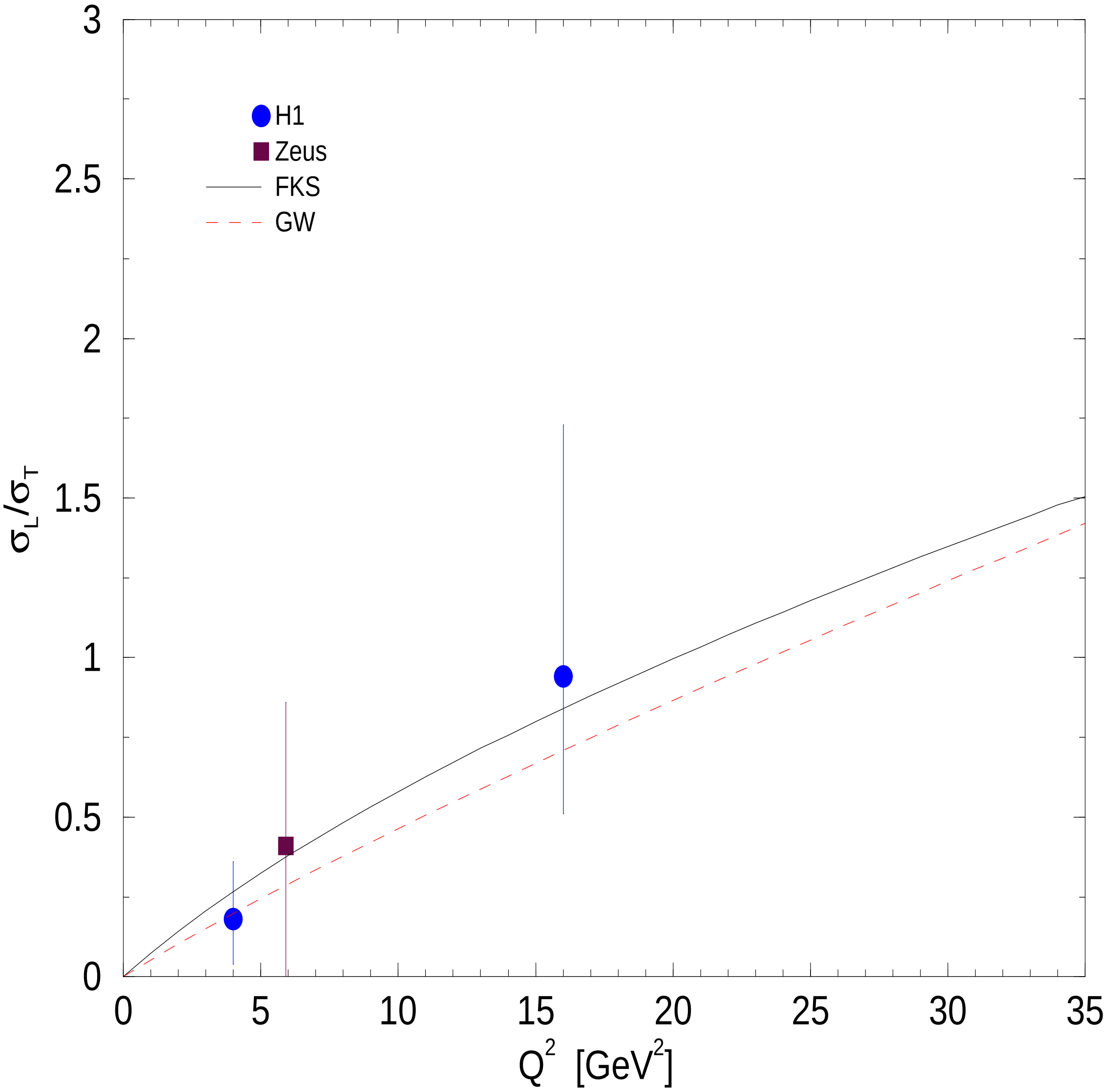

Figure 4.24: The Q^2 dependence of the ratio, $R = \sigma_L/\sigma_T$, at $W = 90$ GeV in J/Ψ production in the FKS (solid line) and GW (dashed line). The free parameters of the NNPZ wavefunction are set to $R^2 = 2.0$ GeV^{-2} and $C = 0.9$. Data from [142, 145].

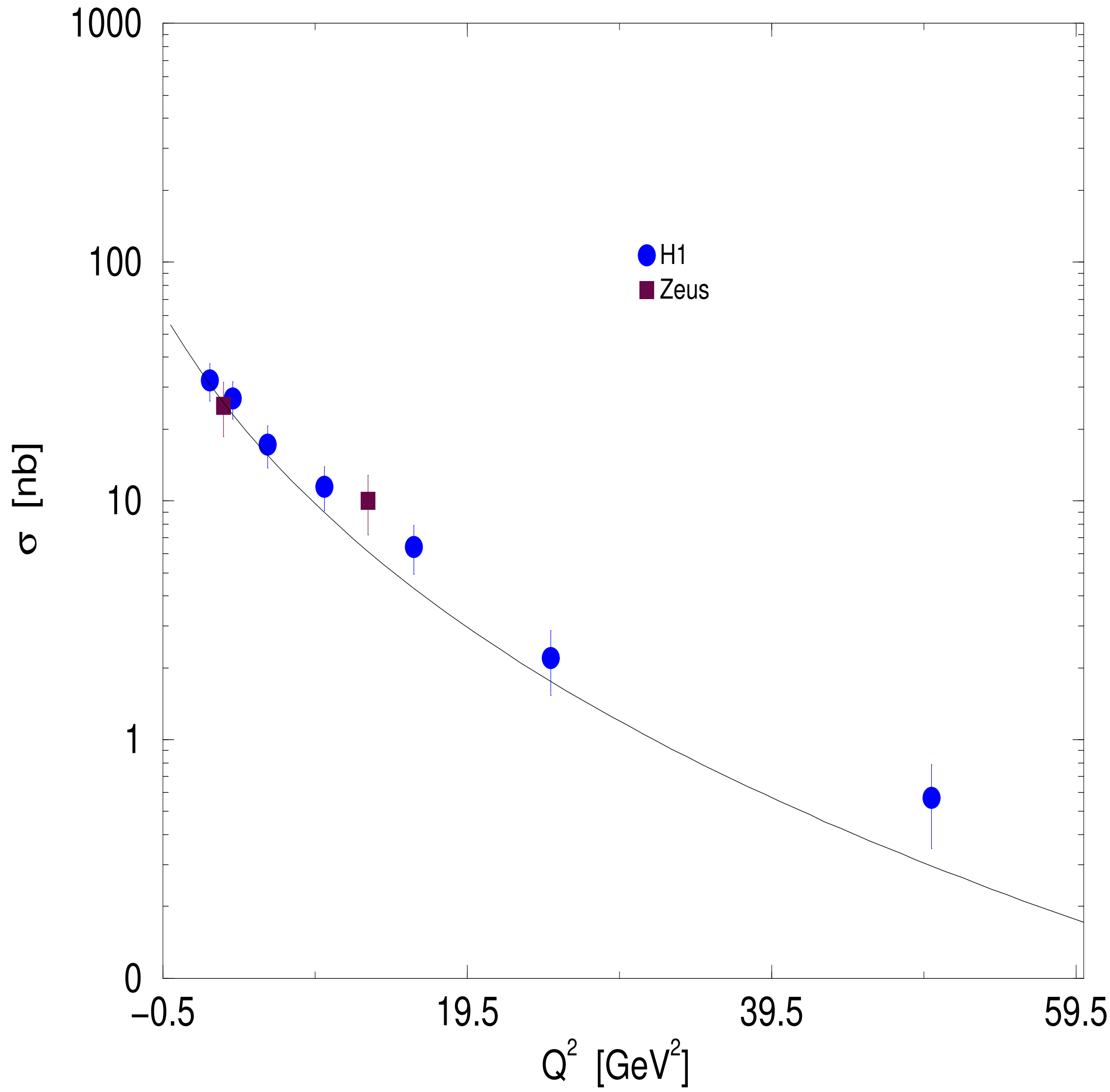

Figure 4.25: The Q^2 dependence of the total cross-section for J/Ψ production in the FKS model at $W = 90$ GeV, using the DGKP wavefunction. Data from [142, 143].

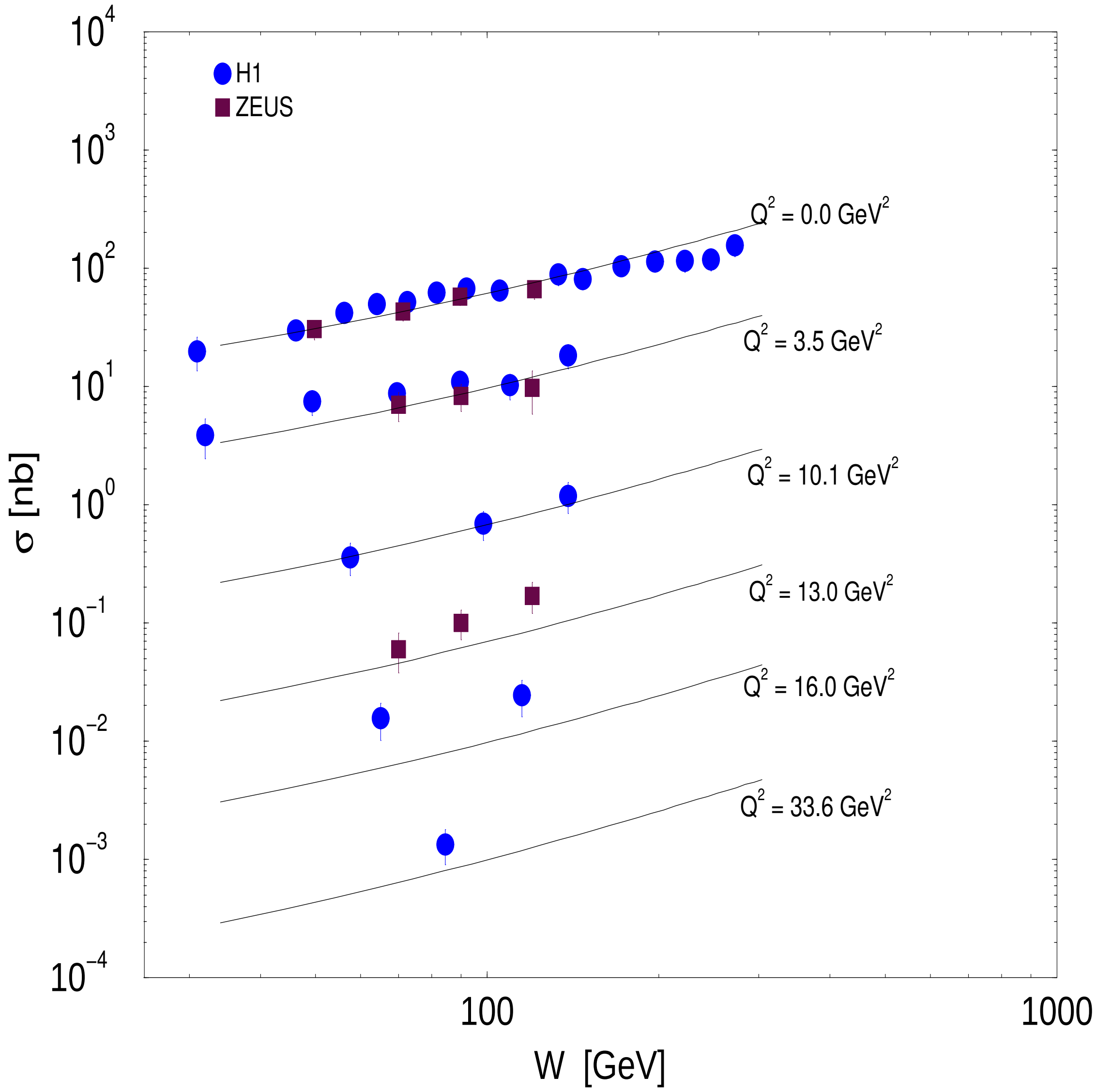

Figure 4.26: The energy dependence of the total cross-section for J/Ψ production in the FKS model at different Q^2, using the DGKP wavefunction. For clarity of presentation, the data and theoretical curves have been scaled as follows : $Q^2 = 3.5 : \times 1/3, Q^2 = 10.1 : \times 1/15, Q^2 = 13.0 : \times 1/100, Q^2 = 16.0 : \times 1/500, Q^2 = 33.6 \times 1/1000$. Data from [144, 142, 143, 145, 146].

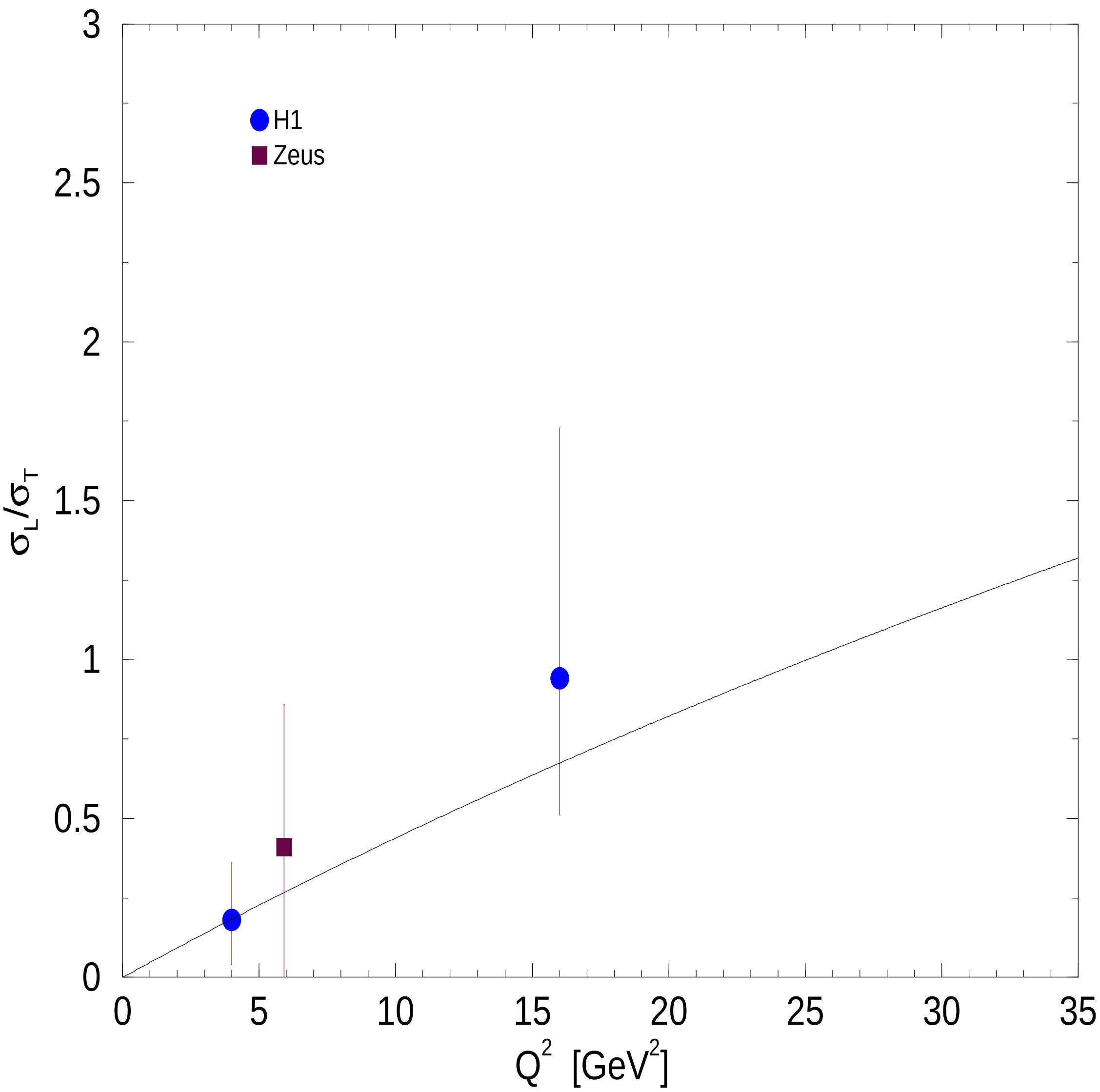

Figure 4.27: The longitudinal to transverse cross-section ratio for J/Ψ production in the FKS model, using the DGKP wavefunction. Data from [142, 145].

Chapter 5

Conclusions

The main focus of this work has been on the application of the colour dipole model to Deeply Virtual Compton Scattering (DVCS) and vector meson production.

After providing essential background material in Chapter 1, we constructed the theoretical framework of the colour dipole model in Chapter 2. In Chapter 3 and 4, we applied the dipole model to DVCS and vector meson production. The latter chapters report original research and contain their own detailed conclusions. Here, we summarise the most important points before indicating possible directions for future work.

For DVCS, we have compared and contrasted two distinct models for the dipole cross-section, the McDermott-Frankfurt-Guzey-Strikman (MFGS) and Forshaw-Kerley-Shaw (FKS) dipole models and find that the predictions are consistent with the H1 data. Both models give very similar predictions for the Q^2 and energy dependencies of the total DVCS cross-section in the kinematic range of the data . The predictions of the two models agree closely even beyond the HERA energy range, despite only one of them including saturation effects, which means that the total cross-section is not a good discriminator between them. In addition, we reconstructed the real part of the amplitude and found that a more pronounced difference between the two models at high energy. We also compared the predictions of the two models with the more recent ZEUS preliminary data and found a more significant difference. The MFGS dipole model gives a better description of the ZEUS data than the FKS dipole model. We note that the uncertainty in the diffractive slope parameter B implies an associated uncertainty in the normalisation of our predictions. It is possible to adjust the value of the diffractive slope to achieve better agreement with data using the FKS dipole model.

In the case of vector meson production, the need to use the essentially unknown meson light-cone wavefunction introduces a major element of uncertainty in our calculation. We have used two different parametrisations, one proposed by Nemchik et al. (NNPZ) and another by Dosch et al. (DGKP). We give predictions for the Q^2 and W dependencies of the total cross-section and also for the ratio of longitudinal to transverse cross-section for ρ, ϕ and J/Ψ vector meson production.

Our strategy was to use the FKS dipole cross-section in its present form (which is accurately extracted from F_2 and photoabsorption data) and tune the two free parameters of the NNPZ wavefunction in order to fit the data. For the light mesons ρ and ϕ, we find that, with the same set of free parameters, we *cannot* simultaneously fit the Q^2 and energy dependencies of the total cross-section and the ratio of longitudinal to transverse cross-section data. Choosing to fit the total cross-section data, we predict a too slow dominance of the longitudinal cross-section over the transverse cross-section with increasing Q^2. On the other hand, we are able to describe simultaneously the available data with the same set of free parameters for the heavier J/Ψ meson. This difference, compared to our results for the light mesons, is somewhat expected because the heavier charm mass makes the process more short-distance dominated.

With the NNPZ wavefunction, we find the relativistic correction in the longitudinal amplitude to be unimportant for J/Ψ for the Q^2 range for which the data are available while becoming gradually more significant at high Q^2 for the light mesons. On the other hand, for the transverse amplitude, we find the relativistic corrections significant for the considered Q^2 range for all three mesons. It is important to note that these remarks hold for the set of free parameters (of the NNPZ wavefunction) we use to fit the data, in particular the free parameter R which controls the exponential suppression of large relative transverse momentum between the quark and the antiquark in the meson.

On the other hand, with the DGKP wavefunction, we chose to use the parameters of the wavefunction which correctly satisfy the semi-leptonic decay width constraint of the meson light-cone wavefunction and we do *not* tune the free parameters to fit the data. Here, different parameters are used for the longitudinal and transverse light-cone wavefunctions.

We highlight the fact that different models propose different sets of values for the quark masses. For consistency, we used the same quark mass in the photon and meson light-cone wavefunction. When using the NNPZ wavefunction, we used the set of quark masses given in the FKS dipole model and when using the DGKP wavefunction, we used that given in the DGKP model. Since the parameters of the FKS dipole model are fitted to total cross-section data using the FKS set of quark masses, it is not strictly legitimate to use another set of quark masses for calculating vector meson production. A better approach would be to recalculate the free parameters of the DGKP wavefunction using the leptonic decay width constraint and the normalisation condition, with the FKS set of quark masses.

We find less good agreement with the total cross-section data for light mesons using the DGKP wavefunction compared to when using the NNPZ wavefunction, particularly in the photoproduction limit. The DGKP wavefunction predicts a faster rise of the longitudinal to transverse cross-section with increasing Q^2. However we cannot conclude a better agreement with the ratio data because the error bars are large on most of the ratio data points.

The physics of transverse and longitudinal meson production being different, it might prove sensible to use different free parameters in the transversely and longitudinally polarised NNPZ meson light-cone wavefunction. This will certainly be the first extension of our present analysis. To make our analysis more precise, we need to do a MINUIT fit to the data and extract the free parameters of the meson light-cone wavefunction. Using only the NNPZ and DGKP parametrisation of the meson light-cone wavefunction, we have not yet exploited the variety of parametrisations of the meson light-cone wavefunctions available in the literature [108, 147, 125, 148]. It would be very instructive to study the predictions of the FKS dipole model using other models for the meson light-cone wavefunction. In this way we can hope to pin down the details of the meson light-cone wavefunction. We are also interested in computing the predictions of the MFGS dipole model for vector meson electroproduction[1] and compare with our present results. We finally need to reconstruct the real part of the vector meson production amplitude in the same way as we did for DVCS.

We leave these possible improvements of our analysis to a forthcoming work [149].

[1]The model has been applied to J/Ψ photoproduction in [76].

References

[1] M. L. Perl, *High energy hadron physics* (John Wiley and Sons, New York, 1974)

[2] F. Halzen and A. D. Martin *Quarks and leptons : An introductory course in modern particle physics* (John Wiley and Sons, Chichester, 1984)

[3] J. R. Forshaw and D. A. Ross, *QCD and the Pomeron* (Cambridge University Press, Cambridge, 1997)

[4] R. E. Cutkosky, J. Math. Phys. **1** (1960) 429

[5] T. Regge, Nuov. Cim. **14** (1959) 951; Nuov. Cim. **18** (1960) 947

[6] P. D. Collins, *An introduction to Regge theory and High Energy Physics*, (Cambridge University Press, Cambridge, 1977) and references therein

[7] A. Sommerfeld, *Partial Differential Equations in Physics* (Academic Press, 1949)

[8] G. N. Watson, Proc. Roy. Soc. **95** (1918) 83

[9] F. Carlson, *Upsala thesis* (1914)

[10] G. F. P. Chew and S. C. Frautshi, Phys. Rev. Lett. **7** (1961) 394

[11] L. F. Foldy and R. F. Peierls, Phys. Rev. **130** (1963) 1585

[12] I. Y. Pomeranchuk, Sov. Phys. **3** (1956) 306

[13] A. Levy, in *Lectures on QCD, Applications*, edited by F. Lenz, H. Griebhammer, D. Stoll (Springer-Verlag, Berlin, 1997) and references therein

[14] M. E. Peskin, D. V. Schroeder, *An introduction to quantum field theory* (Addison-Wesley, Reading, 1995)

[15] R. K. Ellis, J. Stirling, B. Webber, *QCD and collider physics* (Cambridge University Press, Cambridge, 1996)

[16] Ta-Pei Cheng and Ling-Fong Li, *Gauge theory of elementary particle physics* (Oxford University Press, Oxford, 1984)

[17] C. N. Yang and R. L. Mills, Phys. Rev. **96** (1954) 191

[18] J. D. Bjorken, Phys. Rev. **179** (1969) 1547

[19] E. Leader, *Spin in particle physics* (Cambridge University Press, Cambridge, 2001)

[20] R. L. Jaffe, in *Lectures on QCD, Applications*, edited by F. Lenz, H. Griebhammer, D. Stoll (Springer-Verlag, Berlin, 1997) and references therein.

[21] M. Kuhlen, *QCD at HERA, The Hadronic Final State in Deep Inelastic Scattering*, Springer Tracts in Modern Physics **150** (1999)

[22] B. Foster, *Low-x physics*, hep-ex/0008069v1

[23] S. Hassani, *Mathematical Physics*(Springer-Verlag, New York, 1998)

[24] A. Donnachie, P. V Landshoff Phys. Lett. **B296** (1991) 227

[25] ZEUS collaboration, DESY-01-064 (May 2001)

[26] J. R. Forshaw, Photon '97: Theory Summary, hep-ph/9707238; J. R. Forshaw, *Introduction to diffraction*, presented at the 2001 CTEQ Summer School on QCD Analysis and Phenomenology (Scanned transparencies at *http://theory.ph.man.ac.uk/ forshaw/*)

[27] J. D. Walecka, *Electron scattering for nuclear and nucleon structure*(Cambridge University Press, Cambridge, 2001)

[28] E. Predazzi, *Diffraction: past, present and future*, hep-ph/9809454

[29] G. Shaw, *Introduction to diffractive photoprocesses*, Proceedings of the International Conference on the Structure and Interactions of the Photon("Photon 2000"), Ambleside, Ambleside, August 2000 (AIP Conference Proceedings, Volume 571, 2001)

[30] B. H. Wiik, Proceedings of the workshop physics at HERA, edited by W. Buchmüller and G. Ingelman (Hamburg, Germany, 1991)

[31] H1 Collab., I. Abt et al., DESY (1993) 93-103

[32] ZEUS Collab., M. Derrick et al., DESY (1993) 1993

[33] T. Ahmed et al., Nucl. Phys. **B439** (1995) 471

[34] M. Derrick et al., Z. Phys. **C65** (1995) 379

[35] Yu. L. Dokshitzer, Sov. Phys. JETP **46** (1977) 641; V. N. Gribov, L. N. Lipatov, Sov. J. Nucl. Phys. **15** (1972) 438 and 675; G. Altarelli, G. Parisi, Nucl. Phys. **126** (1977) 297

[36] J. Collins et al., in *Perturbative quantum chromodynamics*, edited by A. H. Mueller (World Scientific, 1994)

[37] ZEUS Collab., DESY-01-064 (May 2001)

[38] E. A. Kuraev, L. N. Lipatov and V. S. Fadin, Sov. Phys. JETP **45** (1972) 199; Y. Y. Balitsky, L. N. Lipatov, Sov. J. Nucl. Phys. **28** (1978) 282; For a derivation of the BFKL equation, see [3] and [15]

[39] S. Fadin and L. N. Lipatov, Phys. Lett. **B429** (1998) 127; M. Camici and M. Ciafaloni, Phys. Lett. **B430** (1998) 349

[40] J. D. Bjorken and E. A. Paschos, Phys. Rev **185**, (1969) 1975

[41] R. P. Feynman, quoted in [40]; For a pedagogical discussion, see e.g [2]

[42] J. D. Bjorken, Phys. Rev. **D47** (1993) 101

[43] J. C. Collins, *Light-cone variables, Rapidity and all that*, hep-ph/9705393

[44] A. D. Martin, M. Wüsthoff, J. Phys. **G25** (1999) R309

[45] C. Adloff *et al.*, H1 Collab., Phys. Lett. **B517** (2001) 47

[46] ZEUS collaboration, submitted to the XXX1st International Conference on high enrgy physics, July 2002, Amsterdam, The Netherlands, abstract 825

[47] S. Brodsky, in *At the frontier of particle physics*, Vol. 2, Edited by M. Shifman (World Scientific, Singapore, 2001)

[48] J. Collins, J.Phys. **G28** (2002) 1069 and references therein

[49] A. H. Mueller, Nucl. Phys. **B335** (1990) 115; N. Nikolaev and B. G. Zakharov, Z. Phys. **C53** (1992) 331

[50] D. Yu. Ivanov and M. Wüsthoff, Eur. Phys. J. **C8** (1999) 107

[51] S. Gieseke and C. F. Qiao, Phys. Rev. **D61** (2000) 074028; S. Gieseke, private communication

[52] S. Gieseke, *Virtual photon interactions in high energy QCD*, PhD thesis, Hamburg, 2001

[53] P. S. Cherzor et al. *Optimization of symbolic evaluation of helicity amplitudes*, hep-ph/0101265v1.

[54] F. Mandl and G. Shaw, *Quantum field theory*, Revised Edition (Wiley-Interscience, Chichester, 1984)

[55] E. Yehudai, *The Vector Equivalence Technique*, Fermilab Pub-92-256-T, 1992.

[56] A. Harindranath, *An introduction to light front dynamics for pedestrians*, hep-ph/9612244; Resources on light-cone physics can be found at the light-front homepage *http://202.41.94.71/ hari/light/light.html*

[57] T. Heinzl, *Light-cone quantisation: Foundations and Applications*, hep-th/0008096v2.

[58] S. J. Brodsky and G. P. Lepage, Phys. Rev. **D22** (1980) 2157

[59] H. G. Dosch et al., Phys. Rev. **D55** (1997) 2602

[60] S. J. Brodsky and G. P. Lepage, *Exclusive processes in quantum chromodynamics*, Contribution to 'Perturbative quantum chromodynamics', edited by A. H. Mueller (World Scientific, 1994)

[61] M. Abramowitz and I. A. Stegun, *Handbook of Mathematical Functions*, (Dover, New York, 1964)

[62] T. Kinoshita, J. Math. Phys. **3** (1962) 650, Lee T. D and M. Nauenberg, Phys. Rev **B133** (1964) 1549

[63] S. Catani, M. Ciafaloni and F. Hautmann, Phys. Lett. **B307** (1993) 147

[64] A. Bialas et al., Nucl. Phys. **B593** (2001) 438

[65] N. N. Nikolaev and B. G. Zakharov, Phys. Lett. **B332** (1994) 184

[66] L. Frankfurt et al., Phys. Rev. **D55** (1997) 98

[67] S. Brodsky et al., Phys. Rev. **D50** (1994) 3134

[68] V. L. Chernyak and A. R. Zhitnitski, Phys. Rep. **112** (1984) 173

[69] A. D. Martin, M. G. Ryskin, Phys. Rev. **D57** (1998) 6692

[70] A. H. Mueller, *Parton Saturation*, Lectures given at the international summer school on particle production spanning MeV and TeV energies (Nijmegen 99), Nijmegen, Netherlands, 8-20 Aug 1999, hep-ph/9911289

[71] J. R. Forshaw, G. Kerley and G. Shaw, Phys. Rev. **D60** (1999) 074012

[72] J. R. Forshaw, G. Kerley and G. Shaw., Nucl. Phys. **A675** (2000) 80c

[73] K. Golec-Biernat, M. Wüsthoff, Phys. Rev. **D59** (1999) 014017; **D60** (1999) 114023

[74] J. Bartels et al., *DGLAP evolution in the saturation model*, Talk given by K. Golec-Biernat at the X International workshop on Deep Inelastic Scattering (DIS2002), Cracow, 30 April - 4 May 2002.

[75] M. McDermott et al., Eur. Phys. J. **C16** (2000) 641

[76] L. Frankfurt et al., JHEP **0103** (2001) 045

[77] L. Frankfurt et al., Phys. Rev. **D54** (1996) 3194; Phys. Rev. **D57** (1998) 512

[78] H. Lai et al., CTEQ Collab. Phys. Lett. **D55** (1997) 1280

[79] E. Gotsman, E. Levin and U. Maor, Phys. Lett. **B425** (1998) 369, Eur. Phys. J. **C5** (1998) 303; E. Gotsman, E. Levin, U. Maor and E. Naftali, Nucl. Phys. **B539** (1999) 535, Eur. Phys. J. **C10** (1999) 689 and references therein

[80] M. McDermott, *The dipole picture of small-x physics (A summary of the Amirim meeting)*, hep-ph/0008260 v2

[81] A. Freund, V. Guzey, Phys. Lett. **B462** (1999) 178; Numerical methods in the LO evolution of non-diagonal parton distributions: the DGLAP case, hep-ph/9801388

[82] M. McDermott, R. Sandapen, G. Shaw, Eur. Phys. J. **C22** (2002) 655

[83] C. Adloff et al., H1 Collab., Phys. Lett. **B517** (2001) 47

[84] ZEUS Collab., submitted to the XXX1st international conference on high energy physics, 24-31 July 2002, Amsterdam, The Netherlands, abstract **825**; Y. Yamazaki (ZEUS Collab.), private communication

[85] M. Diehl, *Elastic meson production and Compton scattering*, talk given at the Ringberg Workshop on new trends in HERA physics 2001, 17-22 June 2001, Ringberg castle, Tegernsee, Germany, hep-ph/0109040v2

[86] J. C. Collins, A. Freund, Phys. Rev. **D59** (1999) 074009

[87] Xiang-Dong Ji, J. Osborne, Phys. Rev. **D58** (1998) 094018

[88] B. E. White, J. Phys. **G28** (2000) 203

[89] A. Belitsky et al. , Nucl. Phys. **B593** (2001) 289

[90] L. Frankfurt, A. Freund, M. Strikman, Phys. Rev. **D58** (1998) 114001; *erratum* **D59** (1999) 119901

[91] A. Freund and M. McDermott, Phys. Rev. **D65** (2002) 091901(R)

[92] A. Freund and M. McDermott, Phys. Rev. **D65**, 074008 (2002); Eur. Phys. J. **C23** (2002) 651

[93] A. Donnachie, H. G. Dosch, Phys. Lett. B **502** (2001) 74

[94] A. V. Radyushkin, in *At the frontiers of particle physics*, Vol. 2, Edited by M. Shifman (World Scientific, Singapore, 2001)

[95] F. James, *MINUIT : functional minimization and error analysis*, CERN Program Library Long Writeup, **D506**

[96] J. A. Crittenden, *Exclusive Production of Neutral Vector Mesons at the Electron-Proton Collider HERA* Springer Tracks in Modern Physics **140** (Springer, Berlin, 1997)

[97] J. Olsson, presented at the MESON2002 conference, Krakow, Poland, hep-ph/0209101

[98] A. Kreisel (on behalf of the H1 and ZEUS Collaborations), Submitted to proceedings of LISHEP 2002, hep-ex/0208013

[99] X. Janssen, to appear in procedings of Proceedings of 10th International Workshop on Deep Inelastic Scattering and QCD (DIS 2002), hep-ex/0207011

[100] D. Yu. Ivanov and R. Kirschner, Phys. Rev. **D58** 114026

[101] E. V. Kuraev, N. N. Nikolaev and B. G. Zakharov, JETP Lett. **68** (1998) 696 ; Pisma Zh. Eksp. Teor. Fiz. **68** (1998) 667

[102] J. Gravelis, *Exclusive vector meson production*, PhD thesis, University of Manchester, 1999

[103] A. Donnachie, P. V. Landshoff, Phys. Lett. **B185** (1987) 403, J. R. Cudell, I. Royen, Phys. Lett. **B397** (1997) 317, G. Kerley, G. Shaw, Phys. Rev. **D56** (1997) 7291, D. Schildknecht, G. A. Schuler, B. Surrow, Phys. Lett. **B449** (1999) 328

[104] M. G. Ryskin, Z. Phys. **C57** (1993) 89

[105] M. G. Ryskin et al., Z. Phys. **C76** (1997) 231

[106] S. J. Brodsky et al., Phys. Rev. **D50** (1994) 3134

[107] V. L. Chernyak and A. R, Zhitnitski, Phys. Rep. **112** (1984) 173

[108] L. Frankfurt et al., Phys. Rev. **D54** (1996) 3194

[109] L. Frankfurt et al., Phys. Rev. **D57** (1998) 512

[110] J. C. Collins et al., Phys. Rev. **D56** (1997) 2982

[111] J. R. Forshaw and M. G. Ryskin, Z. Phys. **C68** (1995) 137

[112] A. Martin et al., Phys. Rev. **D55** (1997) 4329

[113] R. Enberg, L. Motyka and G. Poludniowski, hep-ph/0207027

[114] L. Frankfurt et al., JHEP **0103** (2001) 045

[115] K. Suzuki et al., Phys. Rev. **D62** (2000) 031501

[116] B. Z. Kopeliovich et al., Phys. Lett. **B309** (1993) 179

[117] J. Nemchik et al., Phys. Lett. **B341** (1994) 228

[118] J. Nemchik et al., Z.Phys. **C75** (1997) 71

[119] J. Nemchik et al., JETP **86** (1998) 1054

[120] M. Wirbel, B. Stech and M. Bauer, Z. Phys. **C29**(1985) 637

[121] A. Caldwell and M. Soares, Nucl. Phys. **A696** (2001) 125

[122] G. Kulzinger et al., Eur. Phys. J. **C7** (1999) 73

[123] S. Munier et al., Nucl. Phys. **B603** (2001) 427

[124] T. Teubner, in *New trends in HERA physics*, edited by G. Grindhammer, B. A. Kniehl and G. Kramer, Springer, Berlin, 1999 and references therein

[125] H. Halperin and A. Zhitnitsky, Phys. Rev. **D56** (1997) 184

[126] M. Diehl, Talk given at the Ringberg Workshop on New Trends in HERA Physics, Ringberg Castle, Germany, 25-30 May 1997, and references therein

[127] H. G. Dosch, in *At the frontiers of particle physics*, Vol. 2, Edited by M. Shifman (World Scientific, Singapore, 2001)

[128] Tao Huang et al., Phys. Rev. **D49** (1994) 1490

[129] S. Brodsky et al., SLAC-PUB-2540 (1980), Shorter version contributed to 20th Int. Conf. on High Energy Physics, Madison, Wisc., Jul 17-23, 1980

[130] Y. Ivanov et al., Phys. Lett. **B478** (2000) 101; Erratum-ibid. **B498** (2001) 295

[131] C. Adloff et al., H1 Collab., Eur. Phys. J.**C13** (2000) 371

[132] J. Breitweg et al., ZEUS Collab. Eur. Phys. J. **C6** (1999) 603

[133] S. Aid et al., H1 Collab., Nucl. Phys. **B468** (1996) 3

[134] M. R. Adams et al., E665 Collab. Z. Phys. **C74** (1997) 237

[135] M. Arneodo et al., NMC Collab., Nucl. Phys. **B429** (1994) 503

[136] C. Adloff et al., H1 Collab., Phys. Lett. **B360** (2000) 360

[137] M. Derrick et al., ZEUS Collab., Phys. Lett **B377** (1996) 259

[138] M. Derrick et al., ZEUS Collab., Phys. Lett **B380** (1996) 220

[139] J. Breitweg et al., DESY-00-884 (2000)

[140] ZEUS Collab., paper 793, submitted to ICHEP 1998

[141] M. Derrick et al., ZEUS Collab., Phys. Lett. **B380** (1996) 220

[142] C. Adloff et al., H1 Collab., Eur. Phys. J. **C10** (1999) 373

[143] S. Aid et al., H1 Collab., Nucl. Phys. **B468** (1996) 3

[144] C. Adloff et al., H1 Collab., Phys. Lett. **B483** (2000) 23

[145] J. Breitweg et al., ZEUS Collab., Eur. Phys. J. **C6** (1999) 603

[146] J. Breitweg et al., ZEUS Collab., Z. Phys. **C75** (1997) 215

[147] P. Hoodboy, Phys. Rev. **D56** (1997) 388

[148] P. Ball and V. M. Braun, Phys. Rev. **D54** (1996) 2182

[149] J. R. Forshaw, R. Sandapen and G. Shaw, in preparation